UNIVERSITY OF OKLAHOMA

GRADUATE COLLEGE

DRILLING FOAM RHEOLOGY AND HYDRAULICS AT HIGH PRESSURE AND ELEVATED TEMPERATURE

A DISSERTATION

SUBMITTED TO THE GRADUATE FACULTY

in partial fulfillment of the requirements for the

Degree of

DOCTOR OF PHILOSOPHY

By

VINEET SINHA
Norman, Oklahoma
2020

DRILLING FOAM RHEOLOGY AND HYDRAULICS AT HIGH PRESSURE AND ELEVATED TEMPERATURE

A DISSERTATION APPROVED FOR THE

MEWBOURNE SCHOOL OF PETROLEUM AND GEOLOGICAL ENGINEERING

BY THE COMMITTEE CONSISTING OF

Dr. Ramadan Ahmed, Chair

Dr. Prakash Vedula

Dr. Subhash Shah

Dr. Catalin Teodoriu

Dr. Saeed Salehi

DEDICATION

This dissertation is dedicated to my beloved grandparents, who have always been a constant source of inspiration, encouragement, and strength. It is through their blessings that I could undertake my higher studies and face any eventualities of life with zeal, enthusiasm and faith in God.

Acknowledgements

The journey to earning a doctorate and writing a dissertation is long and arduous and certainly not possible single-handedly. Foremost, I would like to express the sincerest appreciation to my advisor, Dr. Ramadan Ahmed; without his supervision, expertise, and support, this research would never have been realized. His work ethic, devotion, and enthusiasm towards research are some invaluable learnings that I will treasure all my life. In the same breath, I would like to acknowledge Dr. Subhash Shah, whose counsel and constant encouragement have been essential to my growth, as a researcher and a professional. Academic and people skills which l acquired during masters working with Dr. Subhash Shah, motivated me to pursue a doctorate degree. I could never have imagined better role models and mentors during my stay at OU.

I would also like to thank my dissertation committee members, Dr. Teodoriu Catalin, Dr. Saeed Salehi, and Dr. Prakash Vedula, for their time, advice, insightful comments and hard questions that helped to refine my dissertation and research presentation. Their technical insights and suggestions have been essential throughout the dissertation writing process.

Special thanks to Jeff McCaskill and late Joe Flenniken for their help throughout my graduate studies, in modifying and building setups and their technical support in overcoming several difficulties while completing my experiments. I would also like to thank Tarek Firoze Akhtar for helping me with the experimental setup during the initial stages of my Ph.D. research.

My sincere thanks to Shirley Ike for offering me an internship opportunity with Wood Group USA Inc. as a part of the flow assurance group and leading me on diverse and challenging projects related to single and multiphase fluid flow problems. Additionally, I would like to thank Wood Group for allowing me to use their resources namely transient simulator OLGA and PVT

fluid tool MultiFlash to help in my research. Special thanks to K.V. Srinivasan and David Roullier for teaching me important concepts related to multiphase flow applicable to real-world problems.

I thank my fellow lab mates at WCTC, Abhishek, Feyi, Harsh, Raj Kiran, Rida, Sarvesh, and Soham, for the stimulating discussions, sleepless nights while working together, and for all the fun we had. I am extremely grateful to Mark Klein, Kim Klein, Chandra, and Bryant, Britt and Jason, Brent, Braden and Tyler, aunt Susan, late grandma Helen and all the kids, for welcoming me in their family and for never letting me feel that I was away from home. I can't be thankful enough to Sami, Abhishek, Bishwa uncle and family for hosting us so many times at their home and always providing encouragement and kernels of wisdom.

I wish to acknowledge the immense support and love of my security blanket "my family". With a pat on the back or a gentle nudge, they have kept me going and what I achieve from now on till the end, would not be possible if it were not for my mother, Vijaya Sinha; father, Binay Kumar Sinha; brother, Vivek Sinha, naniji, Smt. Phoolmati Singh; nanaji, late Sri. Ram Kishore Singh; dadiji late Smt. Shanti Devi; and dadaji, late Sri. Balroop Singh, mausiji Shweta Singh, mausaji, Kumar Gaurav, and my little brother Ishaan. They had faith in me when I had none and no amount of thanks will be enough.

Finally, a very special thanks to my companion, my lovely wife, Aparajita Anand, who has cheered, supported, and encouraged me throughout my PhD. She became a part of my journey and shared all my struggles without an iota of complain. Her presence has been my fortitude which has allowed me to buck up and persevere. I could not have asked for a better partner.

Thank you all!

-Vineet Sinha

Table of Contents

Page

Acknowledgements ..... **v**

Table of Contents ..... **vii**

List of Tables ..... **xiv**

List of Figures ..... **xv**

Abstract ..... **xx**

Chapter 1 ..... **1**

Introduction **1**

1.1 Overview 1

1.2 Problem Statement 5

1.3 Objective 6

1.4 Methodology 7

Chapter 2 ..... **8**

Literature Review **8**

2.1 Foam Quality and Bubble Structure 8

2.2 Foam Generation 10

2.2.1 Techniques to Generate Foam 11

2.3 Measurement of Foam Rheology 13

2.4 Foam Stability 14

2.5 Types of Drilling Foams 16

2.5.1 Aqueous Foams 16
2.5.2 Polymer-Based Foams 18
2.5.3 Oil Based Foams 19
2.6 Foam Rheology Models 20
2.6.1 Mathematical Models 20
2.6.2 Semi-Empirical Models 25
2.6.3 Empirical Models 28
2.7 Wall Slip 34
2.8 Yielding Behavior of Foams 35
2.8.1 Measuring Yield Stress 36
2.9 Modeling of Foam Rheology 39
2.9.1 Published Measurements 39
2.10 Factors Affecting Foam Rheology 40
2.10.1 Foam Quality 40
2.10.2 Base Liquid Type 41
2.10.3 Base Liquid Concentration 42
2.10.4 Surfactant Type and Concentration 43
2.10.5 Foam Generation Technique 44
2.10.6 Bubble Size Distribution 44
2.10.7 Pressure 45

2.10.8 Temperature 47

2.11 Modeling of Foam Flow Hydraulics 47

Chapter 3 55

Theoretical Background 55

3.1 Rheological Models 55

3.2 Rheometry 56

3.2.1 Rotational Viscometer 57

3.2.2 Pipe Viscometer 59

3.2.3 Considerations while Conducting Rheological Measurements 64

3.3 Determination of Foam Density 65

Chapter 4 66

Experimental Studies 66

4.1 Chemical Requirements for Test Fluid Preparation 66

4.1.1 Polymer Sample 66

4.1.2 Foaming Agent 67

4.1.3 Inert Gas 67

4.2 Experimental Apparatus 67

4.2.1 OFITE Model 900 Rotational Viscometer 68

4.2.2 Experimental Flow Loop 68

4.3 Experimental Procedure 73

4.3.1 Test Fluid Preparation....73
4.3.2 Removal of Air from System....73
4.3.3 Setting Foam Quality....74
4.3.4 Flow Data Acquisition....74
4.3.5 Determination of Yield Stress....75
4.4 Test Matrix....76
4.5 Calibration Tests....77
4.5.1 Pipe Viscometer Calibration....77
4.5.2 Static Aging of PAC Base Liquid....78
4.5.3 Thermal Stability of PAC Base Fluid....79
Chapter 5....81
Results and Discussion....81
5.1 Verification of Laminar Flow Regime....81
5.2 Rheology of PAC Foam....83
5.2.1 Effect of Foam Quality....84
5.2.2 Effect of Temperature....86
5.3 Determination of Yield Stress....87
5.4 Development of Correlations for Foam Rheology....91
5.4.1 Expressions for Base Fluid Power Law Parameters....92
5.4.2 Expressions for Foam Power Law Parameters....93

5.5 Comparison of Model Predictions with Experimental Measurements 96

5.6 Model Sensitivities.....97

5.7 Comparison of Experimental Measurements with Existing Models.....99

5.7.1 Comparison with Harris and Reidenbach (1987) Model.....99

5.7.2 Comparison with Bonilla and Shah (2000) Model.....101

5.8 Annular Pressure Prediction.....102

Chapter 6 106

Modeling of Foam Drilling Hydraulics in Wellbore.....106

6.1 Hydraulic Model Formulation 107

6.1.1 Density and Equation of State for Foam.....107

6.1.2 Foam Rheology.....108

6.1.3 Mechanical Energy Balance Equations 109

6.1.4 Closure Equations.....110

6.1.5 Wellbore Configuration.....112

6.1.6 Pressure Drop Across Drill Bit.....114

6.2 Calculation Procedure.....115

6.3 Sample Simulation Cases.....116

6.4 Simulation Results 118

6.4.1 Vertical Wellbore.....119

6.4.2 Three Segment Wellbore.....121

6.5 Parametric Study 123

6.5.1 Effect of Increasing Drilled Depth 123

6.5.2 Effect of Gas and Liquid Injection Rates 125

6.5.3 Effect of Backpressure 128

6.5.4 Effect of Rate of Penetration 129

6.5.5 Effect of Geothermal Gradient 131

Chapter 7 133

Conclusions and Recommendations 133

7.1 Conclusions 133

7.2 Recommendations 134

References 137

Nomenclature 146

Appendix I 150

Experimental Data for Development of Foam Rheology Correlations 150

Appendix II 152

Correlations Used to Calculate Geometric Factors 152

Appendix III 153

Hydraulic Model Formulation 153

III.1 Equation of State 153

III.2 Material Balance 154

III.3 Mechanical Energy Balance 156

Appendix IV **160**

Calculation Procedure for Foam Drilling Hydraulics Model **160**

Appendix V **165**

Base Case Hydraulic Model Results **165**

V.1 Vertical Wellbore 165

V.2 Three-Segment Wellbore 166

List of Tables

Page

Table 2-1: Viscometers for measuring foam rheology (Hutchins and Miller, 2003) 14

Table -3-1: Model parametric constants *A*, *B*, and *C* 56

Table 4-1: Physical properties of POLYPAC-R 67

Table 4-2: Physical properties of Howco-Suds^{TM} 67

Table 4-3: Specifications of OFITE Model 900 Viscometer 68

Table 4-4: Foam formulation and test variables 77

Table 5-1: Equations for coefficients of rheological parameters 96

Table 6-1: Vertical and Three Segment Wellbore Configurations 117

Table 6-2: Input Data for Hydraulic Simulation 118

Table I-1: Fluid Parameters used to formulate foam rheology correlations……..……...150

Table III-1: Regression parameters for calculating the Z factor for Nitrogen gas…….154

Table V-1: Simulation results in a vertical wellbore using base case inputs…...……...165

Table V-2: Simulation results in a three-segment wellbore using base case inputs…..166

List of Figures

Page

Figure 1.1: Foam drilling field layout (Negra˜o, Lage, & Cunha, 1999) 3

Figure 1.2: A 2-D slice of bulk foam: Foam Structure (Schramm, 1994).....4

Figure 1.3: Phenomenon causing foam degradation (Wilson, 1996).....5

Figure 2.1: Relative viscosity as a function of foam quality (Ahmed *et al.*, 2003a) 10

Figure 2.2: Evolution of bubble structure in aqueous foam (Γ = 75%) at 120 s^{-1} (T = 24°C and P = 5 MPa) (Herzhaft *et al.*, 2005).....11

Figure 2.3: Viscometer geometries for Foam Rheology Measurements (Hutchins and Miller, 2003) 13

Figure 2.4: Illustration of the Gibbs-Marangoni effect (Schramm, 1994).....16

Figure 2.5: Relative bubble suspension viscosity as a function of Capillary number, *Ca*, for Φ_b = 0.3 (Truby *et al.*, 2014).....22

Figure 2.6: Bingham plastic viscosity of foam (Blauer *et al.*, 1974).....30

Figure 2.7: Vane rheometer spindle arrangement (Prud'homme and Khan, 1996).....36

Figure 2.8: Angular deflection vs. time for incremental shear stress (Prud'homme and Khan, 1996) 37

Figure 2.9: Comparison of published data on Aqueous Foams 39

Figure 2.10: Comparison of published data on HEC based Foams 40

Figure 2.11: Effect of foam quality (50% to 90%) on bubble structure and viscosity (Harris, 1989) 41

Figure 2.12: Liquid phase-type on 60% quality foams at 1100 s^{-1} (Harris, 1989) 42

Figure 2.13: Effect of gelling-agent on 70% quality foams (Harris, 1989).....43

Figure 2.14: Effect of surfactant type on 70% quality foam at a shear of 1100 s^{-1} (Harris, 1989)43

Figure 2.15: Effect of differential pressure across a foam generator (Harris, 1989) 44

Figure 2.16: Effect of shear rate (90 s^{-1} to 1500 s^{-1}) for 70% quality foam on bubble structure and viscosity, (Harris, 1989).....45

Figure 2.17: Effect of pressure on 70% quality foams (Harris, 1989).....46

Figure 2.18: Reduction of the apparent viscosity of aqueous foams with temperature at 500 s^{-1} (Gu and Mohanty, 2015) 47

Figure 2.19: Velocity field in viscous foam flow with a pure liquid lubricated layer (Peysson and Herzhaft, 2005) 49

Figure 2.20: Pressure drop contour reconstructed from Experimental Data (Edrisi and Kam, 2014a) 50

Figure 3.1: Shear Stress versus Shear Rate for different fluids 55

Figure 3.2: Couette, Parallel Plate, and Cone and Plate geometries for measuring fluid viscosity. 57

Figure 3.3: Velocity profile and components in a Couette geometry rotational viscometer (Lam and Jefferis, 2014).....58

Figure 3.4: Typical pipe viscometer setup (Ahmed and Miska, 2009).....60

Figure 3.5: Fluid flow in pipe segment (Ahmed and Miska, 2009).....60

Figure 3.6: Generalized plot of logarithmic wall shear stress versus logarithmic nominal Newtonian shear rate (Ahmed and Miska, 2009) 62

Figure 4.1: OFITE Model 900 Rotational Viscometer 68

Figure 4.2: Foam Flow Loop Experimental Setup.....69

Figure 4.3: Process flow diagram of Experimental Setup 70

Figure 4.4: Variable speed benchtop mixer 73
Figure 4.5: Flow rate variation during the experiments 75
Figure 4.6: Rheograms from pipe and rotational viscometers (Akhtar, 2017) 78
Figure 4.7: Results of static aging of base liquid (0.25% PAC) 79
Figure 4.8: Rheograms of base fluid (0.25% PAC + Water) before and after high-temperature foam rheology experiments (Akhtar, 2017) 80
Figure 5.1: Fanning friction factor versus Reynolds number 82
Figure 5.2: Rheograms of PAC foam at 79 ºC and different qualities 83
Figure 5.3: Rheograms of PAC foam at 24ºC and different qualities 84
Figure 5.4: Rheograms of PAC foam at 107ºC and different qualities 85
Figure 5.5: Apparent viscosity of the base fluid at different temperatures 87
Figure 5.6: Apparent viscosity of 75% quality PAC foam at different temperatures 87
Figure 5.7: Variation of wall shear stress and needle valve pressure loss with time (D = 6.22 mm, 75% quality at 6.89 MPa) 89
Figure 5.8: Variation of flow rate with time (D = 6.22 mm, 75% quality at 6.89 MPa) 89
Figure 5.9: Wall shear stress vs. time for the medium pipe at 6.89 MPa for 75% quality foam at ambient temperature 90
Figure 5.10: Wall shear stress vs. time for the medium pipe at 6.89 MPa for 65% quality foam at ambient temperature 90
Figure 5.11: Wall shear stress vs. time for the medium pipe at 6.89 MPa for 65% quality foam at ambient temperature 91
Figure 5.12: Normalized fluid behavior index with temperature 92
Figure 5.13: Normalized flow behavior index with temperature 93

Figure 5.14: Normalized foam flow behavior index with different qualities at different temperatures 94
Figure 5.15: Normalized foam consistency index with foam quality and different temperatures 95
Figure 5.16: Actual data (D) versus Model predictions (M) at 24°C 97
Figure 5.17: Actual data (D) versus Model predictions (M) at 149°C 97
Figure 5.18: Predicted apparent viscosity vs. quality at different shear rates and at 24°C 98
Figure 5.19: Predicted apparent viscosity vs. quality at different shear rates and at 149°C 99
Figure 5.20: Measured and HR Model predicted flow curves at 24°C 100
Figure 5.21: Measured and HR Model predicted flow curves at 149°C 101
Figure 5.22: Measured and BS Model predicted flow curves at 24°C 102
Figure 5.23: Measured and BS Model predicted flow curves at 149°C 102
Figure 5.24: Measured and Model predicted wall shear stress at 24°C 105
Figure 5.25: Measured and Model predicted wall shear stress at 149°C 105
Figure 6.1: Schematic of a small control volume 107
Figure 6.2: Foam flow through the pipe and annular sections during drilling 113
Figure 6.3: Schematic for Pressure Drop Across the Drill Bit 114
Figure 6.4: Pressure Drop vs. Measured Depth in Vertical Wellbore 119
Figure 6.5: Foam Drilling Parameters vs. Measured Depth in Vertical Wellbore 120
Figure 6.6: Pressure Drop vs. Measured Depth in Three-Segment Wellbore 122
Figure 6.7: Foam Drilling parameters vs. Measured Depth in Three-Segment Wellbore 122
Figure 6.8: Effect of Drilled Depth on Drilling Parameters in a Vertical Wellbore 124
Figure 6.9: Effect of Drilled Depth on Drilling Parameters in a Three-Segment Wellbore 125

Figure 6.10: Effect of Gas and Liquid Injection Rates on Bottom Hole Pressure in a Vertical Wellbore.....126
Figure 6.11: Effect of Gas and Liquid Injection Rates on Foam Quality at the Bottom of a Vertical Wellbore.....126
Figure 6.12: Effect of Gas and Liquid Injection Rates on Bottom Hole Pressure in a Three-Segment Wellbore.....127
Figure 6.13: Effect of Gas and Liquid Injection Rates on Foam Quality at Bottom of a Three-Segment Wellbore.....128
Figure 6.14: Effect of Changing Back Pressure on Bottom Hole Pressure and Foam Quality in a Vertical Wellbore.....129
Figure 6.15: Effect of Changing Back Pressure on Bottom Hole Pressure and Foam Quality in a Three-Segment Wellbore.....129
Figure 6.16: Effect of Changing Rate of Penetration on Bottom Hole Pressure and Foam Quality in a Vertical Wellbore.....130
Figure 6.17: Effect of Changing Rate of Penetration on Bottom Hole Pressure and Foam Quality in a Three-Segment Wellbore.....131
Figure 6.18: Effect of Changing Geothermal Gradient on Bottom Hole Pressure and Foam Quality in a Vertical Wellbore.....132
Figure 6.19: Effect of Changing Geothermal Gradient on Bottom Hole Pressure and Foam Quality in a Three-Segment Wellbore.....132

Abstract

Foam has been successfully used as the motive fluid for different operations such as well stimulation, underbalanced drilling, enhanced oil recovery (EOR), cleanout, and acidizing operations in the oil and gas industry. Due to its low liquid content, it provides a distinct advantage with regards to less material requirements. However, due to its structure-driven viscosity, high compressibility, and complex flow behavior, accurate predictions of rheology and hydraulic parameters are essential for the success of field operations. This investigation focuses on rheological and hydraulic characteristics of foams, incorporating the effect of temperature on their flow behavior.

In this investigation, polyanionic cellulose (PAC) polymer (0.25% by wt.) based foam was generated using nitrogen as the gas phase and its rheology was determined using a recirculating flow loop that has three pipe viscometers (3.05, 6.22, and 12.7 mm OD) and fully-eccentric annular section (3.05 mm OD × 12.57 mm ID, and 9.53 mm OD × 12.57 mm ID). Experiments were conducted within the temperature range of 24 to 149ºC and at various foam qualities (0%, 45%, 55%, 65%, and 75%).

The foams displayed power-law fluid behavior in the shear rate range tested (100 to 5000 s^{-1}), which is often experienced in the wellbore. Like its base liquid, polymer foam exhibited thermal thinning and a significant rheology change with temperature. Only high-quality foam (75%) at ambient temperature (24ºC) showed yielding behavior, which was measured in a pipe viscometer under static condition. The disappearance of yield stress at elevated temperature could be attributed to the thermal thinning of the liquid phase that weakens the strength of the bubble structure. Experimental data is used to develop new correlations to predict power-law fluid

parameters as a function of temperature, base fluid properties, and foam quality. Moreover, the measurements are compared with the predictions of existing models, and discrepancies are observed, which could be attributed to the variation in foam generation technique, the nature and concentration of polymer, and the concentration of surfactant used in the experiments in which data was obtained to develop the models.

Furthermore, annular pressure loss measurements obtained from fully eccentric annulus at low temperatures (24 and 79ºC) show predominantly good agreement with predictions of a hydraulic model that uses the new correlations. Discrepancies increased with temperature as the foam becomes unstable due to the thermal thinning of the liquid film and subsequent weakening of bubble structure and reduced stability of foam.

A mathematical model has been developed by applying mechanical energy balance on small discretized control volume in the wellbore. The model combines the effect of hydrostatic, frictional and acceleration pressure loss components on the calculation of bottom hole pressure, and predicts foam quality, density, velocity, and pressure at different measured depths. A parametric study was performed to understand the effect of different variables on the foam drilling hydraulics.

Chapter 1

Introduction

1.1 Overview

Foam is a highly concentrated dispersion of gas (dispersed phase) in a liquid medium (continuous phase), stabilized by surfactants. It has many industrial applications including firefighting. Due to its high viscosity, low density, and superior solids carrying capacity, foam is extensively used in the oil and gas industry to improve sweep efficiency and prevent viscous fingering of injected gas/steam during enhanced oil recovery. Foams are also used to seal leaks in cap rocks of storage reservoirs, for plugging thief zones, as motive fluid for hydraulic fracturing in water-sensitive formations and removal of brine from low-pressure gas wells.

The increase in demand for oil has spurred the need for new and improved techniques to produce oil from old depleted fields. This has created a lot of interest in improving underbalanced drilling (UBD) techniques wherein the flowing bottom hole pressure (BHP) is maintained below the pore pressure. Some UBD techniques involve the use of two-phase fluids; however, they have major limitations with proper control over operations due to changing flow regimes and often cause higher BHP fluctuations. The use of single-phase drilling fluid (air or gas) helps mitigate some of these concerns, However, the intrusion of formation water can cause problems such as low drilling rate, the formation of mud rings, and have issues with the operation of downhole motor.

Foam has been used as an alternative drilling fluid for both UBD and completion operations in a depleted, low pressure, faulted, and water-sensitive formations where fine migration and swelling clays are a concern. As UBD fluid, especially in wells with narrow drilling windows,

foam has a number of advantages including i) limited circulation loss, ii) reduced shale sloughing in water-sensitive formation, iii) longer bit life due to efficient cleanup, iv) improved rate of penetration because of negative differential, v) minimal formation damage, vi) lower chances of differential sticking, vii) improved formation evaluation with no interference from mud filtrate, viii) immediate production from reservoir, therefore saving time, ix) potential for dynamic well testing while drilling, and x) improved capacity of handling fluid influx as opposed to gas or air drilling operations. Additionally, foam drilling operations do not require extensive cleanup operations and therefore maximize hydrocarbon recovery. Moreover, the angular velocities are low compared to other light drilling fluids, and therefore, pose little chances of borehole erosion.

Despite its advantages, foam based UBD is not the ultimate solution for formation damage problems. In fact, poorly designed or executed foam-based UBD operations can cause formation damage that exceeds conventional drilling jobs (Bennion *et al.*, 1998; Shah *et al.*, 2010). Some of the limitations of foam-based UBD are: i) inability to maintain underbalanced conditions continuously (all the time), mainly due to improper understanding of foam rheology in downhole conditions (Sanghani and Ikoku, 1983), ii) higher costs especially in challenging conditions (sour gases, remote, and offshore locations), iii) safety concerns with the use of air as dispersed phase (instead of inert gases) which can cause tubing corrosion, iv) requirement of specialized surface equipment such as rotary head, compressor, booster, and separator, v) wellbore instability concerns in poorly consolidated formations, and vi) spontaneous imbibition of foam base liquids by capillary action into the formation (which is generally at sub-irreducible saturation) and can cause near wellbore damage by phase trapping. The typical layout of foam drilling is shown in Figure 1.1.

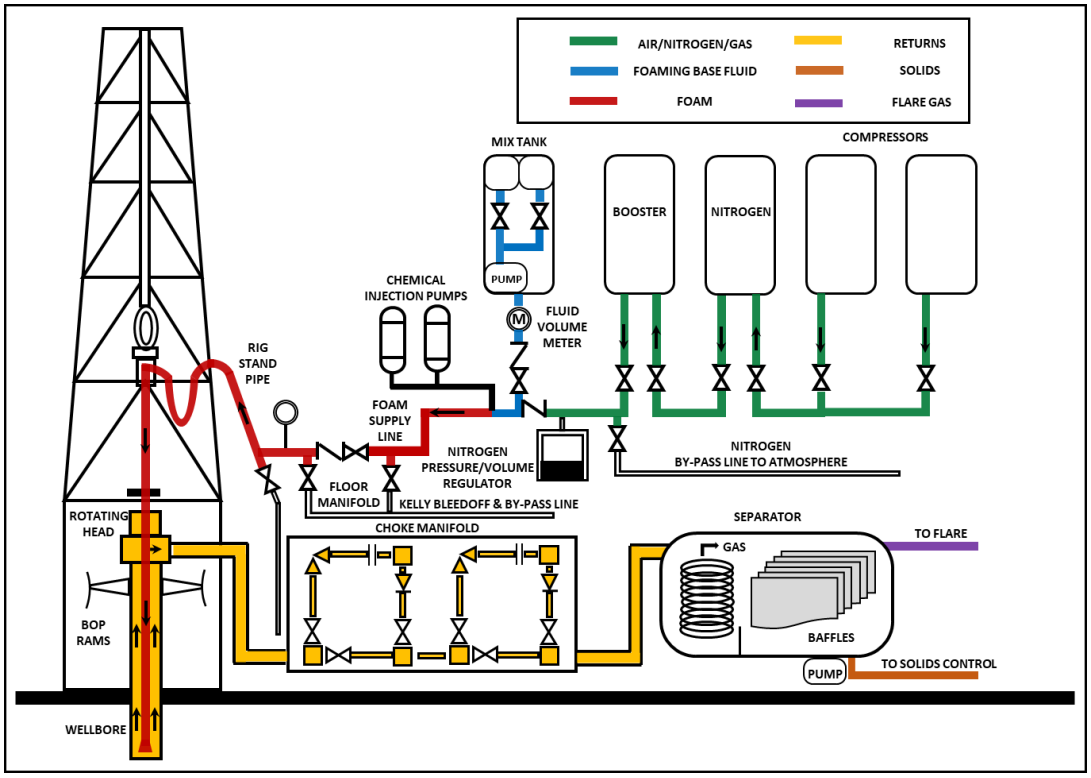

Figure 1.1: Foam drilling field layout (Negra˜o, Lage, & Cunha, 1999)

Structurally, foam consists of polyhedral gas bubbles separated by thin films or lamellae, which is stabilized by the use of surface-active agents and polymers (Nguyen *et al.*, 2016). The connection of three film lamellae constitutes the plateau border which meets at an angle of 120°. The liquid in the polyhedral bubbles is distributed between the films and the Plateau borders. Plateau borders are the channels formed at the confluence of the liquid films. The confluence points are known as vertices. Walls of the polyhedral bubble are smooth surfaces and have uniform curvature (Kraynik and Hansen, 1986). This causes a pressure difference across the surface, with higher pressure on the concave side. Hence, the Plateau border is at a lower pressure than the bubble; this results in destabilization and drainage of liquid out of the film.

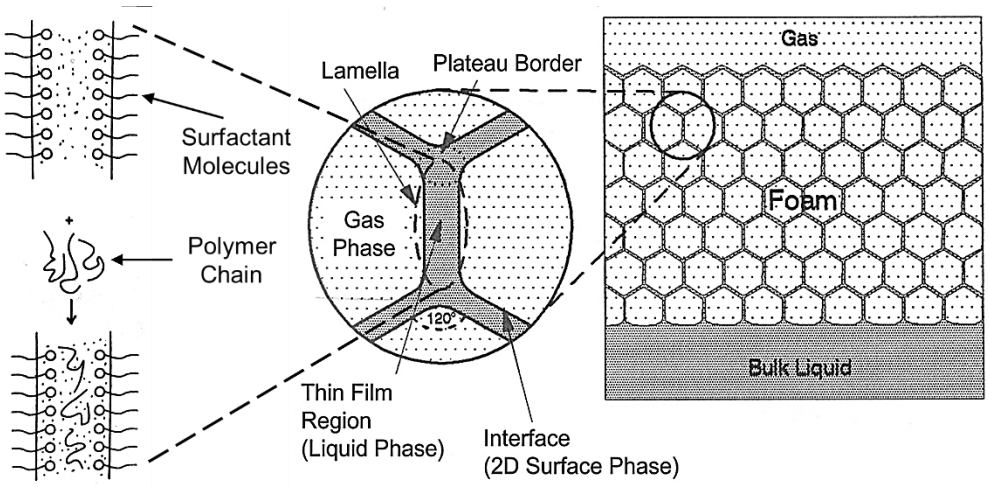

Figure 1.2: A 2-D slice of bulk foam: Foam Structure (Schramm, 1994)

Rheologically, foam displays characteristics of "structured fluid". It behaves like an elastic solid at low shear stress and flows like liquids when the shear stress is high enough to induce bubble rearrangement (Weaire *et al.*, 2006). Kraynik (1988) proposed that the dual behavior of foam, which is considerably different from its constituent phases, requires an in-depth understanding of the interfacial phenomena and bubble level dynamics. However, in case of foam flow through a pipe "bubble/cell" sizes are much smaller than the characteristic dimensions of the flow (pipe diameter), in which continuum description can be applied to develop constitutive equations. Though a brief introduction to foam structure is presented here, this study mainly focuses on the "bulk" flow dynamics of foam. Modeling of bulk foam rheology and hydraulics is critical for the successful design of drilling operations.

Foam has low density; however, it exhibits a very large specific surface area (i.e., the total surface area of a material per unit of mass) and hence, very high surface energy (Nguyen *et al.*, 2016). This makes foam thermodynamically unstable, as foam tries to reduce its surface area and reach a low energy state. Foam decay occurs due to one of the following physical phenomena (Figure 1.3): gravitational drainage, flocculation and coalescence, and disproportionation or

Ostwald ripening. Gravitational drainage of liquid from the lamellae and plateau borders thins the lamellae leading to their eventual rupture. Thinning of the film brings the bubbles together and eventually the coalescence and reordering of bubble structure. Disproportionation involves mass transfer across the lamellae from smaller to larger bubbles due to difference in the capillary pressure. Smaller bubbles shrink, while larger bubbles increase in size eventually leading to coalescence.

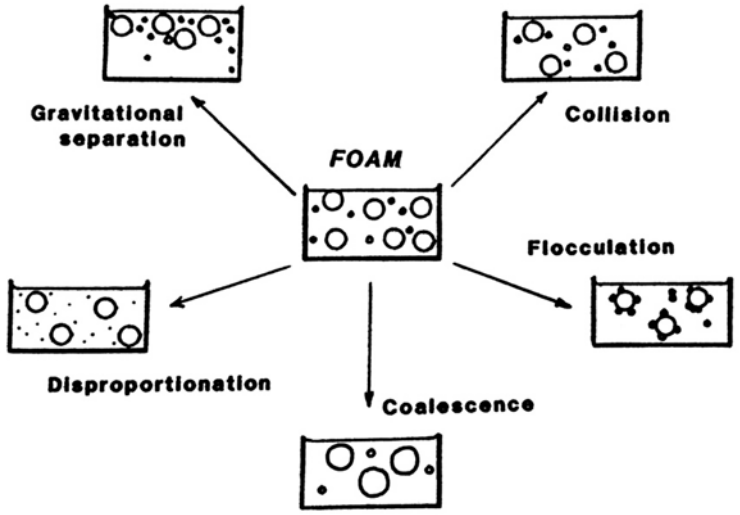

Figure 1.3: Phenomenon causing foam degradation (Wilson, 1996)

1.2 Problem Statement

As previously discussed, foam based UBD, despite its many advantages, presents challenges especially in understanding its rheology and drilling hydraulics. These concerns arise because foam while flowing through drill pipe and annulus undergoes changes in its properties due to variations in wellbore conditions (pressure and temperature). A number of studies have classified foam rheology as either a pseudoplastic (Babatola, 2014; Bonilla and Shah, 2000; Gu and Mohanty, 2015a; Khade and Shah, 2004; Sanghani and Ikoku, 1983; Sani *et al.*, 2001; Sherif *et al.*, 2015a, 2015b) or Bingham plastic model (Beyer *et al.*, 1972; Blauer *et al.*, 1974). However, foam viscosity is not merely a function of shear rate, but also depends on pressure, temperature,

quality, base liquid properties, wall interactions, and expansion effects. Furthermore, foam being compressible, adds another level of complexity in rheological modeling of foam.

Although significant progress has been made in comprehending foam behavior, studies relating its rheological properties and hydraulics in complex flows are still limited. It is imperative to have accurate quantification of foam rheology at each point along the wellbore to facilitate accurate predictions of pressure profiles. This, in turn, will ensure a safe successful and economical UBD design. The present study aims to investigate polymer-based foam rheology at varying temperature and high-pressure using pipe viscometers. The rheological model then provides the basis for the development of a hydraulic model to predict the pressure profile in the wellbore during UBD operation.

1.3 Objective

The primary objective of this study is to investigate the changes in foam rheology due to variations in foam quality and temperature. Nitrogen foams with PAC based polymer foaming solutions were used for the present study. The specific goals of this study are,

- Evaluate the effects of elevated temperature on equilibrated foam at varying qualities using pipe viscometer.
- Quantify foam rheology by developing correlations for rheological model parameters, as functions of quality, base fluid rheology, and temperature.
- Determine the presence of yield stress and wall slip when foam flows under elevated temperature and pressure conditions.
- Validate empirical correlations by comparing actual pressure measurements in an experimental annulus with a published hydraulic model
- Develop a simulator to predict hydraulics during foam drilling operations.

1.4 Methodology

The project objectives are accomplished by performing experimental investigation and modeling analysis. A foam flow loop consisting of three pipe sections with different internal diameter was used to conduct the experiments at elevated pressure and temperature. Results obtained from different diameter pipes helped in investigating the wall slip. Additionally, a fully eccentric annular section was used to simulate annular flow in UBD operations.

Rheological data was obtained using Newtonian fluids (water and mineral oil) to validate measurements and ensure accuracy. The thermal stability of the polymer PAC was tested at a temperature of 149°C (300°F). Following these preliminary tests, rigorous rheology experiments were conducted at varying temperatures and foam quality. The data was analyzed to establish the rheological behavior of PAC foams, as well as to detect the presence of wall slip. Empirical correlations were developed for the fluid rheology model parameters using a non-linear regression technique. The pressure loss data of the annular section is compared with the predictions of the developed correlations using published models. Furthermore, static pressure drop measurements were performed, to determine the yield stress of foam fluids.

A simulator is developed in MATLAB to perform hydraulic analysis for foam drilling operations. The simulator uses the correlations developed from the experimental data. Sensitivity analysis has been performed varying gas and liquid injection rates, back pressures, rate of penetration, and geothermal gradients.

Chapter 2

Literature Review

Foam rheology and stability mainly vary with quality, pressure, temperature, base fluid properties and composition, and foam generation technique that influences the bubble structure. Findings from various studies (Akhtar *et al.*, 2018; Beyer *et al.*, 1972; Blauer *et al.*, 1974; Bonilla and Shah, 2000; Chen *et al.*, 2005d, 2005a, 2005b, 2009; Duan *et al.*, 2008; Gu and Mohanty, 2015a; Harris and Heath, 1996; Khade and Shah, 2004; Sanghani and Ikoku, 1983; Sani *et al.*, 2001; Sherif *et al.*, 2015a, 2015b) have differed depending on experimental conditions, the type of base fluid, and the foam generation technique employed. A brief review of foam studies focusing on foam properties, rheology, and bulk flow properties is presented in the following sections.

2.1 Foam Quality and Bubble Structure

The stability and viscous properties of foams are strongly influenced by their quality, which is the ratio of the volume of gas to the volume of foam at a given temperature and pressure.

$$\Gamma(T,P) = \frac{V_G}{V_G + V_L} \tag{2.1}$$

where, V_G and V_L are gas and liquid volumes.

Foam quality varies in the wellbore with variations in pressure and temperature due to gas compressibility. Raza and Marsden (1967) derived an expression for foam quality along the wellbore for the isothermal flow of an ideal gas with minimal solubility using the ideal gas equation of state and mass conservation laws.

$$\Gamma = \frac{1}{\left[1 + \frac{P}{P_{sc}}\left(\frac{1}{\Gamma_{sc}} - 1\right)\right]} \tag{2.2}$$

where Γ is foam quality at pressure P and Γ_{sc} is quality at standard pressure P_{sc}.

Equation (2.2) is not applicable for foams that are made of highly soluble gases such as CO_2. As pressure increases, gas dissolves into the liquid phase, and a higher amount of gas is required to generate the same quality foam. Moreover, highly soluble gases generate foams that have greater coarsening and coalescence rates, due to increased permeation between bubble films and bubbles and are, therefore, more unstable (Amro *et al.*, 2015; Farajzadeh *et al.*, 2014).

As shown in Figure 2.1, relative foam viscosity (the ratio of foam viscosity to the viscosity of the liquid phase) high-quality foams ($\Gamma > 0.6$) increases exponentially with quality, reaches a peak value and then declines rapidly (Ahmed *et al.*, 2003a). Variations in viscosity are attributed to changes in the microscopic bubble structure. Low quality-wet foams ($\Gamma < 0.6$) behave like "bubbly liquids" and exhibit minimal resistance to flow. Foam undergoes "rigidity transformation" at high qualities ($\Gamma > 0.6$), which results in a well-structured spherical bubble geometry with greater resistance to flow. At even higher qualities ($\Gamma > 0.8$), thin-film polyhedral bubbles are formed. For qualities greater than 0.95, foam transforms to mist, which dispersion of fine liquid droplets in a gas.

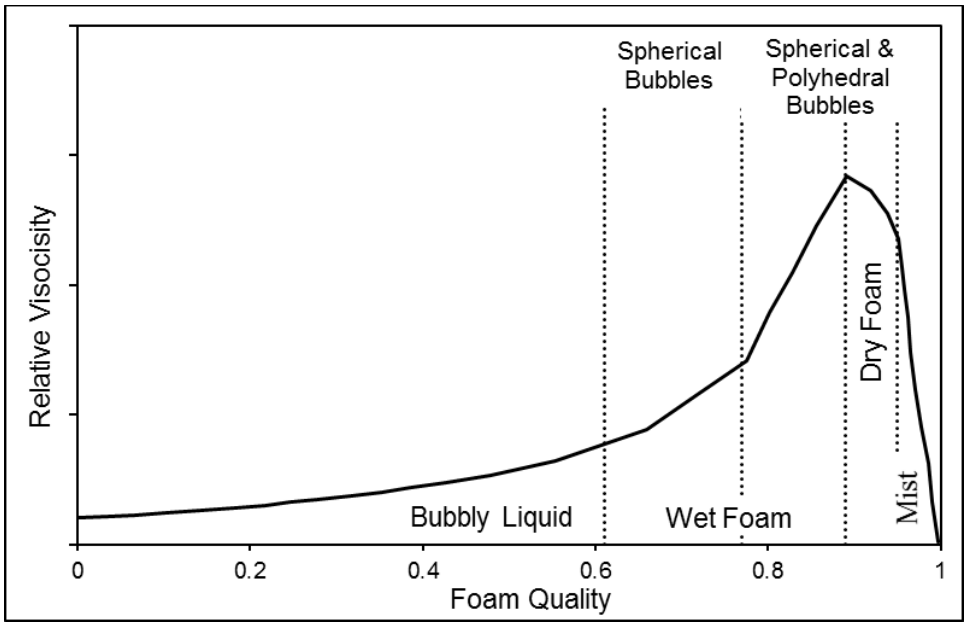

Figure 2.1: Relative viscosity as a function of foam quality (Ahmed *et al.*, 2003a)

2.2 Foam Generation

Foam generation is a non-spontaneous process, which results in the formation of gas-liquid interfaces, with the help of an external shearing force. Foaming increases the net surface energy of the system, which is a product of surface tension, σ, and interfacial area, A ($E = \sigma A$). Developing a stabilized "fully developed" foam requires an optimum shear rate (Lourenco *et al.*, 2004a; Sherif *et al.*, 2015b) and a minimum shearing time (Herzhaft *et al.*, 2005). At high shear larger bubbles rupture to form finer bubbles, while at low shear, bubbles degrade and coalesce. Figure 2.2 shows the evolution of bubble structure in aqueous foam with time. A minimum shearing time of 20 mins at a shear rate of 120 s^{-1} was required to stabilize foam texture (Herzhaft *et al.*, 2005).

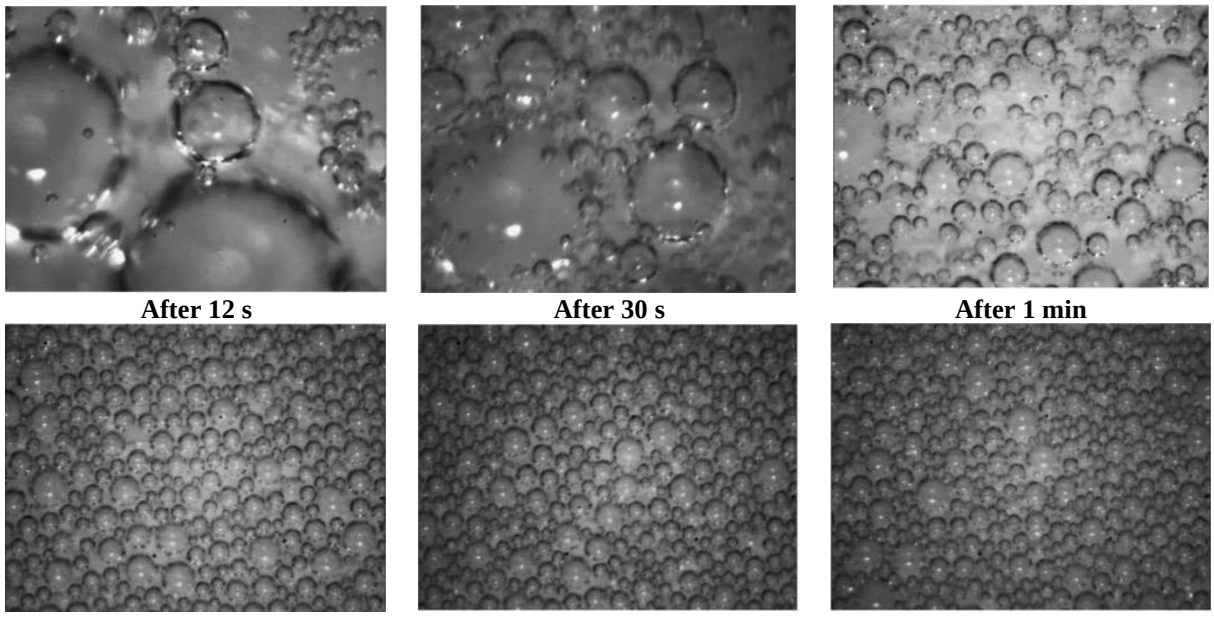

Figure 2.2: Evolution of bubble structure in aqueous foam (Γ = 75%) at 120 s^{-1} (T = 24°C and P = 5 MPa) (Herzhaft *et al.*, 2005)

Foam generation technique has a direct influence on the texture and rheology of foam (David and Marsden, 1969; Harris, 1989; Lourenco *et al.*, 2004a). oil-based applications with partially generated (unequilibrated) foams that have inconsistency in their properties are incredibly difficult to control (Marsden *et al.*, 1967).

2.2.1 Techniques to Generate Foam

Some of the commonly used foam generation methods employed by different studies (Cawiezel and Niles, 1987a; Chen *et al.*, 2005a; David and Marsden, 1969; Gajbhiye, 2011; Khan *et al.*, 1988; Patton *et al.*, 1983; Raza and Marsden, 1967; Reidenbach *et al.*, 1986) are discussed briefly in this section.

- *Bubbling foaming solution through a porous medium:* Enhanced oil recovery studies require fine-textured foam to navigate through the formation and employ a porous medium to generate foam. Commonly used porous medium are, glass wool embedded in epoxy raisin (Patton *et*

al., 1983), crushed Pyrex bed (David and Marsden, 1969), steel wool mesh (Khan *et al.*, 1988), and combination of Ottawa sand and Pyrex bed (Raza and Marsden, 1967).

- *Open flow loop:* Several studies employed a single pass foam generator with shear imparted using either a multiphase pump or a combination of pump and fine filter downstream to impart shearing force (Cawiezel and Niles, 1987b; Chen *et al.*, 2005d, 2005a, 2009; Gajbhiye, 2011; Reidenbach *et al.*, 1986). The limitation of a single-pass foam generator is that it does not allow the formation of equilibrated foam systems (Hutchins and Miller, 2003).
- *Closed flow loop*: In a closed-loop foam generator using flow restriction such as a porous medium or throttled valve (Bonilla and Shah, 2000; Duan *et al.*, 2008; Gu and Mohanty, 2015a; Herzhaft *et al.*, 2005; Sani *et al.*, 2001), the bubble size and foam texture stabilize with time and the amount of energy imparted from the pump can be used to control the foam generation process. With enough recirculation time, an average equilibrated foam texture is achieved. The only demerit of using a recirculating loop is that the bubble structure might change during the measurement as a result of a reduction in circulation rate (Akhtar *et al.*, 2018; Babatola, 2014; Sherif *et al.*, 2015a, 2015b).
- *Closed flow loop with regeneration*: Recent studies (Akhtar *et al.*, 2018; Babatola, 2014; Sherif *et al.*, 2015a, 2015b) employed a setup including a recirculating closed-loop and combination of static mixers and a throttled needle valve to impart the necessary shear to generate foam. The foam was regenerated before each measurement to maintain consistency in foam generation and minimize the effect of degradation on rheology measurements.
- *Coiled tubing foam generator*: Sanghani and Ikoku (1983) used the shear generated from the flow of foaming solution and air in a coiled tubing to create foam. Air and liquid injection rates were controlled to change foam quality.

2.3 Measurement of Foam Rheology

Hutchins and Miller (2003) stated the importance of having a pressurized setup to measure foam rheology in order to prevent foam degeneration. They also discussed the merits and disadvantages of different foam viscosity/rheology measurement techniques. Most commonly used viscometers are Couette type viscometers (Chen *et al.*, 2005c; Khan *et al.*, 1988; Kroezen *et al.*, 1988; Princen, 1983; Saintpere *et al.*, 2000a), recirculating pipe viscometers (Bonilla and Shah, 2000; Harris, 1989; Harris and Heath, 1996; Harris and Reidenbach, 1987; Khade and Shah, 2004; Reidenbach *et al.*, 1986; Sani *et al.*, 2001), and single-pass viscometers (Cawiezel and Niles, 1987a; Chen *et al.*, 2005a; Enzendorfer *et al.*, 1994; Lourenco *et al.*, 2004a; Ozbayoglu *et al.*, 2002, 2005; Sanghani and Ikoku, 1983; Wendorff and Earl, 1983) as shown in Figure 2.3.

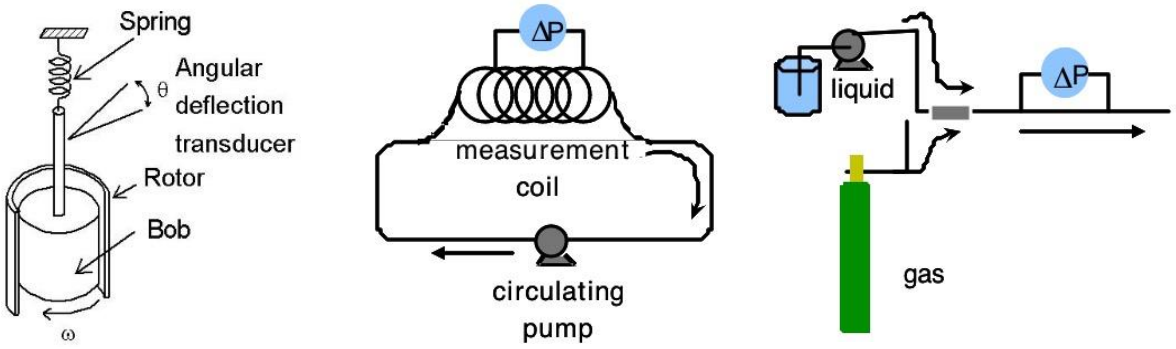

a) Rotational **b) Recirculating** **c) Single Pass**

Figure 2.3: Viscometer geometries for Foam Rheology Measurements (Hutchins and Miller, 2003)

When a Couette type viscometer is used, foam is first generated and allowed to flow through a viscometer. In the case of recirculating and single-pass viscometers, foam is first produced by a combination of static mixers, needle valve, or passing the foaming solution through a porous medium (described in section 2.2.1). Steady-state measurements are obtained from a pipe viscometer section.

Table 2-1 shows the merits, demerits, and applicability of the different viscometers used for measuring foam rheology as identified by Hutchins and Miller (2003).

Table 2-1: Viscometers for measuring foam rheology (Hutchins and Miller, 2003)

	Couette	Circulating Pipe	Single-Pass Pipe
Advantages	• Time-dependent foam property measurement • Small sample size	• Time-dependent foam property measurement • Easy foam visualization	• Time-dependent foam property measurement • Easy foam visualization • Easiest foam-generation
Disadvantages	• Foam containment • Bubbles cream to the top of the cell • Foam visualization is difficult	• Foam structure can change due to circulation	• Large sample size • Time-dependent properties cannot be determined
Suitability	• Low pressure • High-quality foams • Stable foams	• High pressure • Any foam quality	• High pressure • Any foam quality

2.4 Foam Stability

Foam is thermodynamically unstable due to the presence of large surface energy and starts to drain liquid from the bubble films as soon as it is generated. This is followed by foam decay through processes like bubble collision, flocculation, coalescence, and disproportionation or Ostwald ripening (Argillier *et al.*, 1998; Durian and Weitz, in press; Exerowa and Kruglyakov, 1997; Weaire and Hutzler, 2001; Wilson, 1996). Bubble coalescence occurs due to the thinning of the liquid films by loss of liquids, which brings two bubbles closer and leads to one merging into another. Disproportionation, on the other hand, results in diffusion of the smaller bubble into a larger one through the liquid film, due to pressure difference. Foam drainage is mostly driven by two competing forces (gravity and capillary force which opposes liquid drainage), and foam decay through coalescence and disproportionation, which are mainly governed by the surface and bulk

properties such as film elasticity, liquid viscosity, interaction of surfactant molecules within themselves and with polymers, and presence of impurities (Govindu *et al.*, 2019).

To improve foam permanency and bubble film stability, foaming agents such as surfactants, macromolecules, or finely divided solids can be used (Schramm, 1994). Surfactants are surface-active agents, which at concentrations greater than Critical Micelle Concentration (CMC) form aggregates that consist of hydrophobic tails, and hydrophilic heads. These molecules adsorb on the liquid-bubble interface and align themselves so that the hydrophobic tails remain in the gaseous bubble, while the hydrophilic heads protrude in the liquid. This provides an expanding force, which acts against the interfacial tension and tends to reduce its value. Reduction of interfacial tension prevents bubbles from contracting and thereby improves foam stability. Increasing surfactant concentration improves foam stability until it reaches CMC, beyond which further increase addition of surfactant has no effect on stability (Rojas *et al.*, 2001). Additionally, aggregation of surfactant molecules increases interfacial viscosity, which mechanical resistance to film thinning and rupturing (Schramm, 1994).

Foam films display marginal elasticity and can withstand deformation, without rupturing to an extent in the event of bubble expansion. This behavior is explained by the Gibbs elasticity and Marangoni flow effects, collectively known as the Gibbs-Marangoni effect (Clunie *et al.*, in press; Kraynik and Hansen, 1986). In a surfactant stabilized foam system which contains surfactant molecules both in the bulk and the interface, a sudden expansion of the bubble interface provides a new area for the surfactant molecules from the bulk to migrate to the interface. However, after completion of migration, the net surfactant molecules per unit area of the interface reduces, which results in a local increase of the surface tension. Film behaves like a stretched membrane and contracts elastically; this is phenomenon is called “Gibbs elasticity”. “Marangoni flow” refers to

the mass transfer of the liquid phase from the unstretched to the stretched section of the interface due to the pull exerted by the higher surface tension section. Thus, Marangoni flow provides a resisting force to film thinning. These resisting forces exist only until the equilibrium is reestablished in the foam film (no surface tension gradient).

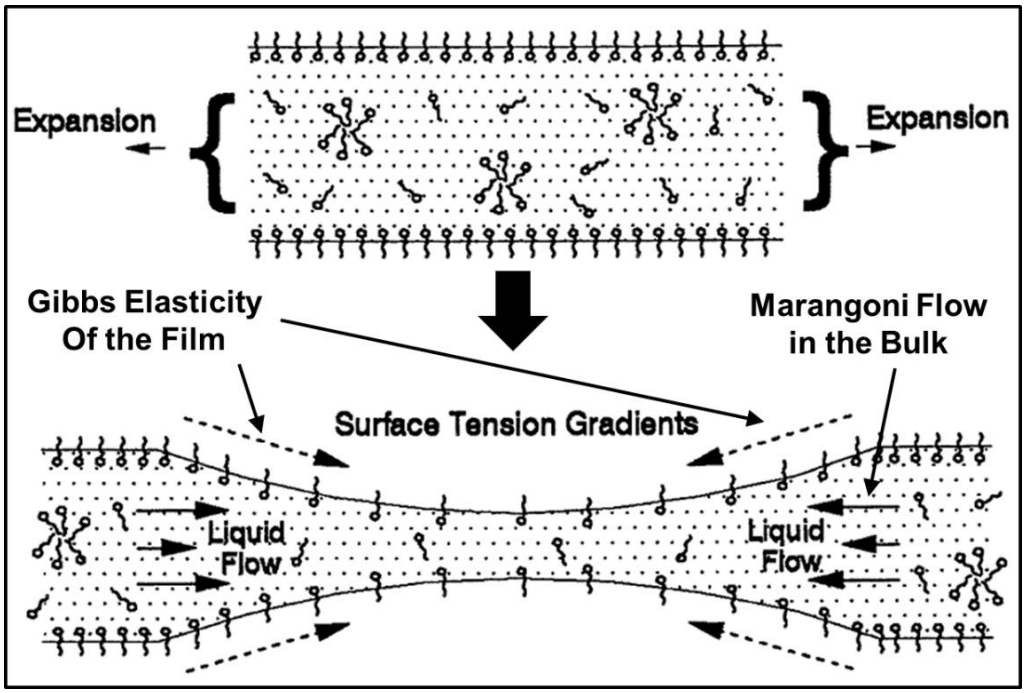

Figure 2.4: Illustration of the Gibbs-Marangoni effect (Schramm, 1994)

2.5 Types of Drilling Foams

Foam is a colloid comprising of the dispersed gas phase in the liquid continuous phase. Foams with liquids as the continuous phase are subcategorized based on the type of base fluid used into aqueous-based, polymer-based, and oil-based foams. The following sections will briefly discuss rheological studies involving all three kinds of foams.

2.5.1 Aqueous Foams

Aqueous foams (also called “stable foams”) are commonly used for cleanout and drilling operations. Surfactant is added to water to aid in the foaming procedure, while, air and inert gases

(like N_2) are used as the dispersed phases. Additives like salts and corrosion inhibitors are added to improve foam behavior for drilling applications without affecting their rheological properties.

Earlier studies treated foam as suspension of bubbles in the continuous phase (Mitchell, 1970); however, other studies (Patton *et al.*, 1983) oppose this approach since foam bubbles slip and deform in shear-induced flow. Moreover, shear gradients will not be constant as the bubbles deform and coalesce continuously.

Most foam rheology studies concluded that aqueous foams behave like pseudoplastic fluids at high shear rates (Martins *et al.*, 2001; Raza and Marsden, 1967; Sanghani and Ikoku, 1983). However, at low shear rates, foam exhibits Bingham plastic (Sanghani and Ikoku, 1983) or Herschel-Bulkley (Bonilla and Shah, 2000) fluid behaviors. Moreover, yielding behavior is more pronounced in high-quality foams (Akhtar *et al.*, 2018). In some cases, wall-slip was reported at high shear rates when low-quality foams were flowing in small diameter pipes (David and Marsden, 1969; Herzhaft, 1999). Wall slip was more reported in smooth pipes (Thondavadi and Lemlich, 1985). Beyer *et al.* (1972) developed expressions for slip velocity during the steady-state flow of aqueous foams. Chen *et al.* (2005b) used a roughened-cup Couette type rotational viscometer to characterize aqueous drilling foam rheology and observed shear-thinning pseudoplastic behavior.

Few studies (Akhtar *et al.*, 2018; Bonilla and Shah, 2000) investigated foam flow behavior at elevated temperatures. All fluids show shear thinning behavior, which steadily decreases with temperature. This is attributed to thermal thinning of the liquid phases and the bubble film which destabilizes the foam and thereby limits the maximum achievable foam quality.

2.5.2 Polymer-Based Foams

Polymer-based foams are also called “gelled foams” or “stiff foams” (Ahmed et al., 2003). They are prepared by adding foaming agents (surfactants) and other additives to viscosify the liquid phase. Some of the polymers used to viscosify the liquid phase are hydroxyl propyl guar, xanthan, hydroxyethyl cellulose (HEC), poly-anionic cellulose (PAC). Stiff foams display structures similar to those found in aqueous foams; however, they are more stable. Hence, they can form higher quality foams. The viscosity of gelled foams depends greatly on the viscosity of the base liquid and foam quality.

Guar is a linear gel and commonly used as a base fluid additive for foam fracturing applications. Rheology of guar-based foams displayed a viscosity reduction at high foam qualities, which is attributed to retarded diffusion of surfactants to the film layer (Harris, 1989; Harris and Heath, 1996; Harris and Pippin, 2000). Khade and Shah, (2004) developed empirical correlations for pseudoplastic model parameters at ambient and elevated temperatures. Hydroxy-propyl-guar (HPG) is a propylene glycol ether of guar and used as a substitute for guar in foam fracturing. Most studies conducted on HPG-based foam showed similar rheological behavior as guar-based foams (Enzendorfer *et al.*, 1994; Harris, 1985; Phillips *et al.*, 1987; Tan and McGowen, 1991); however, Reidenbach *et al.* (1986) observed yielding pseudoplastic behavior in HPG-based foams. The viscosities of guar and guar-co-polymer-based foams decrease with temperature; however, the level of reduction is still smaller than the corresponding gelled fluids (Cawiezel and Niles, 1987a; Harris and Reidenbach, 1987). Exhaustive investigations (Harris, 1985; Hutchins and Miller, 2003) have been performed to assess the effects of bubble structure and distribution on rheology and stability of foam, especially in the presence of additives.

Cellulose-based polymers like HEC and PAC have been recently been used to viscosify base fluid for foam generation. Studies (Babatola, 2014; Sherif *et al.*, 2015a) on cellulose-based foam show power-law behavior at high shear rates, although at low shear rates they display yielding behavior which can be modeled as a Bingham plastic (Khan *et al.*, 1988) or Herschel-Bulkley (Akhtar, 2017) fluid. As expected, foam viscosity increased with foam quality and base liquid polymer concentration. Chen *et al.* (2005a) reported wall-slip in low-quality foams that increases with base polymer concentration. Additionally, the viscosity of HEC based foam decreased with temperature (Akhtar, 2017).

Xanthan gum (XCD) is a polysaccharide that is used as a thickening and stabilizing agent for many industrial operations. Generally, XCD-based foams display yielding behavior, which has been identified with the use of a vane rheometer (Saintpere *et al.*, 2000a). XCD-based foams are best modeled as a yield pseudoplastic fluid. In fact, it was observed that at low shear stresses, they behave like elastic solids but and at higher shear stresses, they display viscoelastic liquid characteristics. Similar findings were reported by (Sani *et al.*, 2001) who also noted that the direct relationship between foam viscosity and its quality and base liquid rheology. XCD-based foams showed wall slip as confirmed microscopic image analysis (Herzhaft, 2002). Additionally, it has been found that the viscosity of XCD-based foams decreases with an increase in temperature (Sani *et al.*, 2001).

2.5.3 Oil Based Foams

Oil-based foams are prepared using either diesel, a mixture of diesel and mineral oil, or mineral oil as the base liquid and an oil-soluble foaming agent. Few studies (Sherif *et al.*, 2015b) have been performed on the flow behavior of oil-based foam until recently. Sherif *et al.* (2015b)

observed the non-Newtonian behavior of oil-based foams. Similar to that of most polymer-based fluids, their viscosity has been found to be mainly a function of quality and base liquid viscosity.

Previously, oil-based foam has been used successfully in fracturing operations due to their superior fluid loss properties (Driscoll *et al.*, 1980). Also, they are in drilling operations due to their superiority in fluid loss control, minimization of formation damage and differential pipe sticking, improving bit life, increasing rate of penetration, reducing gas influx, and improving high-temperature stability (Kakadjian *et al.*, 2003; Sepulveda *et al.*, 2008). The high-temperature stability of foam systems that use two organo-phillic phases (crude oil, diesel, or mineral oil as base liquid and N_2 as the gaseous phase) can be increased by the addition of flouro-surfactants and/or silicon-based surfactants. Moreover, the base liquid can be viscosified further by using co-polymers, that show shear-thinning behavior (Sepulveda *et al.*, 2008).

2.6 Foam Rheology Models

Several studies attempted to characterize foam rheology using different modeling approaches, namely, empirical, analytical, and semi-empirical. Each of these approaches has its own advantages and limitations. The following sections will briefly review different literature published in each category.

2.6.1 Mathematical Models

Foam flow is characterized by the rupturing, deformation, and rearrangement of bubbles. Under steady flow conditions, bubble deformation reaches an equilibrium value and the magnitude of deformation is characterized by the dimensionless capillary number, Ca (Ahmed *et al.*, 2003a; Rust and Manga, 2002; Truby *et al.*, 2014),

$$Ca = \frac{r_b \dot{\gamma} \mu_F}{\sigma} \tag{2.3}$$

where, r_b is Average bubble radius, $\dot{\gamma}$ is the shear rate, μ_F is foam viscosity and σ is interfacial tension (surface tension).

Foams are extensively used for drilling, completion and work-over applications because of its light density and high viscosity. It is extremely critical to have a thorough understanding of foam rheology for successful planning and execution of field operations like underbalanced drilling. Several studies (Barthes-Biesel and Chhim, 1981; Batchelor, 1967; Frankel and Acrivos, 1970; Khan and Armstrong, 1986; Llewellin *et al.*, 2002; Mader *et al.*, 2013; Rust and Manga, 2002) have attempted to establish a relationship between the capillary number and foam viscosity. Mathematical modeling of foam rheology is difficult, largely due to poor understanding of its microscopic structure (Ahmed *et al.*, 2003a). Flow in bubbly suspension causes the deformation of bubbles instead of rearrangement. In a steady, bubble deformation reaches an equilibrium state and the magnitude of deformation is characterized by the dimensionless capillary number, Ca (Truby *et al.*, 2014).

The capillary number is the ratio of viscous forces which tend to deform spherical bubbles to the surface tension, which favors bubble sphericity. Therefore, it indicates the potential for bubble deformation. Bubbles obstruct flow lines in a flow field while simultaneously provide a free slip surface within suspending medium. When $Ca \ll 1$, interfacial forces dominate and bubbles remain spherical, which causes maximum distortion of flow lines and provides fewer slip-surfaces. This leads to an increase in the suspension viscosity (Ahmed *et al.*, 2009). However, when $Ca \gg 1$ viscous forces dominate, elongating bubbles along flow direction, causing lesser flowline distortion with greater free slip area, hence suspension viscosity decreases (Llewellin and

Manga, 2005). Therefore, there exist two regimes that are distinguished based on the values of capillary numbers (Figure 2.5). At extremely high or extremely low capillary numbers, asymptotic viscosity is observed which is a function of bubble fraction, $_b$.

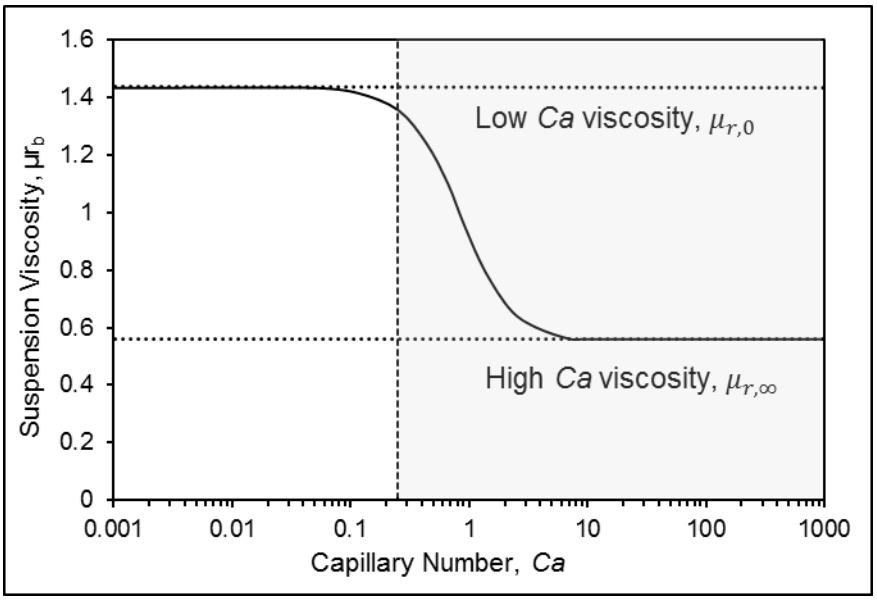

Figure 2.5: Relative bubble suspension viscosity as a function of Capillary number, *Ca*, for Φ_b = 0.3 (Truby *et al.*, 2014)

Mathematical or theoretical models developed for suspension flows of solids and emulsions are often applicable for foams. The simplest linear model was proposed by Einstein (1906) that assumed foams to be a single-phase fluid with viscosities significantly greater than those of its components. He used energy balance in two-phase flow to formulate an equation for the viscosity of foams (μ_F) with qualities lower than 0.52 (Eq. 2.4). The basic assumptions for his model are: i) spherical particles/bubbles suspended in a homogenous fluid, ii) all particles are similar with identical volumes and diameters, iii) particles are uniformly spaced with no interactions among them, and iv) no-slip at the particle surface.

$$\mu_F = \mu_L(1 + 2.5\Gamma) \tag{2.4}$$

For intermediate foam qualities (between 0.52 to 0.74), Hatschek (1911) considered bubble-interference and bubble-deformation in his dissipation energy analysis. Therefore, additional energy input, which is required to initiate and maintain flow is included in the rheology model. This additional amount of work is reflected with an increase in the viscosity of foam. Therefore, foam quality which is basically the concentration of bubbles per unit volume has a higher coefficient (Eq. 2.5a). Moreover, for high-quality foams (quality greater than 0.74), bubbles assume the shape of parallelepipeds resulting in a sharp increase in viscosity with quality (Eq. 2.5b).

$$\mu_F = \mu_L(1 + 4.5\Gamma) \qquad \text{for } 0.52 < \Gamma < 0.74 \tag{2.5a}$$

$$\mu_F = \mu_L/\left(1 - \Gamma^{1/3}\right) \qquad \text{for } \Gamma \geq 0.74 \tag{2.5b}$$

Batchelor (1967) used Navier-Stokes equations to develop a model for the viscosity of a dilute suspension of small particles. The term "suspension" applied to the system of both solids and liquids dispersed in either gas or liquids. The flow was equated to the case of sphere immersed in a pure straining motion and the main assumptions of the model are: i) negligible effects of gravity and inertia on the motion of the suspended particles, ii) particles having spherical geometry, and iii) capillary number much smaller than "1". The final model obtained is simplified and presented elsewhere (Ahmed *et al.*, 2009).

$$\frac{\mu_{sus}}{\mu_L} = 1 + \Gamma\left(\frac{1 + 2.5\lambda}{1 + \lambda}\right) \tag{2.6}$$

where λ is the ratio of the viscosity of the dispersed phase to the continuous phase ($\lambda = \mu_{Dis}/\mu_{Con}$); μ_{sus} is the viscosity of the suspension. It should be noted that the above relation holds

true for low-quality foams. At high foam qualities, neighboring bubbles interfere with the disturbance of flow created by another bubble.

Constitutive equations for dilute suspension of spherical microcapsules (or bubbles enclosed in an elastic membrane in case of foams), which describes the viscosity as a function of the capillary number, Ca, was developed by Barthes-Biesel and Chhim, (1981). The resulting equation displays both shear and normal viscosity effects for the capsules. As opposed to Batchelor (1967) "spherical particle" suspension that deformed elastically when submersed in an externally imposed flow, the internal phase in "capsules" behave like liquid droplets and their elastic interface deforms as solids. The model assumes minimal interaction between capsules and streamlined low-shear flows (i.e. $Ca \ll 1$). The final expression displays stress-strain relation where coefficients are dependent on the physical properties of the suspended capsule and it is expressed as:

$$\frac{\mu_{sus}}{\mu_L} = 1 + \Gamma[2.5 - Ca^2(68.463 - 20.982\psi + 59.375\lambda)] \tag{2.7}$$

where ψ is parameter accounting for non-linear behavior of foam films.

A two-dimensional model for foam viscosity presented by Khan and Armstrong (1986) in terms of foam quality and cell properties. The model is valid for dry foams ($\Gamma > 0.945$) when the capillary number is in the order of "1". It is developed assuming the hexagonal, monodisperse structure of foam cells that reform themselves after deformation in direction of flow cells. The model has been simplified by (Ahmed *et al.*, 2003a) as:

$$\frac{\mu_F}{\mu_L} = \frac{0.31}{Ca} + 26\sqrt{\Gamma}\left(1 - \sqrt{\Gamma}\right) \tag{2.8}$$

When the capillary number is sufficiently large, the first term becomes very small, which implies that foams display a constant viscosity value at a given quality.

A rigorous theoretical model for transient relative viscosity of emulsions has been presented by Frankel and Acrivos (1970). Major assumptions of the model involve i) negligible droplet/gas viscosity with respect to continuous viscosity, ii) very dilute solution, and iii) small deformation of bubble droplets (Mader *et al.*, 2013). In special cases where $\lambda = 0$, the equation was simplified by Rust and Manga (2002) and is given as:

$$\frac{\mu_F}{\mu_L} = 1 + \frac{\Gamma(1 - 2.4\,Ca^2)}{(1 + 1.44\,Ca^2)} \tag{2.9}$$

For $Ca \to 0$ and $Ca \to \infty$, special relations for relative viscosity can be obtained for both the asymptotic regions which are both independent of capillary number.

Most numerical models make assumptions to simplify the mathematical problem, which in turn limits their applicability to predict foam behavior. For example, most models (Barthes-Biesel and Chhim, 1981; Batchelor, 1967) assume the base liquid and the suspended fluid to be Newtonian and incompressible, which is not accurate in gas suspensions or in stiff foams, which is compressible and non-Newtonian. Moreover, liquid droplets are much more viscous than gas bubbles. The internal energy in gases is much higher than that in liquids which makes the surface tension an important criterion. Incorporating surface tension leads to nonlinearity in the constitutive equation. Finally, due to the stark density difference bubble solution cannot be considered neutrally buoyant and randomly dispersed (Llewellin *et al.*, 2002). Thus, the limitation of the theoretical approach lies in the complexity of understanding the underlying mechanisms.

2.6.2 Semi-Empirical Models

Assumptions to simplify the mathematical problem makes the theoretical model too simplistic to represent the foam rheology accurately. Hence, many researchers used experimental approaches to validate theoretical models, especially in foams. This forms the basis for the semi-

empirical modeling approach of foam viscosity. Semi-empirical models are developed using a combination of theoretical relations to define a physical phenomenon and empirical expressions for determining the constants. These models can be applied in conditions similar to the ones in which they were developed. Moreover, the validation of semi-empirical models may be a concern, though not as big as that for theoretical models. In some cases, this modeling approach is advantageous because researchers can propose a hypothesis based on experimental observations and then perform modified experiments to prove or disprove those hypotheses. Most of the works are restricted to the flow of bubbly liquids in magma (viscous base fluid) at low capillary numbers. Ahmed *et al.* (2009) stated that gas volume fraction effects suspension viscosity differently in high viscosity base fluid.

Rust and Manga (2002) combined experimental data from a Couette rheometer with other empirical correlations for very high ($Ca \gg 1$) and very low ($Ca \ll 1$) Capillary numbers using a Cross equation to obtain a single semi-empirical constitutive equation for surfactant-free bubbly suspensions (Figure 2.5).

$$\mu_r = \frac{\mu_F}{\mu_L} = \mu_{r,\infty} + \frac{\mu_{r,0} - \mu_{r,\infty}}{(1 + 1.44\ Ca^2)} \tag{2.10}$$

where, μ_r is the relative viscosity at arbitrary Ca; $\mu_{r,0}$ and $\mu_{r,\infty}$ are relative viscosities at extremely low and high capillary numbers, respectively. Truby *et al.* (2014) used the model presented by Rust and Manga (2002) and developed generalized expressions for both the dilute limit and extremely high capillary number range. Further experimental investigations demonstrated that the transition between the two asymptotic regimes occurred in a fairly narrow range of Capillary numbers ($Ca \approx 1$).

$$\mu_{r,0} = (1 - \phi_b)^{-1} \tag{2.11a}$$

$$\mu_{r,\infty} = (1 - \phi_b)^{-5/3} \tag{2.11b}$$

Prud'homme and Khan (1996) performed theoretical analysis assuming exponential viscosity relation proposed by Mooney (1951) for monodisperse suspensions, to describe the rheological behavior of emulsions and foams. The viscosity of dilute emulsions at high shear rates is a function (Eq. 2.12) of both the oil volume fraction and the viscosity ratio, λ, of internal (dispersed) and external (continuous) phases ($\lambda = \mu_{Dis}/\mu_{Con}$).

$$\mu_r = \frac{\mu_F}{\mu_L} = exp\left(\frac{K\Gamma}{1-\Gamma}\right) \qquad \text{for } \Gamma \leq 0.5 \tag{2.12a}$$

$$K(\lambda) = \frac{5}{2}.\frac{0.4 + \lambda}{1 + \lambda} \tag{2.12b}$$

where, μ_F = foam viscosity and μ_L = base liquid or continuous phase viscosity. However, in the case of foams λ reduces to zero.

As can be seen from Eq. (2.12a) that the bubble size does not influence the foam viscosity. The number of bubble-to-bubble hydrodynamic interactions is a function of the number of bubbles per unit volume of foam or the bubble size, making the viscosity a function of bubble size distribution. In higher-quality foams, decreasing the smaller bubble sizes resulted in higher viscosities, due to increased interactions per unit volume.

Based on deformation study of closed packed bubble microstructure in highly concentrated oil-in-water emulsions at low shears ($Ca \leq 10^{-4}$), Princen and Kiss (1989) formulated semi-empirical equations for yield stress and relative viscosity of foams. Yield stress as a function of surface tension, volume fraction and bubble size are given as:

$$\tau_Y = \sigma \Gamma^{1/3} Y(\Gamma)/a \qquad \text{for } \Gamma \geq 0.74 \tag{2.13}$$

where σ is surface tension; a is surface volume based mean drop radius; and $Y(\Gamma)$ is a viscosity function to characterize the effect of quality on yield stress and roughly equates to $Y(\Gamma) = 0.08 - 0.114 \log(1 - \Gamma)$.

The expression for relative viscosity was written as:

$$\mu_r = \frac{\mu_F}{\mu_L} = \frac{Y(\Gamma)\Gamma^{1/3}}{Ca} + \frac{32(\Gamma - 0.73)}{Ca^{1/2}} \tag{2.14}$$

Llewellin *et al.* (2002) presented a simple linear constitutive equation for dilute ($\Gamma < 0.5$) bubbly suspension for very small deformations ($Ca \ll 1$) based on analysis conducted by Frankel and Acrivos (1970). The model was validated based on data obtained from parallel plate rheometer and the best fit obtained is given as:

$$\mu_r = \frac{\mu_F}{\mu_L} = (1 + 9\Gamma) \tag{2.15}$$

2.6.3 Empirical Models

A purely empirical or statistical modeling approach involves the formulation of statistical expressions using only experimental data or historical studies do describe a material property. Empirical relations do not have any physical basis, but they do help in the interpretation of experimental data. Empirical expressions are limited in their applicability to the conditions identical to the one in which the relationship was developed. Some of the empirical foam rheology models developed in the past are discussed in this section.

Based on tests conducted over a wide range of foam qualities, Mitchell (1970) concluded that: i) at high shear rates, foam viscosity is only dependent on foam quality, ii) for a fixed shear rate, viscosity increases with foam quality, iii) for qualities less than 54%, foam behaved like a

Newtonian fluid, iv) for qualities greater than 97%, the fluid system behaves like a mist flow with slugs of air flowing intermittently along with the foam, and v) stable foams do not exhibit slippage. Therefore, foam quality is the main factor affecting foam viscosity. Foam behaved like a Newtonian fluid below 54% quality and like a Bingham Plastic above 54% quality. No wall slippage was observed in his studies.

$$\mu_F = \mu_L(1 + 3.6\Gamma) \qquad \text{for } \Gamma \leq 0.54 \tag{2.16a}$$

$$\mu_F = \mu_L(1 - \Gamma^{0.49})^{-1} \qquad \text{for } \Gamma \geq 0.55 \tag{2.16b}$$

A similar study Beyer *et al.* (1972) conducted a laboratory scale and pilot scale experiments and observed a Bingham plastic behavior of the foam fluid. After correcting data for wall slip, expressions for plastic viscosity and slip velocities are generated. Foam quality and velocity were found to impact foam flow behavior, while surfactant concentration did not have a significant effect on friction pressure drop. In the analysis, the flow was assumed to be steady-state, isothermal and laminar. Based on this, the equation for Bingham Plastic fluid is given as:

$$\tau - \tau_Y = \mu_p\dot{\gamma}/144 \qquad \text{for } \tau \geq \tau_Y \tag{2.17}$$

where τ is the local shear stress; τ_Y is yield shear stress; $\dot{\gamma}$ is the shear rate; μ_p is Plastic viscosity. The value of yield stress obtained from pilot tests was 4.65 Pa and its value was independent of foam quality. The expressions for plastic viscosity are:

$$\mu_p = 1/[7200(1 - \Gamma) + 267] \qquad \text{for } 0.9 \leq \Gamma \leq 0.98 \tag{2.18a}$$

$$\mu_p = 1/[2533(1 - \Gamma) + 733] \qquad \text{for } 0.75 \leq \Gamma \leq 0.9 \tag{2.18b}$$

Based on the theories of Einstein (1906) and Hatschek (1911) and laboratory measurements of Mitchell (1970), Blauer *et al.* (1974) developed a plot for plastic viscosity of foam as a function of foam quality The study proposed three models to determine foam viscosity. The study suggested

that spherical gas bubbles in low quality (between 0 to 0.52) foams are uniformly dispersed and do not interact with one another. At foam qualities of 0.52, the spherical bubbles become packed in a loose cubical arrangement and begin interfering with each other while flowing. Above qualities of 0.74, bubbles do not assume the spherical shape and deform to form parallelepipeds.

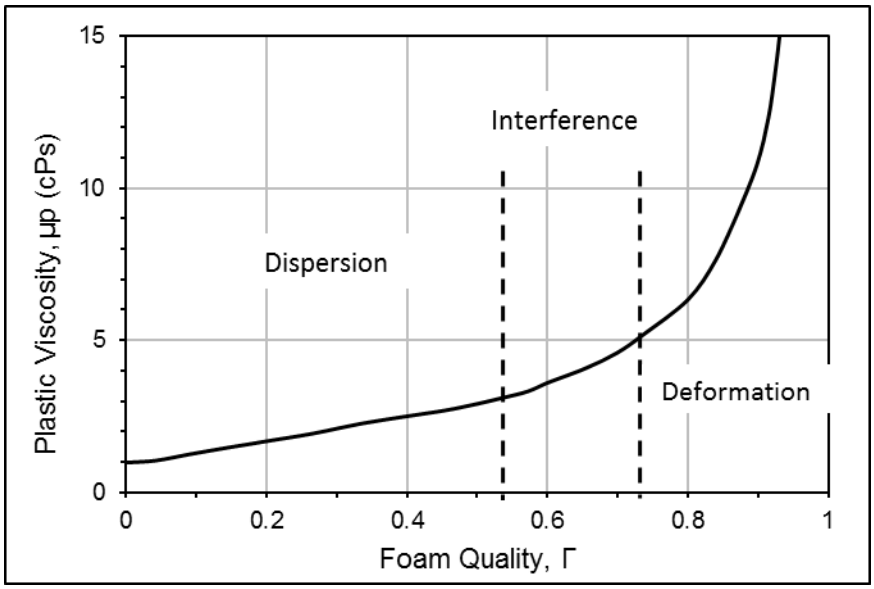

Figure 2.6: Bingham plastic viscosity of foam (Blauer *et al.*, 1974)

To account for non-Newtonian behavior of foam, Blauer *et al.* (1974) used effective viscosity (μ_e) concept, which combines the plastic viscosity, μ_p, and yield strength of foams, τ_Y, for determination of the Fanning friction factor. The effective viscosity in Bingham plastic foam is expressed as:

$$\mu_e = \mu_p + \frac{g_c \tau_Y D}{6u} \tag{2.19}$$

where u = fluid velocity.

Using a concentric annular viscometer, Sanghani and Ikoku (1983) investigated stable foam rheology for a wide range of shear rates (150 to 1000 s^{-1}). Foams behaved as pseudoplastic fluid, and flow behavior index, *n*, and fluid consistency index, *K* were determined and related to

foam quality. They also developed correlations for friction factor and pressure calculations. Recently, their measurements are used by Li and Kuru (2005) to develop better expressions for n_{F} and K_{F} for different foam quality ranges.

$$n_F = 1.2085\, e^{3.5163\Gamma} \qquad \text{for } \Gamma \leq 0.915 \tag{2.20a}$$

$$n_F = 2.5742\Gamma - 2.1649 \qquad \text{for } 0.915 \leq \Gamma \leq 0.98 \tag{2.20b}$$

and expression for foam consistency index:

$$K_F = 0.3543\, e^{-1.9897\Gamma} \qquad \text{for } \Gamma \leq 0.915 \tag{2.21a}$$

$$K_F = -102.8175\Gamma + 103.2723 \qquad \text{for } 0.915 \leq \Gamma \leq 0.98 \tag{2.21b}$$

Investigation of the rheology of aqueous and guar gel-based foams revealed a yield pseudoplastic behavior (Bonilla and Shah, 2000). Foam fluids with qualities varying between 0 to 80% in a temperature range of 75 to 175°F were tested at 1000 psi pressure in a recirculating loop under laminar flow condition. Shear stress plotted against nominal Newtonian shear rate, for two different pipe sizes confirmed the absence of wall slip. Both foam and base liquid had the same flow behavior index, while, correlations for foam consistency index, K_F, were formulated in reference to base liquid consistency index K_L (Eq. 2.22a). A model for yield stress, τ_Y, has also been developed (Eq. 2.22b).

$$\frac{K_F}{K_L} = e^{(C_1\Gamma + C_1'\Gamma^2)} \tag{2.22a}$$

$$\tau_Y = C_2 e^{(C_2' + C_2''\Gamma)} \tag{2.22b}$$

where, $C_1, \mathrm{C}_1', C_2, \mathrm{C}_2'$ and $\mathrm{C}_2^{''}$ are empirical constants that depend on the type of base fluid. Khade and Shah (2004) incorporated the effect of temperature while developing empirical relationships for power-law model parameters in guar-based foams. They observed that the flow behavior index of the base liquid showed variation with guar concentration and its value increased with

temperature. The fluid consistency index decreased with temperature but showed no dependence on base gel concentration. The authors further presented correlations for the consistency index of foam which is similar to Eq. (2.22a) and for flow behavior index as relative to that of the base liquid (Eq. 2.23). A comparative study of new model predictions with older works by Mitchell (1970) and Reidenbach *et al.* (1986) was performed to check its effectiveness for predicting experimental data.

$$\frac{n_F}{n_L} = 1 + C_3 \Gamma^{(C_3')} \tag{2.23}$$

where, C_3 and C_3' are functions of different guar-based liquids.

Sani et al. (2001) observed yield pseudoplastic behavior of both Xanthan base fluid and its foam. They used temperature corrections for both flow behavior index and fluid consistency index to determine accurate base fluid rheology before generating correlations for model parameters of Xanthan foams. They assumed the flow behavior index of foams to be same as that of the base fluid and developed expressions for foam consistency index, K_F, and yield stress, τ_Y, of the form shown in Eq. (2.23).

More recently, rheological investigations of oil-based foams (OBF) and HEC based foams have been performed (Sherif *et al.*, 2015a, 2015b). The bubble size distribution has been related to foam quality. Both foams displayed wall slip at high shear rates and displayed pseudoplastic behavior. The article presented correlations to evaluate relative power-law parameters for oil-based foam fluids in a quality range of 34% to 68% for OB foams and between 45-70 % for HEC based foams of the general form shown in Eq. (2.24).

$$\frac{K_F}{K_L} = \left(C_4 e^{C_4'\Gamma} + 1\right) \tag{2.24a}$$

$$\frac{n_F}{n_L} = \left(C_5 e^{C_5'\Gamma} + 1\right)^{-1} \tag{2.24b}$$

where, C_4, C_4', C_5, and C_5' are constants obtained by statistical analysis for different base liquid types.

Gu and Mohanty (2015a) performed a rheological investigation of three variations of polymer-free aqueous foam fracturing fluids using a recirculating pipe viscometer for the temperature range of 95 to 155°F, quality range of 25 to 84%, and pressure range of 100 to 2000 psi. Two fluids contained regular anionic surfactant with and without glycerol, while the third fluid was prepared using a viscoelastic surfactant. All three foams displayed pseudoplastic behavior. Apart from rheology measurements, they also analyzed the bubble flow regime using a view cell. The correlations for power-law parameters for aqueous foams were developed as functions of quality and pressure. The flow behavior index was given as:

$$n_F = 1.54 - 1.64\Gamma^2 \qquad \text{for } 0 \leq \Gamma \leq 0.6 \tag{2.25a}$$

$$n_F = 1.54 - 1.64\Gamma^2 - (0.89Q - 0.211)[log(P/1000)] \qquad \text{for } 0.6 \leq \Gamma \leq 0.85 \tag{2.25b}$$

Consistency index for aqueous foams:

$$K_F = 10^{(5.89\Gamma^2 + 0.43\Gamma - 4)} \qquad \text{for } 0 \leq \Gamma \leq 0.6 \tag{2.26a}$$

$$K_F = 10^{(5.89\Gamma^2 + 0.43\Gamma - 4)} + 8.6 \times 10^{-11}.e^{21\Gamma}.(P - 1000) \qquad \text{for } 0.6 \leq \Gamma \leq 0.85 \tag{2.26b}$$

Babatola (2014) conducted flow experiments with PAC based fluids at ambient conditions and 100 psi system pressure. Empirical relations were developed for relative power-law parameters which were a function of foam quality and base fluid concentration. More recently, Akhtar (2017) conducted experiments with aqueous and PAC based foams in a smaller setup at elevated

temperatures (75 to 225°F) and high pressures (1000-3000 psi). The study showed the minor influence of pressure on foam rheology (i.e. no seconding effect of pressure on rheology). Correlations have been developed for relative power-law parameters as function of quality, fluid type, and temperature. Flow behavior index for both aqueous and PAC foams obeyed the general form:

$$\frac{1}{n_F} = C_6 + \frac{C_6'}{\left[1 + exp\left(\frac{\Gamma - C_6''}{C_6'''}\right)\right]} \tag{2.27}$$

The relative fluid consistency indexes of aqueous and PAC foams are described using the exponential function.

$$\frac{K_F}{K_L} = exp\left\{C_7 + \frac{C_7'}{\left[1 + exp\left(\frac{\Gamma - C_7''}{C_7'''}\right)\right]}\right\} \tag{2.28}$$

where, $C_6, C_6', C_6'', C_6''', C_7, C_7', C_7''$, and C_7''' are functions of fluid type and temperature.

For high-quality PAC foams (greater than 65%) a slightly different expression has been proposed for greater accuracy.

$$\frac{K_F}{K_L} = C_8 \cdot exp\left[\frac{-(\Gamma - C_8')^2}{2C_8''^2}\right] \tag{2.29}$$

where, C_8, C_8', and C_8'' are dimensionless parameter functions of temperature.

2.7 Wall Slip

No-slip boundary condition implies that the fluid element in contact with the boundary wall has zero velocity. However, many polymers solutions, melts, gels, emulsions, dispersions, and foams display wall slippage. The wall slippage produces a higher flow rate. It is often identified by plotting the rheograms (plots of wall shear stress versus nominal Newtonian wall shear rate) of

foam gathered in varying pipe sizes. Ideally, the rheograms should coincide, however in presence of wall slip a parallel right-shifting is observed. To reveal the true rheology of a fluid, shear rates need to be corrected for wall slip.

Kraynik (1982, 1988) observed the presence of wall slip in flow through transparent pipes. In general, the observed slip velocities (Kraynik, 1988) were sensitive to wall roughness, volume fraction, and bubble size. Foams when flowing through a pipe tends to form a thin liquid film between the pipe wall and bulk foam (Saintpere *et al.*, 2000b). This thin film acts as a lubricant for the bulk foam thereby lowering the frictional loss and resulting in the right-shifting of flow curves in a rheogram for different pipe diameters. In another study (Coussot, 2014), fluids that displayed yielding behavior were able to flow at wall shear stresses which were well below the yield stress. The use of roughened pipe prevented this behavior of foams. The observations were further supported by the experimental findings of Thondavadi and Lemlich (1985), in which they observed wall slip in smooth acrylic pipes but not in rough galvanized steel pipes.

2.8 Yielding Behavior of Foams

Foams display solid-like behavior at high foam qualities (greater than 70%); and therefore, exhibit yield stress (Gopal and Durian, 1999, 2003; Prud'homme and Khan, 1996). At high qualities, bubbles are jammed together and unable to flow freely around each other. Therefore, when they are subjected to low shear, they deform rather than rearrange. Bubble film stretches and increases the surface energy of the system. The resulting imbalance provides the restoring force, very is much similar to the elastic deformation of solids. Kraynik (1982) provided an expression for critical yield stress at which the fluid starts flowing. Princen (1983) and Prud'Homme (1981) assumed a hexagonal pencil stack model of a two-dimensional monodisperse foam, in which, shear deformation below the elastic limit is prevented by the interfacial tension. Plastic deformation

occurs above the yield stress and which leads to the sliding of the top row by one cell width in the direction of the shear. Therefore, below the yield stress, foam flows as a "bulk" and only once the yield stress is exceeded sheared fluid flow appears. This idealized "rolling" of the top cell stack is not possible in three-dimensional foams because the cells acquire a polyhedral shape. At higher pressure gradients the yield stress is exceeded which leads to the continual shearing of the bulk foam near the wall. Lower apparent viscosity values are recorded.

2.8.1 Measuring Yield Stress

Nguyen and Boger (1992) proposed three methods to determine the yield stress of foams. The methods include i) direct measurements using "vane rheometer", ii) measuring elastic modulus at different strains, and iii) extrapolating low shear rate measurements.

Vane Rheometer: Vane rheometer has a co-axial geometry and the spindles in a "vane rheometer" comprise of flat blades with a radial length, R_{Vane} (Figure 2.7). The vanes are placed in a container whose dimensions are much larger than R_{Vane} . The vanes prevent the foams from slipping, while the larger cup size keeps stress levels low at the outer boundary, so that yield only occurs at the tips of the vanes.

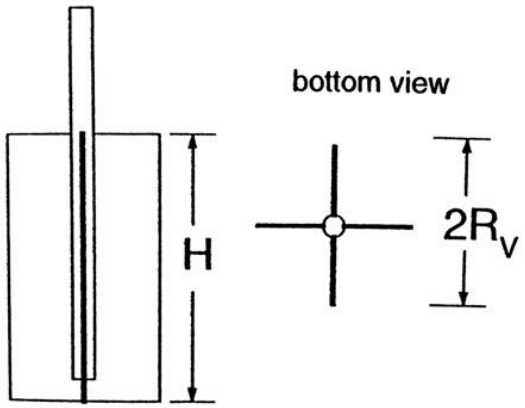

Figure 2.7: Vane rheometer spindle arrangement (Prud'homme and Khan, 1996)

For yield stress measurement, the "stress relaxation" method is used. A foam sample is placed in a rheometer and exposed to an increasing torque and the angular deflection at the end of each torque increment is plotted against time (Figure 2.8). Below yield stress, fluid behaves as an elastic medium and the vane assumes a new deflection. When yield stress is reached, fluid shears and vanes begin to rotate (Figure 2.8). Critical torque imposed, T is converted to yield stress as follows:

$$\tau_Y = \frac{T}{2\pi(R_{vane})^2} \Big/ \left[\frac{H_{bob}}{R_{vane}} + \frac{1}{3}\right] \tag{2.30}$$

where, H_{bob}= length of the bob; R_{vane} = vane radius.

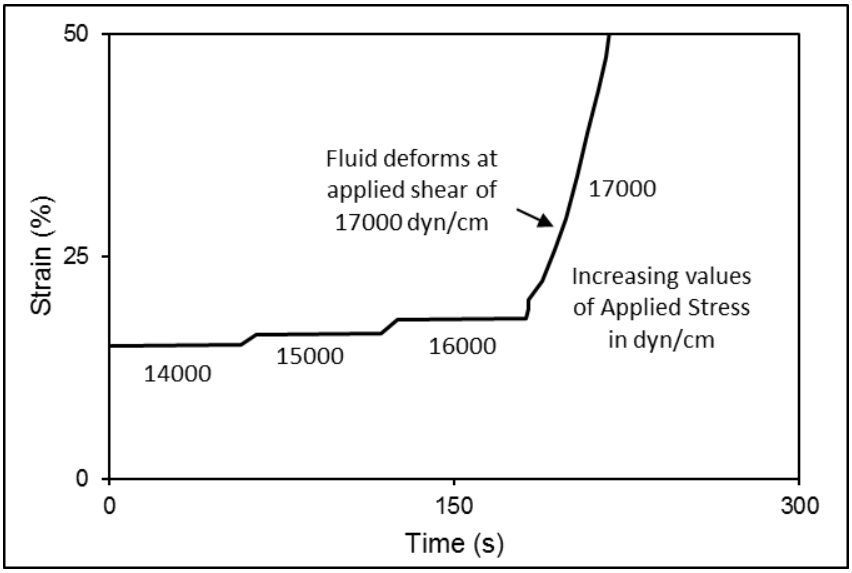

Figure 2.8: Angular deflection vs. time for incremental shear stress (Prud'homme and Khan, 1996)

Measuring Elastic Modulus at Different Strains: Dynamic oscillatory measurements using a rheometer can be used for yield stress can be determined. The principle involved is that for stresses lower than the yield stress, foam behaves like an elastic solid with elastic modulus, G'. Yield stress is obtained by multiplying elastic modulus to the critical strain at which the foam starts breaking down and modulus starts decreasing, $\dot{\gamma}_c$.

$$\tau_Y = G'.\dot{\gamma}_c \tag{2.31}$$

where, G'= elastic modulus, $\dot{\gamma}_c$ = critical strain.

Extrapolating Low Shear Rate Measurements: The process of extrapolation from experimental data is subjective and highly dependent on the range of shear rates tested. Reidenbach *et al.* (1986) studied CO_2 and N_2 foams and concluded that they obeyed the Herschel-Bulkley model with a yield stress value, τ_Y. They obtained the power-law index, n, using trial and error and then plotted wall shear stress data versus the nominal shear rate ($8u/d$), raised to nth power on Cartesian coordinates to find yield stress, τ_Y. Finally, they generated empirical correlations for foam consistency index, K_F, and the yield stress, τ_Y, as functions of foam quality:

$$K_F = K_L e^{\mathrm{C}_9\Gamma + \boldsymbol{C}'_9\Gamma^2} \tag{2.32}$$

$$\tau_Y = \mathrm{C}_{10}\Gamma \qquad \text{for } \Gamma \leq 0.6 \tag{2.33}$$

$$\tau_Y = \mathrm{C}_{11} exp^{\boldsymbol{C}'_{11}\Gamma}\Gamma \qquad \text{for } \Gamma \geq 0.6 \tag{2.34}$$

where, $\mathrm{C}_9, \boldsymbol{C}'_9, \mathrm{C}_{10}, \mathrm{C}_{11}$, and $\boldsymbol{C}'_{11}$ are empirical constants functions of the type of gas used (CO_2 or N_2), however, they are independent of the kind of liquid phase used. A similar approach has been used in other studies (Beyer *et al.*, 1972; Blauer *et al.*, 1974; Bonilla and Shah, 2000; Sani *et al.*, 2001) considering either the Bingham plastic model or the Herschel-Bulkley model for foams. Princen (1985) conducted tests with concentrated foams and emulsions to determine yield stress and presented a semi-empirical equation for yield stress that included the effects of the foam structure.

2.9 Modeling of Foam Rheology

2.9.1 Published Measurements

Aqueous Foams: Figure 2.9 compares the published data for 80% quality aqueous foams from different studies. Test conditions were the same for all of these studies (1000 psi, 75°F), except for Duan *et al.* (2008), which was conducted at 600 psi. Highest shear stress values were observed in the case of Akhtar (2017) followed by almost similar readings from both Harris and Heath (1996) and Bonilla and Shah (2000). All the studies used a closed-loop system to generate high-quality foam. The main reason for the differences in the readings is the foam generation method and surfactant type.

Polymer-Based Foams: Figure 2.10 shows data published on HEC based polymer foams, 80% quality all tested at 100 psi, 80%, and 75°F. Even though Chen *et al.* (2005c) used an open-loop system to generate foam, it recorded higher shear stress values. The main reason for the differences in the readings is the foam generation method, base liquid rheology, and surfactant type.

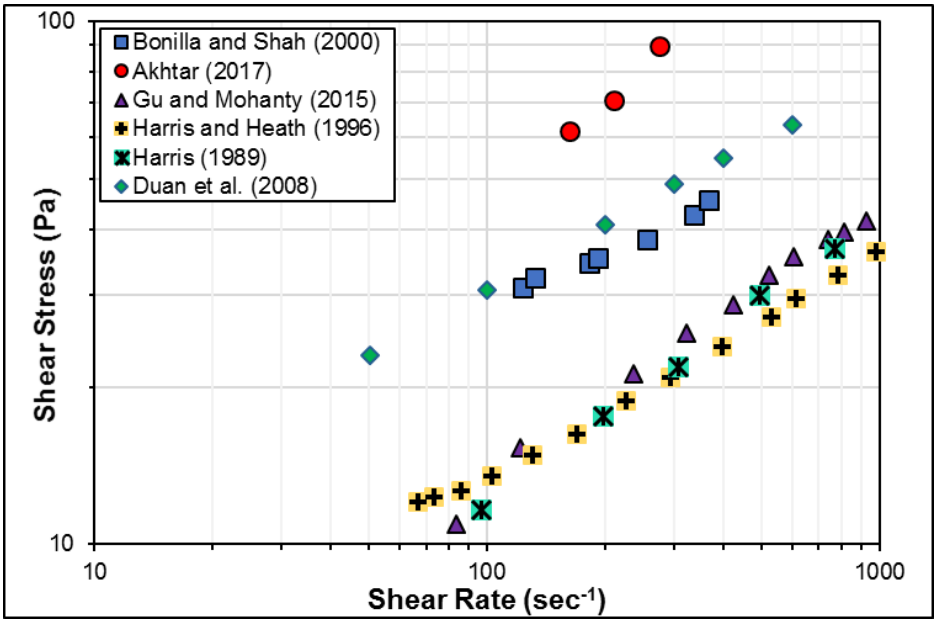

Figure 2.9: Comparison of published data on Aqueous Foams

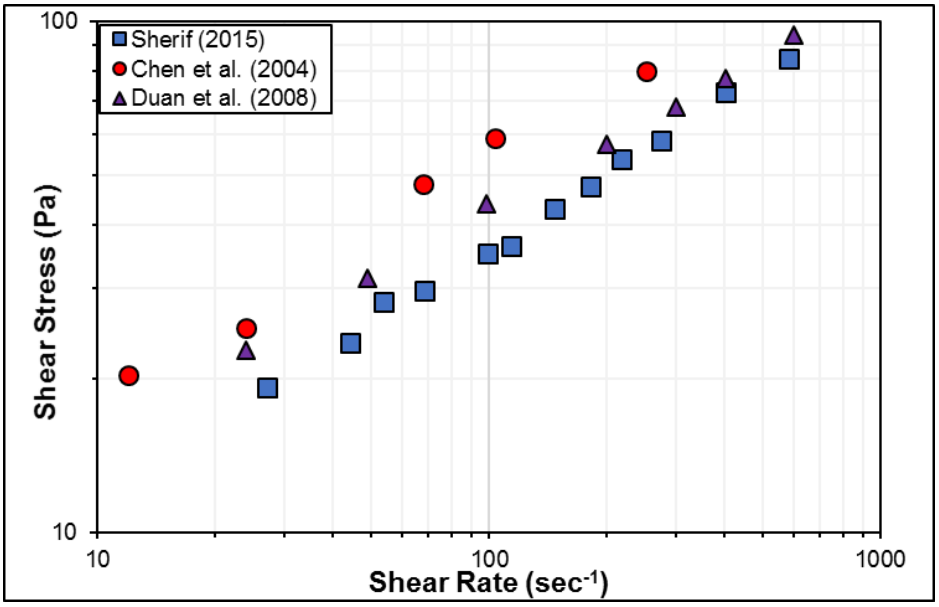

Figure 2.10: Comparison of published data on HEC based Foams

2.10 Factors Affecting Foam Rheology

Due to its inherent structure and compressibility, foam rheology is complex and dependent on quality, pressure, temperature, base liquid properties, foam generation technique, and bubble size and distribution. A brief discussion on the effect of these variables on foam rheology ensues in this section.

2.10.1 Foam Quality

An increase in foam quality leads to more viscous foams. The fluid consistency index of foam increases with the quality and its relative magnitude increases remarkably at higher qualities (Bonilla and Shah, 2000). This behavior is attributed to the transition of a loosely packed bubble regime to a closely packed structure causing greater bubble interactions, which results in an increase in viscosity. Harris (1989) and Herzhaft *et al.* (2005) performed simultaneous measurements of foam flow data and bubble size distribution. With increased foam quality, the bubble size became larger (Figure 2.11a), the scarcity of available liquid forces the formation of larger bubbles with limited liquid volume available per bubble. A plot of shear stress versus the

shear rate at the equilibrium bubble structure revealed that the foam viscosity increases with foam quality (Figure 2.11b).

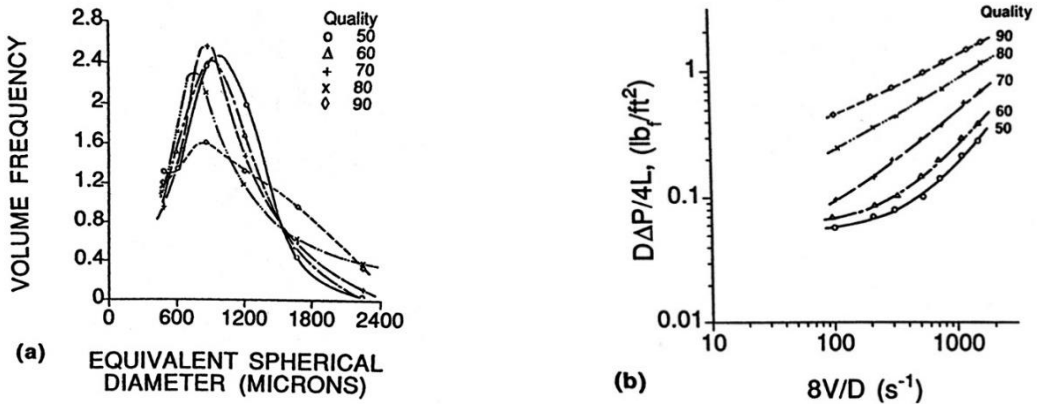

(a) Bubble size distribution for foam sheared at 1100 s^{-1}

(b) Shear Stress vs. Newtonian Shear Rate

Figure 2.11: Effect of foam quality (50% to 90%) on bubble structure and viscosity (Harris, 1989)

2.10.2 Base Liquid Type

Water, a mixture of 80% methanol and 20% water and kerosene base fluids were compared for shear degradation and bubble structure (Harris, 1989). Methanol mix based foam showed moderate degradation at high shear rates, while hydrocarbon-based foams were prone to degradation at high shear. Bubble sizes in oil-based foams were large; and therefore, they were more susceptible to shear breakdown (Figure 2.12). Moreover, preparing high-quality kerosene-based foams (70%) was difficult, since a uniform texture could not be generated at a low shear rate (500 s^{-1}); and high shear rate (1100 s^{-1}) led to the formation of gas slugs. The study indicated that due to thick lamellae of kerosene-based foam (as compared to water-based) and slow diffusion of polymeric surfactants through a hydrocarbon-based liquid, foam bubbles could not be stabilized, and gas slugs formed.

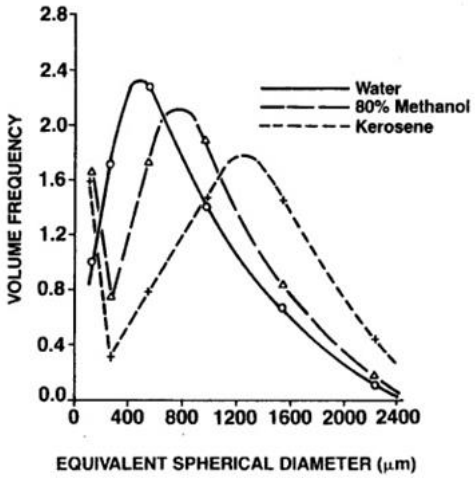

Figure 2.12: Liquid phase-type on 60% quality foams at 1100 s^{-1} (Harris, 1989)

2.10.3 Base Liquid Concentration

The addition of a gelling agent reduces the static drainage time and stabilizes foams. Referring to Figure 2.13a and 2.13b, at higher shear rates (1100 s^{-1}) addition of gelling agents affected the rheograms significantly but had little effect on bubble size distribution. At high shear rates, no change in bubble distribution is observed. However, at lower shear rates, viscous forces hinder the surface-stabilization process and modify the bubble distribution (Figure 2.13c). This alteration though is not reflected in the rheological behavior of the foams (Figure 2.13d).

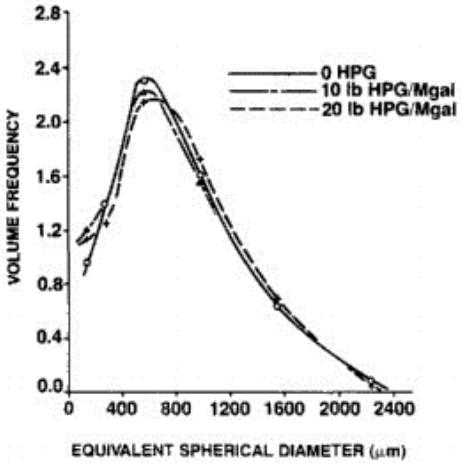

(a) Bubble size distribution - 1100 s^{-1}

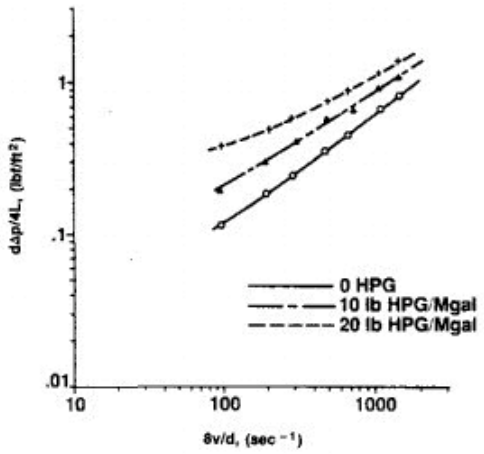

(b) Shear Stress vs. Newtonian Shear Rate - 1100 s^{-1}

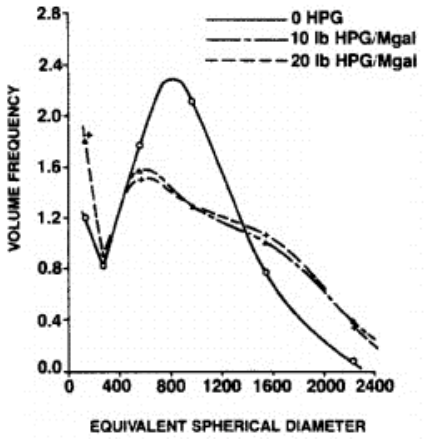

(c) Bubble size distribution - 250 s^{-1}

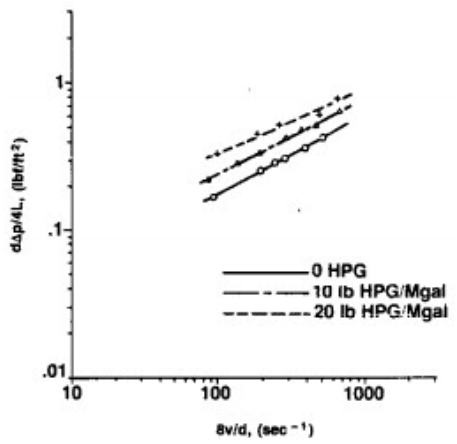

(d) Shear Stress vs. Newtonian Shear Rate - 250 s^{-1}

Figure 2.13: Effect of gelling-agent on 70% quality foams (Harris, 1989)

2.10.4 Surfactant Type and Concentration

The type of foaming agent used to stabilize foams, i.e. non-ionic, anionic, and amphoteric had little effect on foam rheology. Anionic surfactants produced slightly finer foam texture as compared to the other types of surfactants, which did not translate to higher viscosity (Figure 2.14).

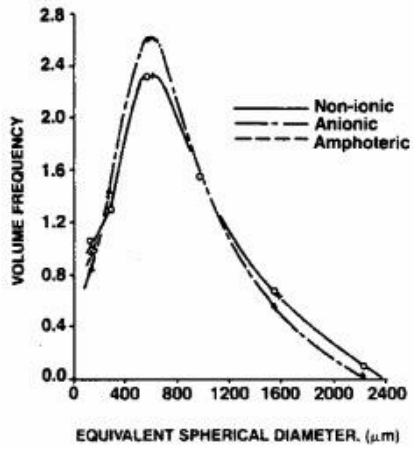

(a) Bubble size distribution

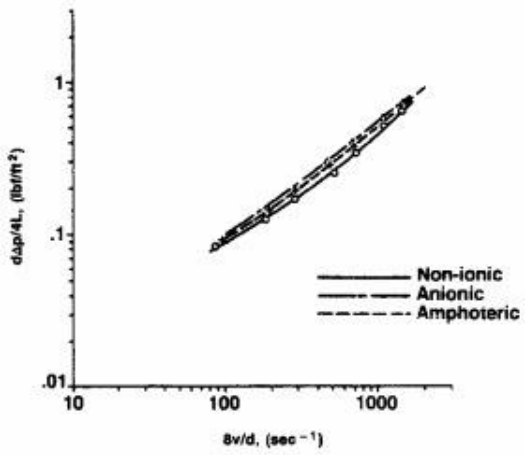

(b) Shear Rate vs. Newtonian Shear Stress

Figure 2.14: Effect of surfactant type on 70% quality foam at a shear of 1100 s^{-1} (Harris, 1989)

2.10.5 Foam Generation Technique

Harris (1989) used a 40/60 mesh sand to generate foam. A minimum differential pressure of 95 psi was required to generate uniform foam. The bubble size distribution appeared Gaussian and shifted towards lower diameter with increasing the differential pressure (Figure 2.15). Furthermore, the distributions were narrow, which indicated the development of uniform textured foam. However, bubble size distribution varied with the type of foam generation technique employed.

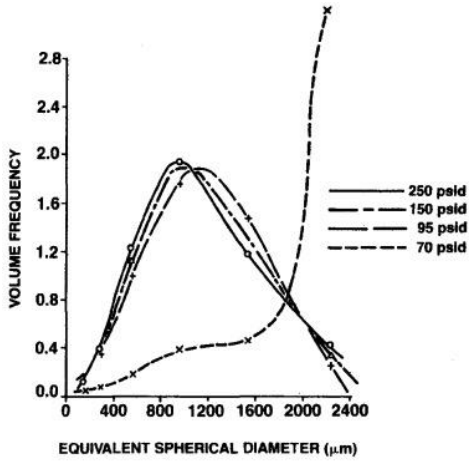

Figure 2.15: Effect of differential pressure across a foam generator (Harris, 1989)

2.10.6 Bubble Size Distribution

Different shear histories result in varying bubble size distribution with smaller sized bubbles forming at higher shear rates (Figure 2.16a). This change in bubble structure results in a two-fold increase in pressure reading and foam viscosity at low shear rates (less than 100 s^{-1}). However, at high shear rates (greater than 300 s^{-1}), a minimal effect of shear rate was observed on the measured viscosity values (Figure 2.16b)

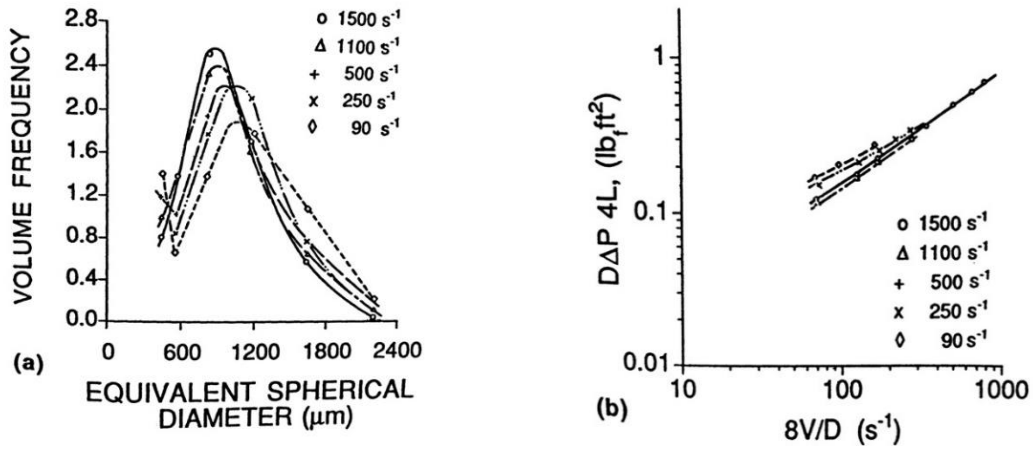

(a) Bubble size distribution **(b) Shear Rate vs. Newtonian Shear Stress**

Figure 2.16: Effect of shear rate (90 s^{-1} to 1500 s^{-1}) for 70% quality foam on bubble structure and viscosity, (Harris, 1989)

2.10.7 Pressure

At a given foam quality, only a minor change in bubble distribution was observed with pressure (600 to 1600 psi). However, at lower pressures, a larger shift in bubble sizes is observed (Figure 2.17a). At low system pressures, frictional drag in the tubing would create greater volumetric changes, because of higher gas compressibility at low pressures. Therefore, a 10 psi friction pressure change at 100 psi system pressure will have 10 times more expansion than a 10 psi change in a 1000 psi system. Foams generated at low pressures were more viscous than those generated at high pressures (Figure 2.17b). Approximately, constant system pressure across the test section is essential for accurate rheological measurements (Herzhaft 1999).

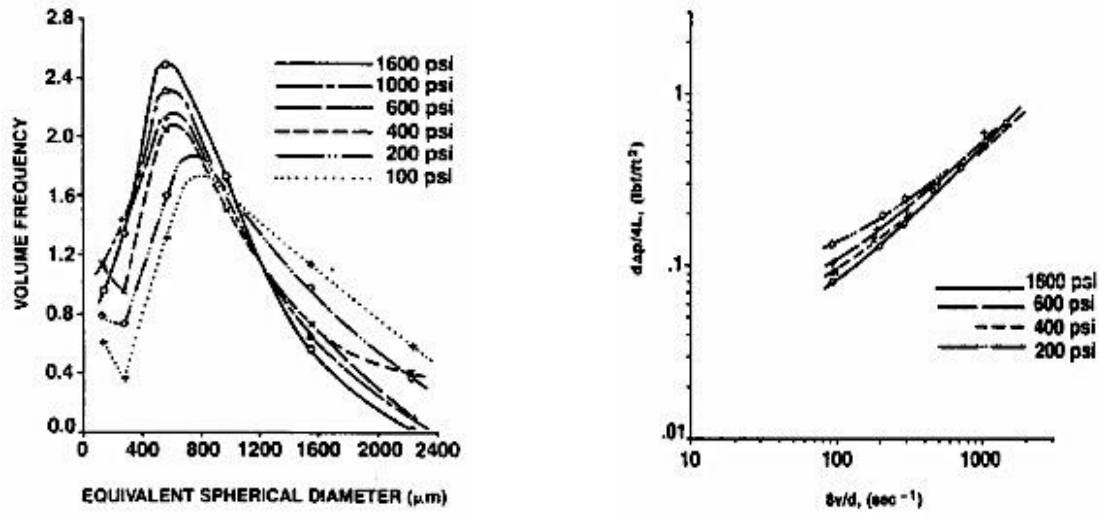

(a) Bubble size distribution **(b) Shear Stress vs. Newtonian Shear Rate**

Figure 2.17: Effect of pressure on 70% quality foams (Harris, 1989)

David and Marsden (1969) proposed foam compressibility model which relates foam compressibility to that of the gas phase. Thus:

$$c_F = -\left(\frac{1}{V_F}\frac{\partial V_F}{\partial p}\right)_T = \frac{V_G}{V_G+V_L}\left[-\frac{1}{V_G}\left(\frac{\partial V_G}{\partial p}\right)\right]_T = \Gamma c_G \qquad (2.35)$$

where, c_F = foam compressibility. $V_F = V_G + V_L$, is the foam volume or summation of liquid and gas volumes; p = pressure; T = Temperature; c_G = gas compressibility. The model shows that foam compressibility is not only a function of gas-phase properties but also depends on foam quality. Furthermore, as discussed earlier, the increase in pressure results in a finer texture (i.e. smaller bubble size). Fine-textured foam has greater specific surface energy due to the presence of a large film area. The finer texture translates into increased resistance to shear deformation. As a result, foams display higher shear stress readings at high pressures (Duan *et al.*, 2008).

There are conflicting findings on foam rheology variations with pressure. There still exists a lack of understanding of foam behavior in this regard and further investigations need to be performed. Cawiezel and Niles (1987b) conducted high-temperature (175°F) and high-pressure (34.47 MPa or 5000 psi) flow loop tests in a single pass foam viscometer and observed a significant

increase in low-shear rate viscosity with pressure. However, Harris (1989) observed a decrease in apparent viscosity with pressure. Recent studies (Akhtar, 2017; Lourenco *et al.*, 2004b) showed a limited effect of pressure on rheology.

2.10.8 Temperature

The viscosity of foam generally decreases with temperature (Akhtar, 2017; Bonilla and Shah, 2000; Gu and Mohanty, 2015b). This is related to the reduction in viscosity of the base fluid in case of stiff foams. Film thickness reduces with temperature and increases the rate of foam drainage and therefore affects its stability. Which also explains the difficulty of foam generation at elevated temperatures. Viscosity reduction is more significant in high-quality foams which is due to accelerated drainage from the foam films.

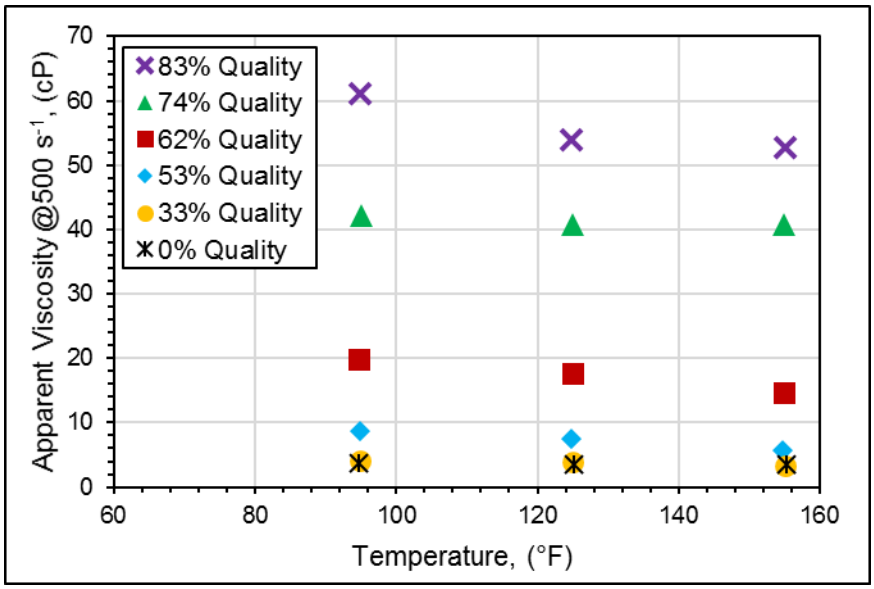

Figure 2.18: Reduction of the apparent viscosity of aqueous foams with temperature at 500 s^{-1} (Gu and Mohanty, 2015)

2.11 Modeling of Foam Flow Hydraulics

Foam provides an attractive alternative as a drilling fluid in underbalanced operations. Designing foam drilling jobs requires precise hydraulics modeling in order to determine

operational parameters such as optimum gas and liquid injection rate, back pressure requirement, etc. Theoretically, hydraulics modeling of both incompressible (drilling muds) and incompressible (foam fluids) are comparable, i.e., they both require the calculation of Reynolds number for determination of flow regime (laminar or turbulent). Earlier works by Raza and Marsden (1967) observed similar velocity profiles for compressible and incompressible in a pipe. For laminar flow, the friction pressure gradient is directly related to the velocity profile, while, in case of turbulent flow, friction factors are obtained as a function of Reynolds number. For calculation of annular pressure drop exact solutions like the Fredrickson and Bird (1958) for power-law fluid, can be used (Zamora and Lord, 1974).

However, due to foam's compressibility, its properties such as density, quality, apparent viscosity, and flow velocity changes along with the well profile. Therefore, for hydraulic calculations, segment-wise analysis is performed, and the density of foam is obtained at each segment using the equation of state for foam (Appendix III). Apparent viscosity is then calculated at the in-situ foam quality and shear rate. This approach was used by Blauer *et al.*, (1974), Okpobiri and Ikoku (1983), and Ozbayoglu (2002).

Some researchers observed the presence of a thin liquid layer close to the wall, which slipped without being sheared (Figure 2.19). The remaining contribution to flow was attributed to bulk foam shearing mechanism also termed as "flow due to fluidity" (Beyer *et al.*, 1972; David and Marsden, 1969; Peysson and Herzhaft, 2005). They have either used empirically determined slip velocity correlations or rheology definition for hydraulics modeling for hydraulics calculations. However, slip velocity correlations provide no connection to foam rheology and therefore are limited by their predictive capability (Ahmed *et al.*, 2003a).

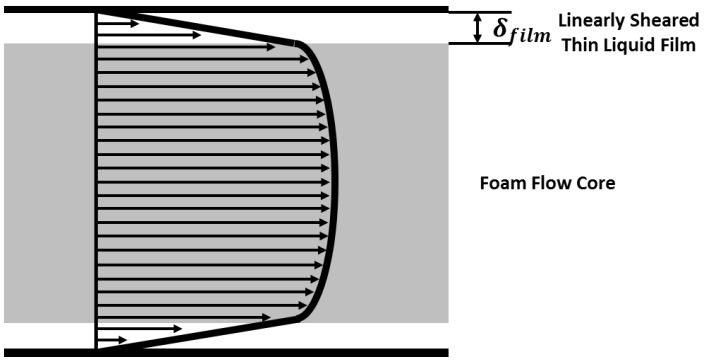

Figure 2.19: Velocity field in viscous foam flow with a pure liquid lubricated layer (Peysson and Herzhaft, 2005)

Valko and Economides (1992) introduced a new concept of "volume equalization" and developed rheological parameters independent of pressure and quality. Using this concept, a constant friction factor could be used for the entire pipe section for laminar and turbulent flow regimes. It should be noted that the change in pressure gradient along the flow path was attributed to changes in density and velocity. Other researchers (Capo *et al.*, 2006; Gardiner *et al.*, 1998; Lourenco *et al.*, 2004a) have used this principle along with a wall slip velocity for foam hydraulic modeling.

More recently, Gajbhiye (2011) introduced a technique that treated foam as a two-fluid system and characterized flow behavior-based visual observations of bubble texture and distribution and pressure response from experimental foam flow tests. Similar methodology was followed by other researchers (Edrisi *et al.*, 2014; Edrisi and Kam, 2014b, 2015; Gajbhiye and Kam, 2012), where they developed contour plots of pressure and viscosity superimposed on the gas-liquid superficial velocity cross plots using experimental data from horizontal and inclined foam flow experiments (Figure 2.20). These contour plots were analyzed mathematically, to generate empirical constitutive equations, which could be used to develop pressure contour maps for different initial conditions.

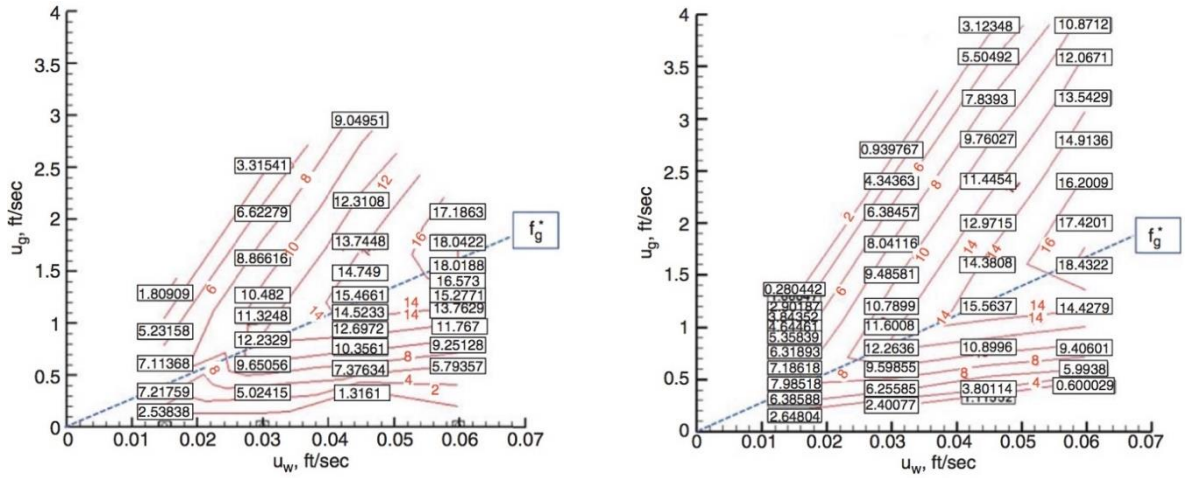

a) Pressure Contours: Experimental Data **b) Pressure Contours: Reconstructed**

Figure 2.20: Pressure drop contour reconstructed from Experimental Data (Edrisi and Kam, 2014a)

Blauer *et al.* (1974) used effective viscosity (μ_e) concept, which combines the plastic viscosity, μ_p, and foam yield strength, τ_Y, for calculation of Reynolds number and Fanning friction factor. Furthermore, the relation between Reynolds number and Fanning friction factor was identical for foam and single-phase fluid. Pressure drop was calculated for laminar flow in pipes using the Buckingham-Reiner equation for Bingham plastic fluids and is expressed as,

$$Q = \frac{\pi D^3 \tau_w g_c}{32\mu_p}\left[1 - \frac{4\tau_Y}{3\tau_w} + \frac{1}{3}\left(\frac{4\tau_Y}{3\tau_w}\right)^4\right] \tag{2.36}$$

where, $\tau_w = \Delta P.\, D/4L$

Sanghani (1982) and later Sanghani and Ikoku (1983) presented analysis similar to Blauer *et al.* (1974), with foams as pseudoplastic fluid. Effect of gas on foam density was incorporated, and experimental data were presented for the calculation of model parameters, n_F and K_F. For laminar flow the expression for calculation of friction pressure in pipes was developed and is given as:

$$\left(\frac{\Delta P}{\Delta L}\right)_f = \frac{4K_F}{D}\left[\frac{8(3n_F+1)Q}{\pi n_F D^3}\right]^{n_F} \tag{2.37}$$

Deshpande and Barigou (2000) conducted foam flow experiments in vertical pipes and studied the effects of, liquid-phase (polymer) type, surfactant type and concentration, foam generation technique, and pipe diameter on pressure drop, bubble structure and liquid holdup in foams. The authors assumed the power-law behavior of foam and neglected wall slip. They plotted Reynolds number and Fanning friction factor on a log-log scale for nearly 300 experimental data points and developed an explicit expression for friction factors for laminar foam flow in a vertical pipe (valid for $10^{-6} \leq Re \leq 10^{-1}$).

$$f = \frac{18.36}{Re^{0.97}} \quad (R^2 = 0.98) \tag{2.38}$$

where Reynolds number for a Power-law fluid was used in the calculation,

$$Re = \frac{\rho_F u_F^{2-n_F} D^{n_F}}{2^{n_F-3} K_F (3+1/n_F)^{n_F}} \tag{2.39}$$

Early mathematical expressions for slip velocity (u_{slip}) and velocity due to fluidity (u_{fluid}) were developed by David and Marsden (1969), expressed in terms of semi-compressibility. Mooney's expression for flow through a conduit of Newtonian fluid was used to determine the total flow:

$$Q = \frac{1}{c_G \Gamma}\left[\frac{\pi}{2}\frac{R^3}{L}\beta_{slip} - \frac{24\pi L^3}{P^4}\int_0^{\tau_a} u\tau^3 d\tau\right] \tag{2.40}$$

where, R = pipe radius; L = conduit length; $c_G\Gamma$ = foam semi-compressibility; β_{slip} = slip coefficient.

Beyer *et al.* (1972) developed empirical relations for slip velocity (u_{slip}) in terms of liquid volume fraction (LVF = $1-\Gamma$) and wall shear stress (τ_w). They also proposed that the total

velocity (u_{total}) was the summation of the slip velocity (u_{slip}) and fluidity component (u_{fluid}). The Bingham Plastic fluid definition was used to determine the fluidity component of the velocity for flow in pipe ($u_{fluid} = 144D\tau_w/8\mu_e\,[1 - 4\tau_Y/3\tau_w]$, $D =$ pipe diameter). The researchers developed an explicit function (Ψ) to determine the frictional pressure loss as a function of total velocity (u_{total}), Liquid volume fraction (LVF), and pipe diameter (D) and is given as,

$$\left(\frac{\Delta P}{\Delta L}\right)_f = \frac{4\tau_w}{D} = \Psi[u_{total}(T,P); LVF(T,P); D] \tag{2.41}$$

Kraynik (1982) observed that during the flow of aqueous foams in glass pipes, the foam itself moved as a "rigid plug" with minimal shearing, while, shearing was observed only in the thin film of water (thickness = δ_{film}) present at the pipe wall. The authors presented an expression for foam flow rate in terms of pressure drop and is given as:

$$Q_F = \frac{\pi R^3 \delta_{film}}{2\mu_{water}}\left(\frac{\Delta P}{\Delta L}\right)_f \tag{2.42}$$

where, μ_{water} = water viscosity; $R =$ pipe radius; $L =$ pipe length.

Peysson and Herzhaft (2005) observed similar findings as Kraynik (1982) and presented a two-phase hydraulic model for foam flow that consists of a "lubrication film layer" consisting of pure liquid and a bulk core region where foam moves almost like a plug with marginal shear. The liquid film layer displayed a Newtonian behavior whose thickness was a function of the bubble to wall interactions and independent of the tube diameter. The pressure drop for the flow of film on the wall and foam core was expressed below:

$$\left(\frac{\Delta P}{\Delta L}\right)_{total} = \frac{Q_{total}}{\frac{\pi}{8}\left[\frac{R^4}{\mu_L} + (R_{core})^4\left(\frac{1}{\mu_F} - \frac{1}{\mu_L}\right)\right]} \tag{2.43}$$

where, $R_{core} = R - \delta_{film}$ = Core foam size; δ_{film} = film layer thickness; μ_F, μ_L = foam and liquid viscosity; Q_{total} = total flow rate.

Chen *et al.* (2005a) developed empirical relations for the slip coefficient for isothermal foam flow in the annulus for prediction of friction pressure loss. The authors assumed a power-law fluid behavior and assumed negligible change in fluid properties with pressure and temperature. The volumetric flow rate in the annulus for laminar flow was given by:

$$Q_{total} = \pi \cdot \left(\frac{n}{3n+1}\right) \cdot \left(\frac{D_{eq}}{2}\right)^{\frac{3n+1}{n}} \cdot \left(\frac{1}{2K} \cdot \left[\frac{\Delta P}{\Delta L}\right]_{total}\right)^{\frac{1}{n}} \tag{2.44}$$

where, $D_{eq} = \chi^{\frac{n}{3n+1}}.D_o$ = equivalent pipe diameter that causes same pressure loss in a pipe as measured in the annulus for given volumetric rate, Q; the function χ is given as:

$$\chi = (1-\xi^2)^{1+\frac{1}{n}} - \kappa^{1-\frac{1}{n}}(\xi^2 - \kappa^2)^{1+\frac{1}{n}} \tag{2.45}$$

where $\kappa = D_i/D_0$ and ξ = represents the ratio for the location of maximum velocity in the annulus and was correlated to κ and n as, $\xi = 0.9904.\kappa^{0.4141}.n^{0.01238}$.

Valko and Economides (1992) developed the technique of "volume equalization", for analyzing standard constitutive equations in terms of the parameter "specific volume expansion ratio" ($\varepsilon = \rho_L/\rho_F$), instead of foam quality. The researchers defined the Volume-Equalized Reynolds number ($Re_{VE} = D^n u^{2-n}\rho_F/K\varepsilon^{1-n}$) and Friction factor ($f = 2/Re_{VE} \cdot (6n+2/n)^n$) and proposed their invariance for pressure loss calculations during isothermal foam flow in a pipe. Furthermore, by performing mechanical energy balance, the authors derived an expression for frictional pressure loss calculation for a steady, isothermal flow of compressible fluids in horizontal pipes:

$$\left(\frac{\Delta P}{\Delta L}\right)_f = -\frac{1}{D}\frac{\left(2f_f b^2c^2 - Dg\right)p^3 + 4f_f abc^2p^2 + 2f_f a^2c^2p}{bp^3 + ap^2 - abc^2p - a^2c^2} \tag{2.46}$$

where, constants a, b, and c are given as,

$a = w_G \frac{RT}{M_G}$, $b = w_G \frac{RTB}{M_G} + (1 - w_G)\frac{1}{\rho_G}$, $c = \frac{4(m_G + m_L)}{\pi D^2}$, and $w_g = \frac{m_G}{(m_G + m_L)}$.

Gardiner *et al.* (1998) used Volume Equalization Principle and accounted for wall slip during the calculation of frictional pressure drop of foam flow in pipes. The authors derived a volume equivalized Hagen-Poiseuille's equation for a power-law fluid in order to calculate pressure drop over short distances. Later Lourenco *et al.* (2004) used the same hydraulic model and studied the effects of elevated pressure and elevated temperature on the foam hydraulics. The analogous Hagen-Poiseuille's equation is presented below,

$$Q_{total} = 2\pi \int_0^R ur.dr = \pi R^2 \left\{ u_{slip} + \frac{n}{n+1}\left[\left(-\frac{dp}{dL}\right)\frac{R^{n+1}\varepsilon^{n-1}}{2K}\right]^{\frac{1}{n}}\left[1 - \left(\frac{r}{R}\right)^{\frac{n+1}{n}}\right]\right\} \tag{2.47}$$

Some researchers (Princen, 1983; Prud'Homme, 1981) performed a theoretical analysis of an idealized two-dimensional hexagonal pencil stack model of a monodisperse foam to determine the threshold pressure drop required for foam to flow. They concluded that finer foams were "stiffer" and more resistant to deformation, furthermore, threshold pressure was a strong function of liquid volume fraction, since, dry foams create thinner water films.

$$\left(\frac{\Delta P}{L}\right)_Y = \frac{\alpha\sigma}{r_{cell}R} \tag{2.48}$$

where, α = dimensionless coefficient of the order of unity and its value is strongly dependent on the liquid volume fraction; σ = interfacial tension; r_{cell} = cell radius; R = tube radius; L = tube length.

Chapter 3

Theoretical Background

3.1 Rheological Models

In general, drilling fluids are categorized as Newtonian or non-Newtonian depending on the nature of the relationship between shear stress and shear rate. Fluids which show a linear relation are called Newtonian while the rest are classified as non-Newtonian fluids. A non-Newtonian fluid can be either shear-thinning (pseudoplastic) or shear-thickening (dilatant). Non-Newtonian fluids are further subcategorized based on the presence or the absence of yield stress. The flow curves for all fluids is shown in Figure 3.1, while, the general expressions for shear stress and shear strain relation is provided in Eq. (3.1).

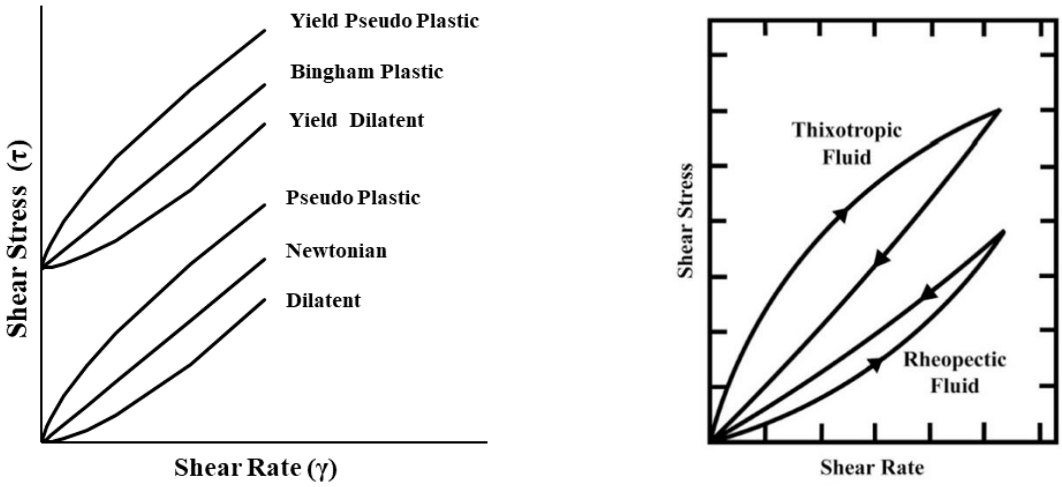

a) Time independent fluids **b) Time-dependent fluids**

Figure 3.1: Shear Stress versus Shear Rate for different fluids

Additionally, some fluids can be time-dependent, i.e., they do not re-trace their shearing history on the removal of shearing force, resulting in a hysteresis loop in the shear stress versus shear rate flow curve (Figure 3.1b). Time-dependent fluids can either show a decrease in apparent

viscosity over time (thixotropic) or an increase in apparent viscosity with time (rheopectic). A generalized rheological model for all time-independent fluids can be written as:

$$\tau = A(C + \dot{\gamma})^B \tag{3.1}$$

where, τ = shear stress; $\dot{\gamma}$ = shear rate; A, B, C = model parameters are listed in Table -3-1.

Table -3-1: Model parametric constants *A*, *B*, and *C*

Rheology Models	*A*	*B*	*C*
Newtonian	μ	1	0
Bingham	μ_p	1	τ_Y/μ_p
Pseudo-plastic	K	n < 1	0
Dilatant		n > 1	
Yield pseudo-plastic	K	n < 1	τ_Y/K
Yield dilatant		n > 1	

where μ is Newtonian viscosity; $\mu_p$is plastic viscosity; K is fluid consistency index; n is flow behavior index; τ_Y is yield stress.

3.2 Rheometry

A thorough understanding of fluid rheology is crucial during field operations, for estimating pump requirements, tubular sizing, cuttings lift capacity. The frictional pressure drop is a function of the viscous properties of the fluid. Viscous forces dominate during laminar flow, while, inertial forces are more prevalent during turbulent flow.

During rheometric measurements, the following major assumptions are made: i) the fluid is treated as a "continuum", ii) fluid composition is considered homogenous, and iii) fluid properties are considered "isotropic" or "direction independent". These assumptions are valid for both low molecular weight fluids (molecular dimensions 10^{-8} - 10^{-7} cm) and high concentration polymer solutions (macromolecule size 10^{-5} cm). On the other hand, emulsions, suspensions, and

foams can be treated as “pseudo-single-phase liquid” and expressed by average properties as long as their uniform phase distribution is not altered while flowing. Additionally, rheological measurements for foams have to minimize complications resulting from gas compressibility (Heller and Kuntamukkula, 1987; Akhtar et al., 2018). Two types of rheometers (rotational and pipe viscometers) were used in the present study.

3.2.1 Rotational Viscometer

Rotational viscometers were used to measure base fluid rheological properties. In general, Rotational viscometers measurements are performed in either controlled stress (shear is imposed, and strain is measured) or controlled strain mode (shear stress measured for imposed strain). Controlled strain viscometers are more common and useful for low viscosity fluids. Conversely, controlled stress provides is more versatile and is especially useful for fluids with internal structure and particle to particle interaction. Besides, it provides direct control over fluid-induced shear stress which is useful for measuring yield stresses. Major assumptions in using rotational devices include steady-state laminar flow, isothermal conditions, and negligible gravity and end effects. The three major rotational viscometer geometries are “Couette”, “parallel plate”, and “cone and plate” as shown in Figure 3.2.

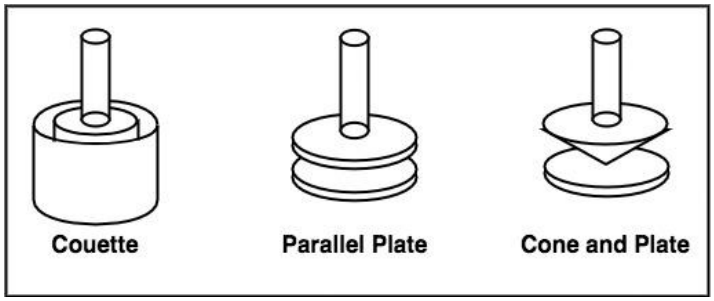

Figure 3.2: Couette, Parallel Plate, and Cone and Plate geometries for measuring fluid viscosity.

The most common type of rotational viscometers uses a "concentric cylinder with a rotating sleeve" or the "Couette", geometry. The test fluid sample is placed between the sleeve and the suspended bob. The sleeve rotates with an angular velocity, Ω, and shears the fluid sample, which induces a torque on the surface of the bob. The torsion spring enforces a counter torque to equalize the torque by the fluid momentum and is a product of the torsion constant, k_{T} and the angle of deflection, θ_{bob}. Wall shear stress is calculated from this counter torque and the wall shear rate is obtained from the angular velocity Figure 3.3b shows the components of a Couette type rotational viscometer.

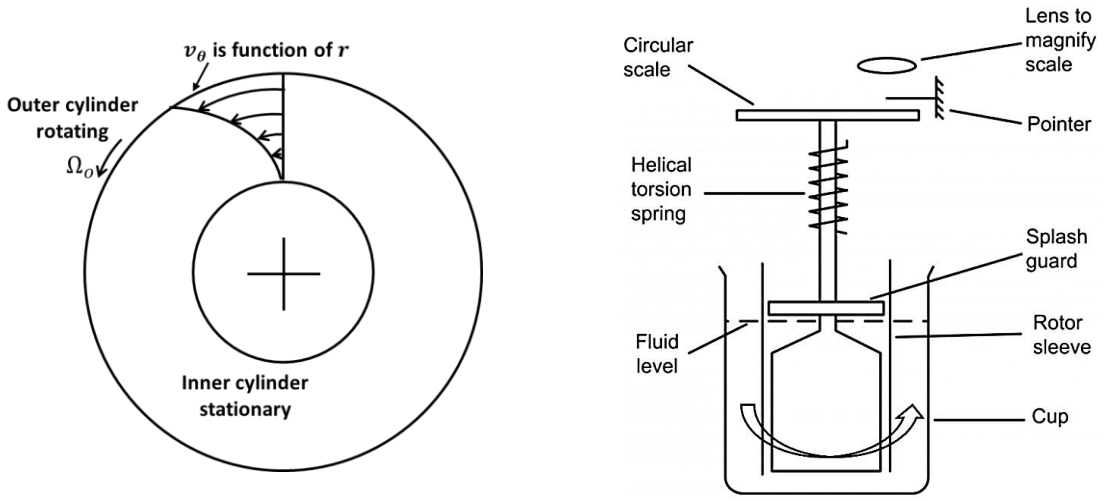

(a) Velocity Profile **(b) Components of Couette Viscometer**

Figure 3.3: Velocity profile and components in a Couette geometry rotational viscometer (Lam and Jefferis, 2014)

The measurements using rotation viscometer must be performed after ensuring that the flow between the coaxial cylinders is steady, laminar, and tangential. The torque, T, experienced by the bob of a Couette rotational viscometer, can be converted to the wall shear stress using Eq. (3.2),

$$\tau_{bob} = \frac{T}{2\pi\, {R_{bob}}^2 H_{bob}} \tag{3.2}$$

where, R_{bob} is cup and bob radius; T is torque measured at bob; H_b is the height of bob.

The torque is related to the angular displacement of the torsion spring, θ_{bob},

$$T = k_T \theta_{bob} \tag{3.3}$$

For a narrow gap viscometer, the shear rate is calculated from Eq. (3.4). These two expressions are then used to develop the fluid flow curve and calculate the viscosity.

$$\dot{\gamma} = \frac{\Omega R_{bob}}{\left(R_{cup} - R_{bob}\right)} \tag{3.4}$$

Rotational viscometers, however, have limitations with regards to estimating foam rheology (Heller and Kuntamukkula, 1987): i) bubble collapse and network rearrangement in small sample volume, causes discontinuous measurements, ii) foam drainage during measurements forms liquid layer at bottom, which affects data reproducibility, iii) non-uniform shearing of high-quality foams during yield stress measurements due to segregation. To mitigate these concerns, some studies (Chen *et al.*, 2005b; Washington, 2004) have used inline rotational viscometers, with roughened surfaces and fins on the spindle to minimize liquid drainage and wall slip. However, the data treatment is complex for such rheometers.

3.2.2 Pipe Viscometer

The basic principle of pipe viscometry involves pumping test fluid through a conduit of standard dimensions under isothermal condition, and measuring the pressure drop and volumetric flow rate in the laminar flow regime for a fully developed, steady-state flow. Thereafter, the relationship between nominal Newtonian wall shear rate (calculated from flow rate) with wall shear stress (obtained from pressure drop) is established to provide information about the fluid rheology. Pipe viscometers are more reliable and accurate than annular viscometers for measuring foam rheology as the slot flow approximation is not required. Since measurements are performed in a fully developed flow, entry and exit lengths must be sufficiently long before the fluid enters

the test section (Figure 3.4). However, pipe viscometers are relatively expensive, and not convenient for field applications; therefore, they are mostly used for research purposes and during in-line viscometric measurements.

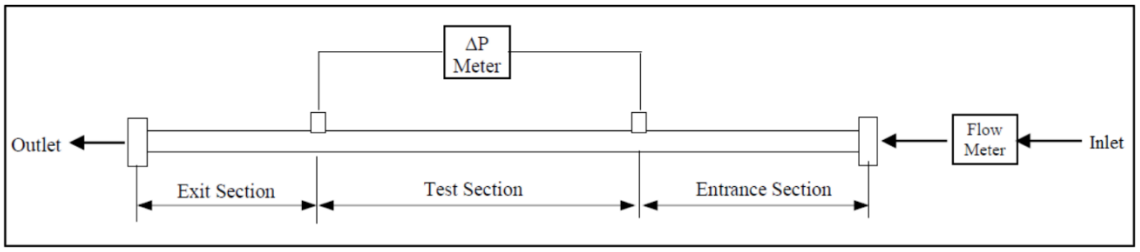

Figure 3.4: Typical pipe viscometer setup (Ahmed and Miska, 2009)

For a fully developed laminar flow through a pipe segment of length ΔL, and diameter D, integration of the velocity distribution over the entire pipe section (Figure 3.5) provides the volumetric flow rate of the fluid.

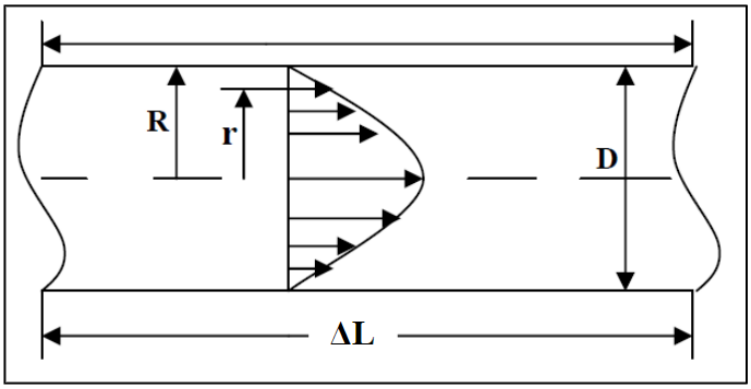

Figure 3.5: Fluid flow in pipe segment (Ahmed and Miska, 2009)

$$Q = 2\pi \int_0^R u(r)\, dr \tag{3.5}$$

where, $u(r)$ is axial velocity. Integrating Eq. (3.5) by parts and on applying boundary conditions ($u(R) = 0$), following expression is obtained for the volumetric flow rate,

$$\frac{Q}{\pi R^3} = -\pi \int_0^R r^2 \frac{du}{dr} dr \tag{3.6}$$

For steady, incompressible fluid flow in a pipe, the momentum balance at radius R, over length ΔL, provides an expression for wall shear stress.

$$\tau_w = \frac{R\Delta P}{2\Delta L} \tag{3.7}$$

Similarly, shear stress at distance, r, from the pipe center, is given as:

$$\tau(r) = \frac{r\Delta P}{2\Delta L} \tag{3.8}$$

Combining Eqs. (3.7) and (3.8),

$$\frac{\tau(r)}{r} = \frac{\tau_w}{R} \tag{3.9}$$

Changing the variables in Eq. (3.12),

$$r = \frac{\tau(r)}{\tau_w} R \rightarrow dr = \frac{R}{\tau_w} d\big(\tau(r)\big) \tag{3.10}$$

On substituting the variables in Eq. (3.12),

$$Q = -\pi \int_0^{\tau_w} \left(\frac{\tau(r)}{\tau_w} R\right)^2 \frac{du}{dr} \frac{R}{\tau_w} d\big(\tau(r)\big) \tag{3.11}$$

On rearranging,

$$\frac{Q}{\pi R^3} = \frac{1}{(\tau_w)^3} \int_0^{\tau_w} \tau^2 \, f(\tau) \, d\tau \tag{3.12}$$

where, $f(\tau) = -du/dr =$ shear rate.

Multiplying both sides by $(\tau_w)^3$ and differentiating using Leibnitz integral rule,

$$\frac{3{\tau_w}^2 Q}{\pi R^3} + \frac{{\tau_w}^3}{\pi R^3} \frac{dQ}{d\tau_w} = {\tau_w}^2 f(\tau_w) \tag{3.13}$$

Upon rearranging the above equation:

$$f(\tau_w) = \frac{3Q}{\pi R^3} + \frac{\tau_w}{\pi R^3}\frac{dQ}{d\tau_w} \tag{3.14}$$

Converting volumetric flow rate to average flow velocity through the cross-section, Robinowitch-Mooney expression for the generalized wall shear rate for pipe flow is obtained:

$$\dot{\gamma}_w = -\left(\frac{du}{dr}\right)_{\tau_w} = \frac{3}{4}\left(\frac{8U}{D}\right) + \frac{\tau_w}{4}\frac{d(8U/D)}{d\tau_w} \tag{3.15}$$

or,

$$\dot{\gamma_w} = \frac{1}{4}\left(\frac{3N+1}{N}\right)\frac{8U}{D} \tag{3.16}$$

N is the flow behavior index determined from the slope of log-log plot wall shear stress versus the nominal Newtonian wall shear rate $(8U/D)$. Thus

$$N = d\tau_w/d(8U/D) \tag{3.17a}$$

Also, the generalized fluid consistency index is obtained from the log-log plot as shown in Fig. 3.6. Thus:

$$\tau_w = k'\left(\frac{8U}{D}\right)^N \tag{3.18b}$$

where, k' is the generalized fluid consistency index.

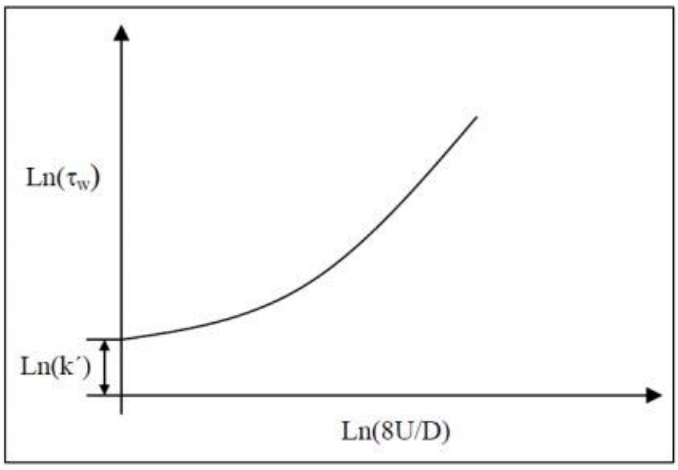

Figure 3.6: Generalized plot of logarithmic wall shear stress versus logarithmic nominal Newtonian shear rate (Ahmed and Miska, 2009)

When foam behaves like a power-law fluid, then the curve is a straight line and the equation reduces to,

$$\tau_w = K\dot{\gamma_w}^n = K\left[\left(\frac{3N+1}{N}\right)\frac{8U}{D}\right]^n \tag{3.19}$$

Equation (3.19) is valid for laminar flow, which is validated using the Reynolds number. The equation for Reynolds number in terms of mean fluid velocity and wall shear stress can be written as:

$$Re = \frac{8\rho U^2}{\tau_w} \tag{3.20}$$

For power-law fluids, $d\tau_w/d(8U/D) = n$ and Eqs. (3.19) and (3.20) can be combined to obtain the expression of generalized Reynolds number for power-law fluids.

$$Re = \frac{8\rho U^2}{K\left[\left(\frac{3n+1}{n}\right)\frac{8U}{D}\right]^n} = \frac{\rho U^{2-n} D^n}{8^{n-1}.\ K\left[\left(\frac{3n+1}{n}\right)\right]^n} \tag{3.21}$$

The Fanning friction factor in terms of wall shear stress is written as:

$$f = \frac{\tau_w}{0.5\rho U^2} \tag{3.22}$$

When the Reynolds number is less than "2100", the flow is considered laminar. Flow transition to turbulent flow occurs at high Reynolds numbers. Turbulent flow is characterized by fluctuating velocity and pressure fields and increased hydraulic resistance. To obtain accurate friction pressure drop in turbulent conditions, empirical correlations based on the Fanning friction factor and Reynolds number are used. For laminar flow, the Fanning friction factor is derived from Hagen-Poiseuille's law for pipe flow and is expressed as:

$$f = \frac{16}{Re} \tag{3.23}$$

For turbulent flow, Dodge and Metzner, (1959) proposed an implicit empirical equation to predict Fanning friction factor:

$$\frac{1}{f^{0.5}} = \frac{4}{n^{0.75}} lo\, g \left[Re.f^{\left(1-\frac{n}{2}\right)}\right] - \frac{4}{n^{1.2}} \tag{3.24}$$

where n is fluid behavior index.

3.2.3 Considerations while Conducting Rheological Measurements

There are certain requirements that need to be fulfilled while conducting rheological measurements of foam using different viscometers. These requirements are as follows:

- *Bubble to Gap Size Effects*: As a rule of thumb, for accurate viscosity measurements, the bubble size should be less than 1/20th of the diameter of a pipe viscometer or the annular gap of a rotational/Couette viscometer. The average bubble size in most foam systems is in the range of 50 to 150 μm (Govindu *et al.*, 2019; Sherif *et al.*, 2015a, 2015b), consequently, the gap required in a Couette viscometer or diameter needed in a pipe viscometer would be of the order of 3 mm or larger. This implies that only foam with very fine texture can be tested in standard viscometers (Heller and Kuntamukkula, 1987).
- *Slip and Yield Stress Effects*: The stress distribution in most viscometers is not uniform. Therefore, for high-quality foams, regions of no-flow can exist, when stress is less than the yield value. In such cases, foam deforms elastically and may start slipping at the boundaries when a lubricating liquid film forms due to gravity drainage and bubble coalescence. As a result, the viscometer records reduced yield stress values.
- *Effects of Bubble Size and Drainage:* Some models relate foam structure to their rheology, Structural models (i.e. models which account for the foam structure) for viscosity prediction,

propose an inverse relationship between yield stress and bubble size. The process of coarsening by gas diffusion results in an increase in the mean bubble size over time. Moreover, standing foams drain over time, resulting in foam quality variations (i.e. increase at the top and reduction at the bottom) in a vertical viscometer. This causes a vertical variation of both viscosity and yield stress. To mitigate this effect, either the residence time should be decreased or a flow-through rotational viscometer should be used. Another possibility is to use a pipe viscometer; however, pressure and temperature changes occurring across the viscometer must be minimized.

3.3 Determination of Foam Density

Foam density measurements are generally gathered while running flow experiments. For a given pressure and temperature conditions, foam density (ρ_F) can be calculated as follows:

$$\rho_F = \rho_G(\Gamma) + \rho_L(1-\Gamma) \tag{3.25}$$

where, ρ_G is gas density; ρ_l is liquid density. Rearranging the terms in Eq. (3.25) yields:

$$\Gamma = \frac{\rho_L - \rho_F}{\rho_L - \rho_G} \tag{3.26}$$

Assuming a compressible gas and neglecting the gas solubility in the liquid phase, the density of gas can be obtained using the real gas equation from standard conditions of temperature and pressure:

$$\rho_G = \frac{Z_{sc}P.T_{sc}}{ZP_{sc}.T} \cdot \rho_{G_{sc}} \tag{3.27}$$

where, P, T, and Z are test pressure, temperature, and compressibility factors, respectively. P_{sc}, T_{sc}, are standard temperature and pressure; $\rho_{G_{sc}}$and Z_{sc} are the density and compressibility of gas at standard conditions.

Chapter 4

Experimental Studies

PAC polymer-based foams were tested to examine the effect of temperature on the rheology, at a constant pressure of 6.9 MPa. The physical properties of chemicals used for the study are discussed in the first part of this chapter. This is followed by a detailed description of the experimental setup, the test procedure, and the test matrix used for the experimental investigation. Finally, the results of the pipe viscometer calibration test with a Newtonian fluid and degradation studies for the PAC polymer are discussed.

4.1 Chemical Requirements for Test Fluid Preparation

Stiff foams are a dispersion of gases in a polymer-based liquid solution which is stabilized by the help of surfactants. For the present study, a mixture of poly-anionic cellulose (PAC) polymer and surfactant were used to prepare the foaming solution for rheology characterization tests and performing dynamic measurements of yield stress in high-quality foams.

4.1.1 Polymer Sample

Poly Anionic Cellulose (PAC) available in the market under the commercial name POLYPAC-R was used to create polymer-based foams. It is available in powdered form and water-soluble. Often this polymer is used in the field to control fluid loss properties as well as the viscosity of aqueous solutions. PAC has good resistance to bacterial attacks, and it is environmentally friendly. Properties of POLYPAC-R are presented in Table 4-1. The polymer was mixed with tap water to prepare the base liquid.

Table 4-1: Physical properties of POLYPAC-R

Attribute	Behavior
Color	White
Specific gravity	1.5-1.6
pH in 1% aqueous solution	6.5-8
Temperature stability	149 °C (300 °F)

4.1.2 Foaming Agent

An anionic surfactant (foaming agent) sold under the commercial name, Howco Suds™ was used as the surfactant for stabilizing the foams. The concentration of the surfactant in the base liquid was 2% by volume. The properties of the surfactant are listed in Table 4-2.

Table 4-2: Physical properties of Howco-Suds™

Attribute	Behavior
Color and Physical State	Light yellow liquid
Boiling Point	>300 °F
pH	6.5-7.5

4.1.3 Inert Gas

Nitrogen gas stored in pressurized cylinders was used as the phase to generate foam. A pressure regulating valve at the discharge end of the cylinder was utilized to control the pressure and the rate of gas supply at the point of injection.

4.2 Experimental Apparatus

Rheological measurements for the base liquid were performed using a rotational viscometer while pipe viscometer provides the rheological characterization of foam. The two experimental apparatuses are discussed in the following sections.

4.2.1 OFITE Model 900 Rotational Viscometer

Automated rotational viscometer (OFITE Model 900 viscometer) with a coaxial cylinder geometry (Figure 4.1), is used to measure the rheology of the base liquid. The viscometer uses "R1B1" configuration for rotor and bob with a spring constant of "1", that measures viscosities for very low to intermediate shear rates (0.01- 1700 s^{-1}). The sample cup is heated using a heating cup, to a maximum of 190°F. The rheometer can be operated manually, with digital readouts for the measurements, or remotely using the ORCADA™ software package, which allows the design of customized tests. Table 4-3 lists the equipment specifications.

Figure 4.1: OFITE Model 900 Rotational Viscometer

Table 4-3: Specifications of OFITE Model 900 Viscometer

Instrument	Geometry	Dimensions, mm	Shear Rate Range (s^{-1})
OFITE Model viscometer	Diameter of Bob	D_{bob} = 34.49	0.01-1700
	Diameter of Cup	D_{cup} = 36.83	
	Ratio (β)	D_{bob}/ D_{cup} = 0.9365	

4.2.2 Experimental Flow Loop

The experimental flow loop used to carry out the foam rheology tests (Figure 4.2) is divided into four sections: i) fluid (gas and liquid) injection and circulation, ii) heat exchanger, iii) foam generation, and iv) test sections. The entire setup is covered with polyurethane foam insulation, to minimize heat loss. Figure 4.3 shows the process flow diagram for the entire setup.

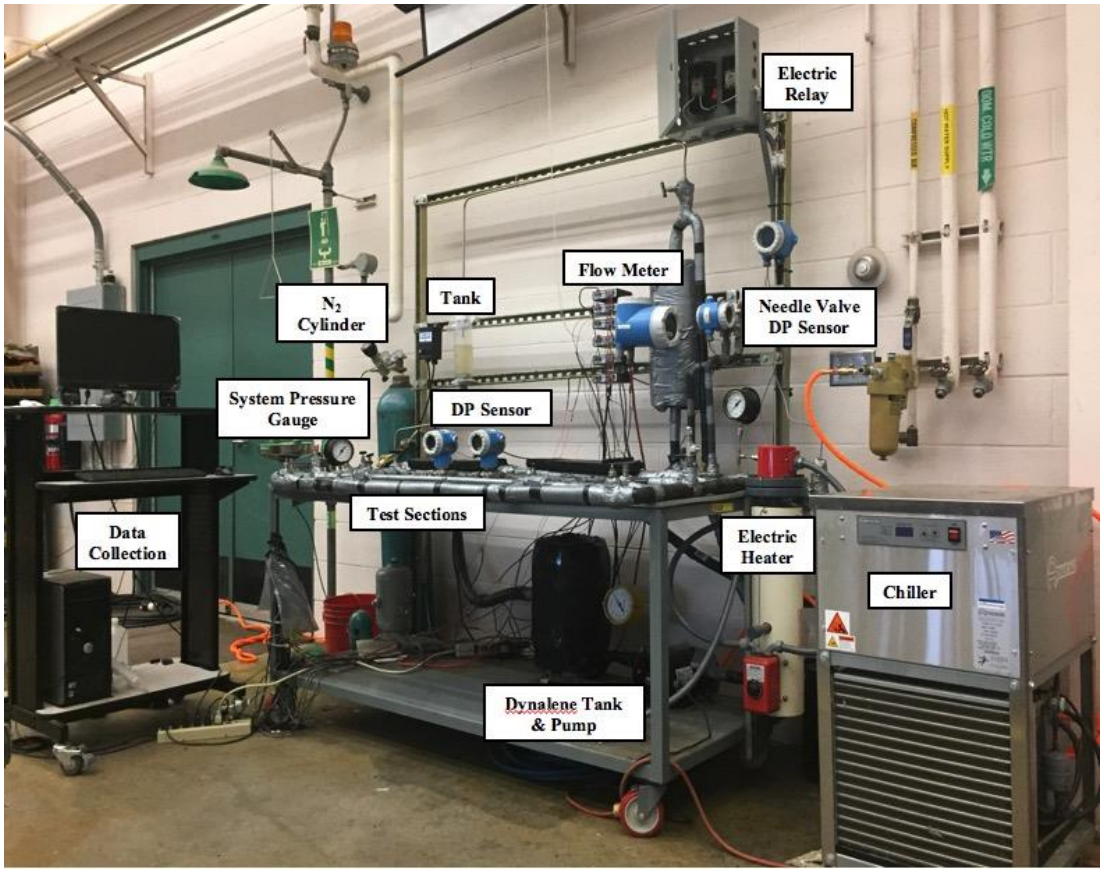

Figure 4.2: Foam Flow Loop Experimental Setup

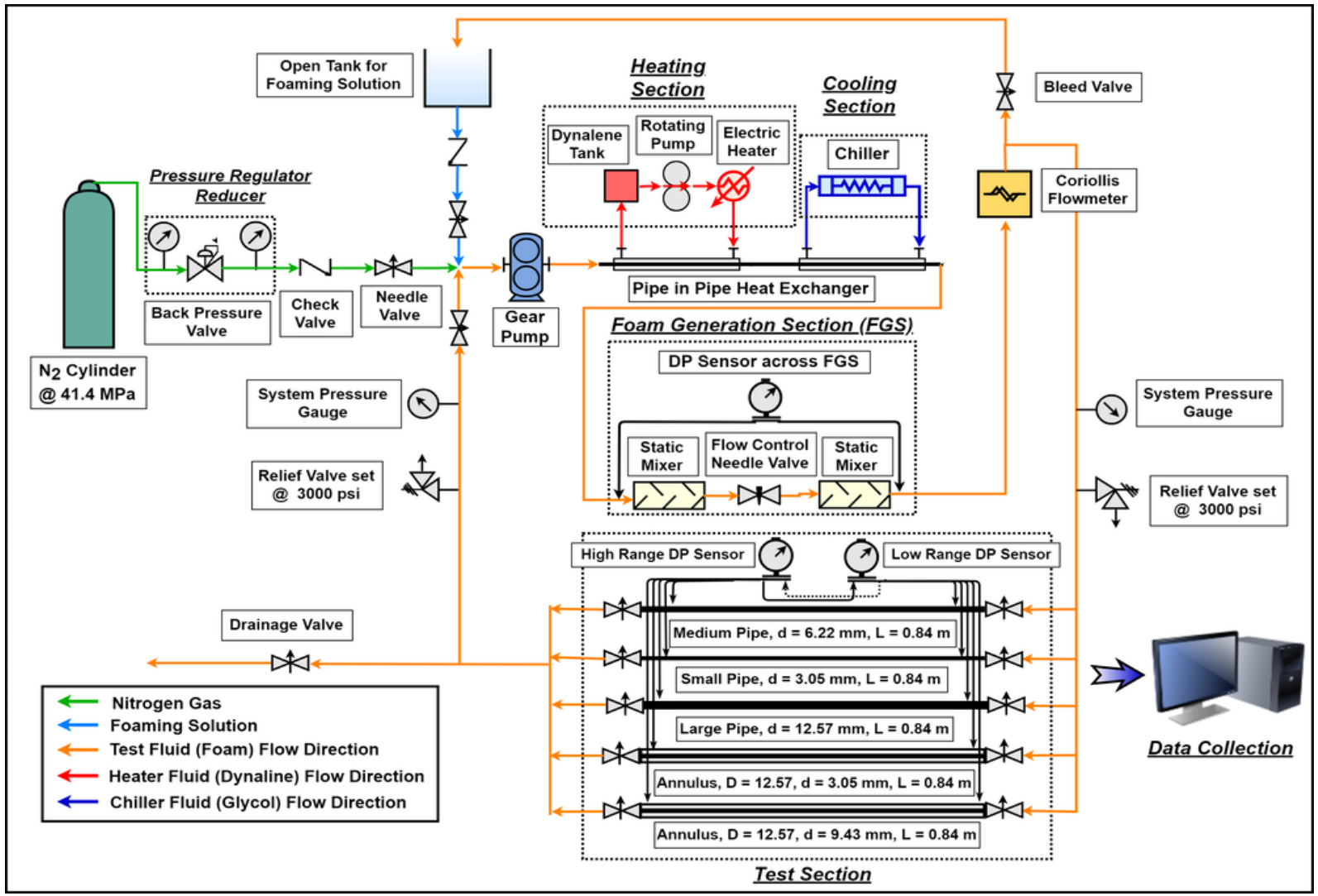

Figure 4.3: **Process flow diagram of Experimental Setup**

Fluid Injection and Circulation Section

The foaming fluid (base liquid) is introduced into the flow loop from a 1000-ml tank (base liquid tank), which is open to the atmosphere. Check valves (rated to 6000 psi), and bonnet needle valves, placed downstream of the tank prevent backflow, and isolate the tank when the required amount of fluid is introduced into the loop. The base liquid is topped up, as per requirement. A variable speed gear pump (Micropump GA-T23) rated for 115 AC/DC, capable of handling the multiphase flow and delivering a maximum flow rate of 1.14 L/min is used to inject base liquid into the loop and circulate test fluid. Needle valves are also used for bleeding surplus gas and liquid from the system while setting up quality. Nitrogen is introduced in the loop from a pressurized cylinder (rated at 6000 psi), through a pressure regulator. Analog gauges provide pressure readings at the point of introduction, while, check valves prevent the backflow of test fluid into the airline. Stainless steel tubes which are rated to 5000 psi are used for delivering pressurized fluids.

Heat Exchanger Section

The heat exchange section consists of double-pipe heat exchangers (heater and cooler) for heating and cooling test fluid. The test fluid is circulated in the opposite direction to the heat transfer fluid to maximize the energy transfer. In the heater, the test fluid is heated by circulating the heating medium (high-temperature heat transfer fluid, Dynalene) using a high-temperature rotary pump capable of handling a maximum temperature of 450°F. A 2.5-KW electric heater (Chromalox heater rated for maximum oil temp 500°F) is used to heat the heating medium. Heater setpoint temperature is controlled using a VBA program. To prevent viscous heating of test fluid during ambient temperature tests, a small-size industrial chiller (Advantage, #138881) is used that can pump ethylene glycol as a cooling fluid. The operating temperature range for ethylene glycol is 8-387°F.

Foam Generation Section

The foam generation section provides a high degree of foam homogeneity and repeatability of the rheology tests. The components of the foam generation section are, i) a needle valve that throttles the fluid flow and provides the mixing energy the foam generation requires through pressure drop, ii) static mixers that are placed both upstream and downstream of the needle valve, which provides required mixing, which homogenizes the test fluid before and after the needle valve. A differential pressure sensor (Endress-Hauser DeltabarS PMD75), which is rated for measuring the differential pressure of 0 to 298 kPa. The sensor is placed across the foam generation section to measure the pressure drop and control the degree of shearing. For the present study, a differential pressure of 248-298 kPa was maintained across the foam generation section.

Test Section

Three stainless steel tubes (ID's of 3.048 mm, 6.223 mm, and 12.573 mm) and two annulus sections (3.05 mm OD x 12.57 mm ID, 9.53 mm OD x 12.57 mm ID) serve as the test sections. The length between pressure taps is 0.838 m for medium pipe, and 0.8314 m for all other sections. Fluid density, temperature, and flow rate in the test section are measured with a Coriolis flowmeter (Endress-Hauser Promass 83A). Pressure drop measurements are performed by two, parallel-connected differential pressure sensors (Endress-Hauser DeltabarS PMD75). They are calibrated to read pressures between the ranges 0 – 10 kPa and 0 to 300 kPa. The entry lengths of the test sections are 50 times their internal diameter. Pressure gauges and relief valves (set at 3000 psi) are installed both at upstream and downstream of the test sections. The discharge valve at the end of the test section is used both for attaining desired foam quality and depressurization after completion of the test. A data acquisition system that uses a VBA program to display measured parameters and control fluid temperature.

4.3 Experimental Procedure

4.3.1 Test Fluid Preparation

Base liquid with PAC polymer was prepared by adding a measured quantity of powdered polymer to one liter of tap water and mixing using a low-shear propeller type variable speed mixer (Figure 4.4). The initial mixing was performed at high speed, followed by 20 minutes of low speed mixing to prevent the formation of fisheyes and ensure complete dispersion of the polymer. The suspension was left to hydrate for 24 hours and its rheology was measured. The hydrated suspension was transferred back to the blender cup, and 2% by volume of liquid anionic surfactant was added using a syringe while running the blender at low speeds. High-speed mixing is avoided to prevent air entrapment that can cause bubble formation in the fluid sample.

Figure 4.4: Variable speed benchtop mixer

4.3.2 Removal of Air from System

The test sample was poured in the base liquid tank and introduced into the flow loop using the gear pump. Each test section was filled up sequentially, ensuring fluid return at the discharge. Finally, the bleed line was filled up with base liquid by opening the bleed valve. While pumping

test fluid in the flow loop, air can get trapped in the high points which will contaminate the pure N_2 foam. The removal of trapped air was performed by recirculating the test fluid to the open tank, through a completely immersed discharge line. The flow was alternatively directed through each test section while working the valves in the corresponding line. The process was continued until no air bubbles were observed in the transparent discharge line and the liquid tank.

4.3.3 Setting Foam Quality

To generate foam, nitrogen from a pressurized cylinder was injected into the flow loop using bonnet needle valves while the fluid was recirculated at the maximum flow rate (0.55 L/min). A check valve, downstream of the bonnet needle valve prevented the backflow of gas from the loop. A pressure regulator on the nitrogen cylinder was used to achieve the desired pressure.

A mixture of base liquid and nitrogen gas was recirculated through a needle valve, which was throttled to provide the necessary shear energy for foam generation. The throttling level was kept constant by measuring the differential pressure across the needle valve (248-298 kPa). Static mixers having no rotating parts placed both upstream and downstream of the needle valve maintained the homogeneity of the foam. A Coriolis flowmeter measured the foam density, from which the foam quality is determined. Consistent measurements of quality indicated the completion of the foam generation process and demonstrated its stability and homogeneity. The foam quality was varied by carefully draining foamed from the discharge valve and adding more gas in the system.

4.3.4 Flow Data Acquisition

After generating stable foam, pressure drop measurements were performed across each test section varying foam flow rates. Fluid density and temperature for each test case were recorded

simultaneously. Ten measurements were recorded at each foam flow rate, for consistency and reliability of the recorded data. A visual basic code was used to collect and record the gathered data. The foam texture changes while performing each set of measurements due to bubble coalescence and gravity drainage. To maintain uniformity in the level of foam generation for all test cases, the foam was regenerated between two consecutive tests by circulating foam through the test section at the maximum rate (0.55 L/min) for 60 seconds as shown in Figure 4.5.

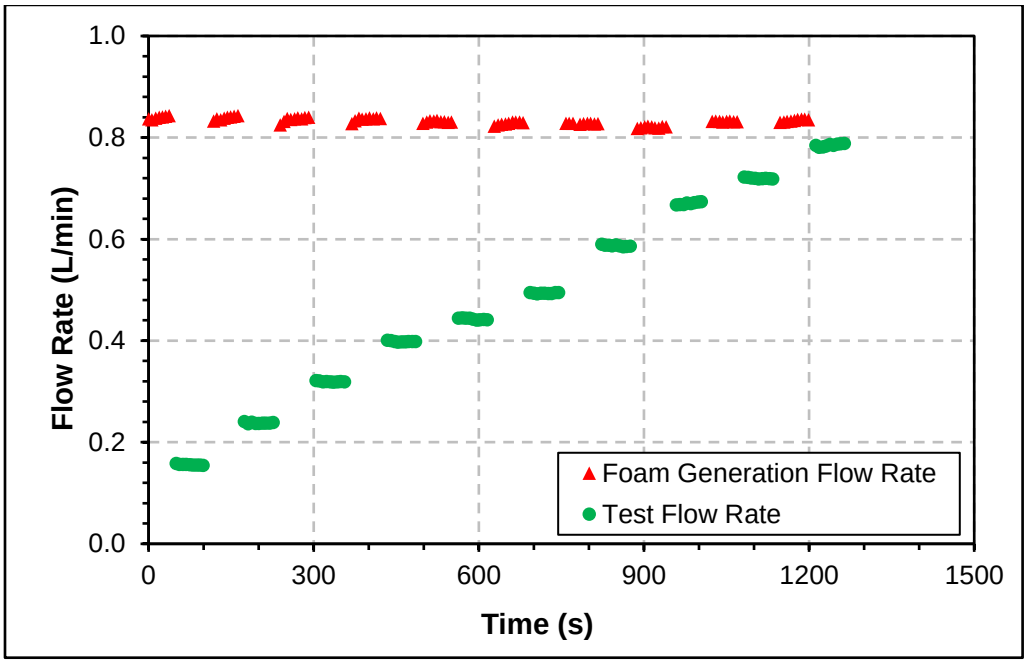

Figure 4.5: Flow rate variation during the experiments

4.3.5 Determination of Yield Stress

High-quality foams have an inherent structure and can display viscoplastic behavior. Hence, they act as solids below a critical shear stress value, (also called yield stress) and resist a finite deformation like solids. Yield stress for non-Newtonian fluids can be determined by observing shear deformation in fluids with increasing values of stress. This technique, however, cannot be employed for foams, because they degrade with time due to gravity drainage and bubble coalescence. Therefore, an experimental procedure was devised (Akhtar *et al.*, 2018) as a variation

of the “stress relaxation” technique employed by Khan *et al.*, (1988) to obtain yield stress measurements in a pipe viscometer by bringing the foam to a static condition immediately from a dynamic state.

To obtain yield stress using the stress relaxation method, the desired quality foam was first generated at test pressure and temperature by circulating fluid at the maximum flow rate for 10 minutes before shutting down the pump completely. As opposed to fluids with no yield, upon shutdown, the high-quality aqueous foams exhibited a “recoiling phenomenon”, which was manifested as a negative pressure gradient across the needle valve and a unique differential pressure trend that showed an abrupt reduction, followed by a slight differential pressure recovery to a peak value, and then a steady decline. The “peak” or the “plateau” value of the differential pressure was then converted to wall shear stress and identified as the yield stress of the foam fluid. The test was repeated to ensure the reproducibility of results and the average of the values is taken as the final yield stress.

4.4 Test Matrix

PAC polymer-based foams were tested to analyze the effect of temperature on the rheology, at a pressure of 6.9 MPa. Table 4-4 shows the foam formulations used and the test variables for the elevated temperature foam tests.

Table 4-4: Foam formulation and test variables

Pressure (MPa)	6.9					
Temperature (°C)	23 ± 2	52 ± 2	79 ± 2	107 ± 2	127 ± 2	149 ± 2
Tube Sizes (mm)	Tube: 3.05, 6.22, and 12.57 mm ID. Annulus: 12.57 mm ID × 9.53 mm OD					
Flow Rates (% of 0.55 L/min)	10, 20, 30, 40, 50, 65, 80, 90, 100					
Liquid Phase	Water + 0.25% PAC (by wt.)					
Gaseous Phase	Nitrogen					
Surfactant	Howco-Suds™ Foaming Agent					
Surfactant Conc. (vol. %)	2%					
Foam Qualities (%)	0, 45, 55, 65, 75					

4.5 Calibration Tests

A set of calibration tests were conducted to establish the accuracy and repeatability of the experimental study. The following sections briefly discuss the results of these calibration tests.

4.5.1 Pipe Viscometer Calibration

The recirculating pipe viscometer calibration was performed by Akhtar (2017), by comparing rheological measurements to rotational OFITE 900 viscometer with Newtonian mineral oil (Drakeol® 10 LT MIN OIL NF) at ambient conditions (23.9°C). Flow data from pipe viscometers were obtained under laminar flow conditions (i.e. Reynolds number less than 2100). Rheological measurements from different diameter pipe viscometers lie on the same flow curve, indicating no wall slip (Figure 4.6). Additionally, rotational viscometer data coincided with the pipe data, which validated the pipe viscometer. The slope of the straight line passing through origin indicated a viscosity of 0.0335 Pa-s (33 cP).

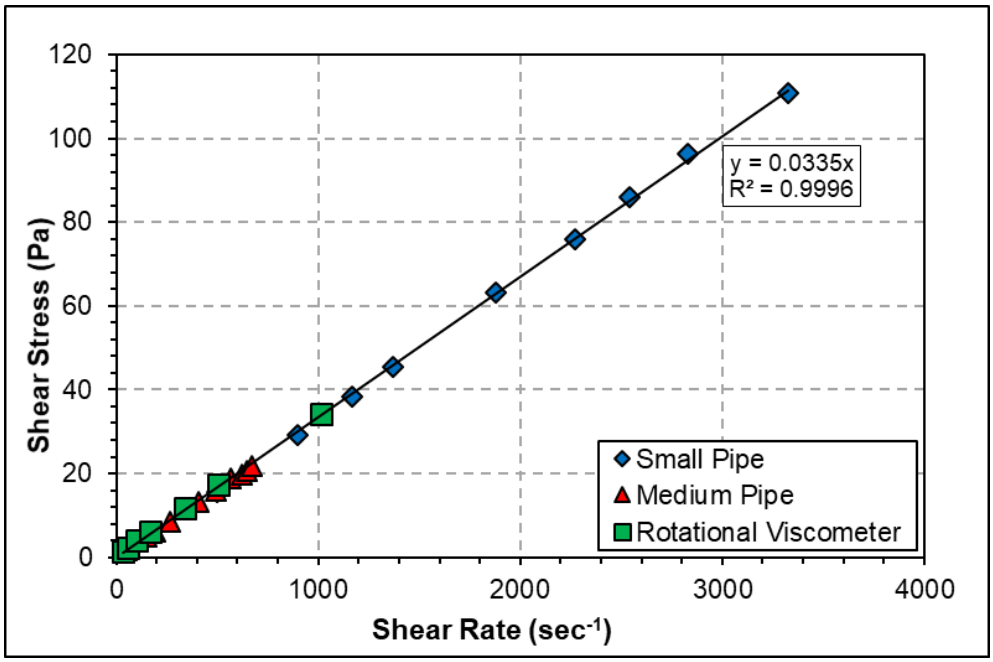

Figure 4.6: Rheograms from pipe and rotational viscometers (Akhtar, 2017)

4.5.2 Static Aging of PAC Base Liquid

After preparing 0.25% PAC polymer base fluid, the solution was kept at ambient conditions and allowed to hydrate and build viscosity over a period of seven days. Viscosity measurements were conducted at 24-hour intervals in OFITE rotational viscometer with temperature control set at 23.9°C. Minimal change in rheology was observed with time (Figure 4.7). The flow curves overlapped, and the data was adequately described using the power-law model fluid behavior. The flow behavior index was very close to one (n = 0.903), indicating an almost Newtonian behavior.

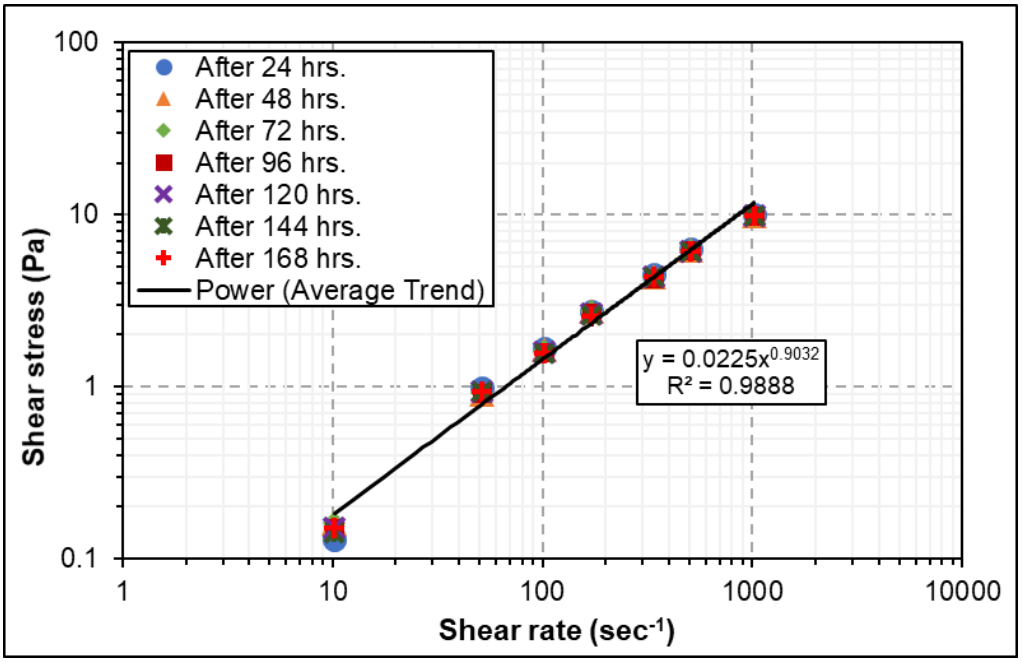

Figure 4.7: Results of static aging of base liquid (0.25% PAC)

4.5.3 Thermal Stability of PAC Base Fluid

Commercial PAC polymer (POLYPAC-R) is designed to be stable up to a maximum temperature of 149°C. To establish its thermal stability and quantify the effect of high temperatures on the rheological measurements of PAC base fluids, a polymer degradation study was performed (Akhtar, 2017). Rheology measurements were performed before and after foam flow experiments using a rotational viscometer. Liquid settling out of the foam loop experiments was collected and cooled down to ambient conditions before performing rheology measurements. The fluid-preserved its original flow properties (rheology) after exposure to high temperature (149°C) and high shear for an extended time in the flow loop (Figure 4.8). Therefore, PAC was thermally stable for the ranges of temperature and shearing level considered in the present experimental investigation.

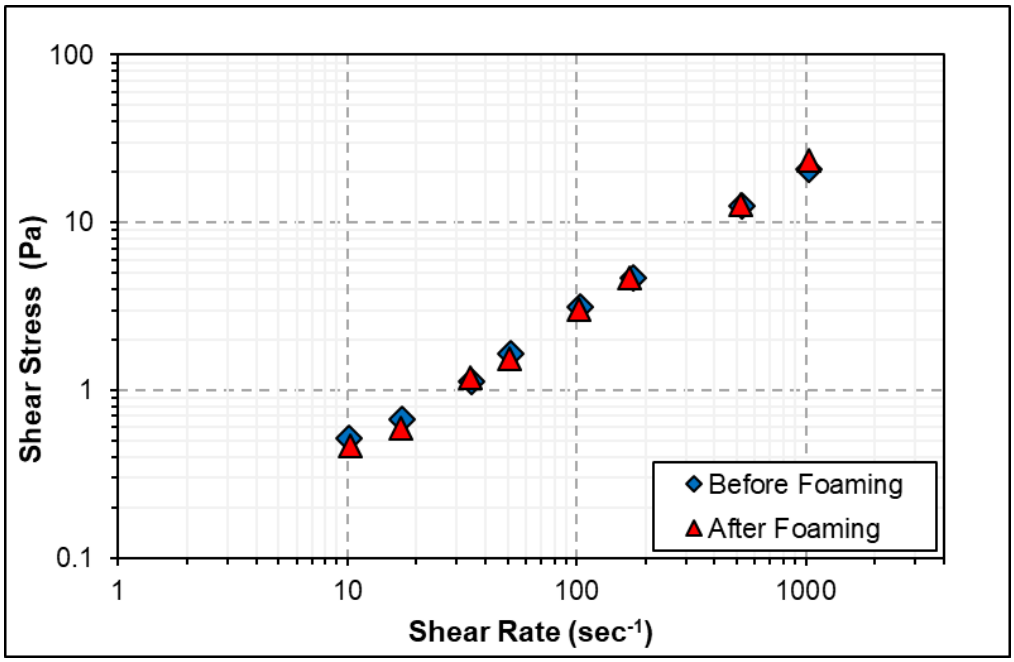

Figure 4.8: Rheograms of base fluid (0.25% PAC + Water) before and after high-temperature foam rheology experiments (Akhtar, 2017)

Chapter 5

Results and Discussion

The purpose of rheological measurements is to determine the relationship between the wall shear stress and wall shear rate for a fluid. The wall shear stress (τ_w), is obtained from the measured differential pressure across the pipe viscometers using Eq. (3.7). Foam is a non-Newtonian fluid that exhibits shear-thinning behavior and is characterized by a generalized flow behavior index defined in Eq. (3.17a). The wall shear rate for non-Newtonian fluid flowing in a pipe is computed from the nominal Newtonian shear rate using Eq. (3.19).

5.1 Verification of Laminar Flow Regime

For determining foam rheology, all pipe flow measurements were performed in the laminar flow regime ($Re < 2100$). Considering foam as power-law fluid, the generalized Reynolds number is calculated as:

$$Re = \frac{\rho_F u^{2-n_F} D^{n_F}}{8^{n_F-1} K_F ((3n_F + 1)/4n_F)^{n_F}} \tag{5.1}$$

where ρ_F is the density of the foam. The power-law model parameters for foam (n_F) and (K_F) are determined from the slope and intercept of the plot of logarithmic wall shear stress and nominal Newtonian shear rate. The highest Reynolds number observed during the tests was 2042 for the base fluid at 300°F.

The measured Fanning friction factor is determined from the wall shear stress calculated from Eqs. (3.23) and (3.24). Theoretical Fanning friction factor ($f = 16/Re$) is compared to the measured values to evaluate discrepancies. The apparent viscosity of foam (η) is determined using the following expression:

$$\mu_F = K_F(\dot{\gamma}_w)^{n_F-1} \tag{5.2}$$

Figure 5.1 shows the Fanning friction factor vs Reynolds number for the base liquid and 75% quality foam at all test temperatures. Due to its low viscosity and high density, the base fluid resulted in higher Reynolds numbers as compared to 75% quality foam. At elevated temperatures and high shear rates (i.e. in a small pipe), the fluid flow was in the turbulent regime, especially for the base liquid. Furthermore, in some cases due to reduced viscosity at elevated temperature, the measurements remained even below the differential pressure transmitter measuring range. Therefore, very low differential pressure readings (less than 400 Pa) were not considered during the rheological analysis. The comparison of actual and theoretical Fanning friction factors indicated that the turbulent flow regime begins at Reynolds number value of approximately 2300. Power-law fluids have a different critical Reynolds number value that dictates the transition from laminar to the turbulent flow regime; and therefore, the onset of turbulence was delayed.

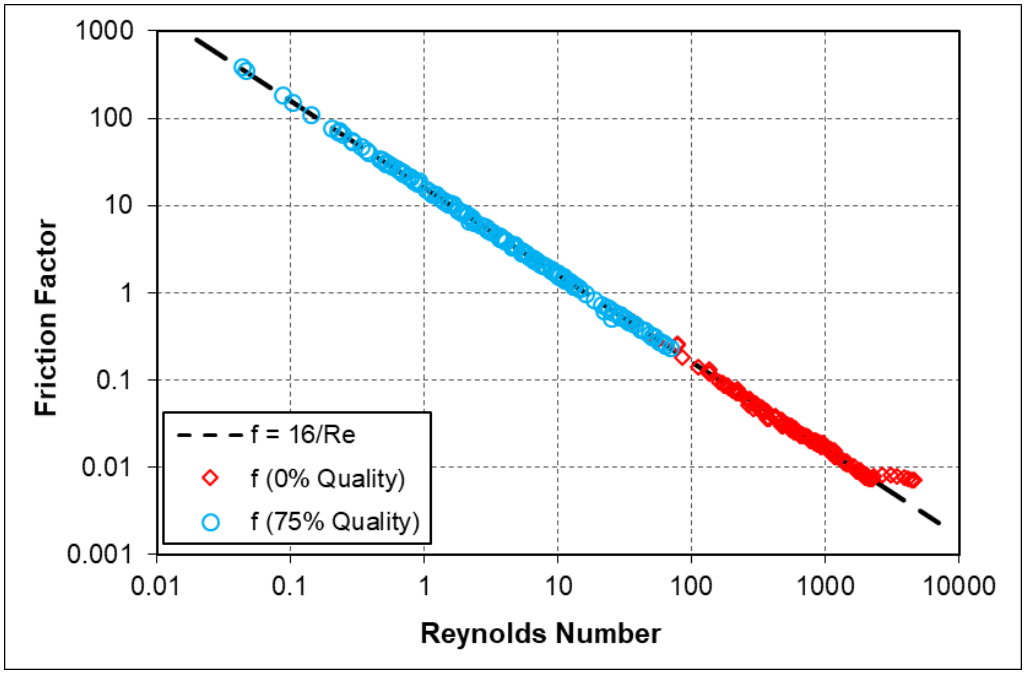

Figure 5.1: Fanning friction factor versus Reynolds number

5.2 Rheology of PAC Foam

All tests were conducted at 6.89 MPa (1000 psi) pressure and varying temperature (23.8 to 148.9°C) and foam quality (0 to 75 %). Temperature variations during the tests remained within ±1%. Figure 5.2 shows the rheograms obtained from flow tests conducted at 79ºC and different foam qualities. The results demonstrate that the fluids could be adequately described using the power-law fluid model. The shear-thinning behavior of foams augmented with foam quality as can be observed from the reduction of fluid behavior index 'n_F'. Flow behavior index is obtained from the slope of the plot of logarithm of wall shear stress versus logarithm of nominal Newtonian shear rate, i.e., $\log(\tau_w)$ vs. $\log(8u/D)$. The reduction is attributed to the evolution of a rigid bubble structure in foams (Ahmed *et al.*, 2003a; Herzhaft *et al.*, 2005; Hutchins and Miller, 2003). Similar trends were observed in all the experiments conducted during this investigation.

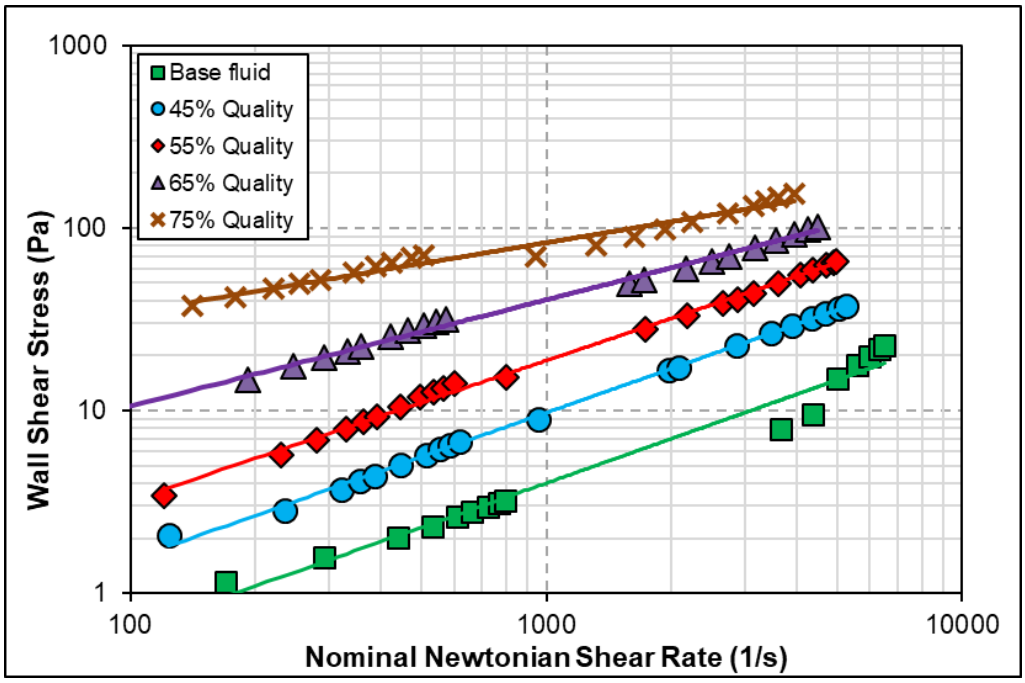

Figure 5.2: Rheograms of PAC foam at 79 ºC and different qualities

5.2.1 Effect of Foam Quality

With increasing foam quality, foam changes its bubble structure from a loosely packed to a more closely packed structure causing greater bubble interaction, which results in an increase in viscosity (Section 2.10.1). Figure 5.3 and Figure 5.4 shows the rheograms of PAC foams for varying foam qualities and test temperatures (24 and 107ºC), respectively. Regardless of the temperature, foam viscosity increased with quality as previously reported by other studies (Akhtar *et al.*, 2018; Gu and Mohanty, 2015b; Sherif *et al.*, 2015a, 2015b). The base fluid viscosity and bubble structure stability are related strongly, therefore, the effect of quality was more pronounced at low temperature (24ºC) than elevated temperature (107ºC).

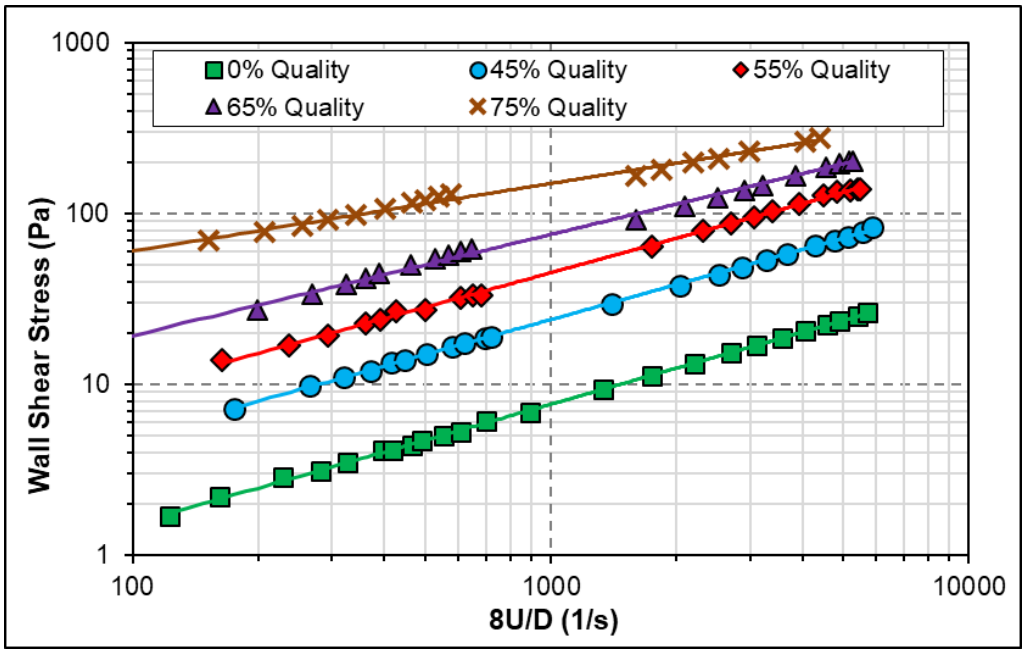

Figure 5.3: Rheograms of PAC foam at 24ºC and different qualities

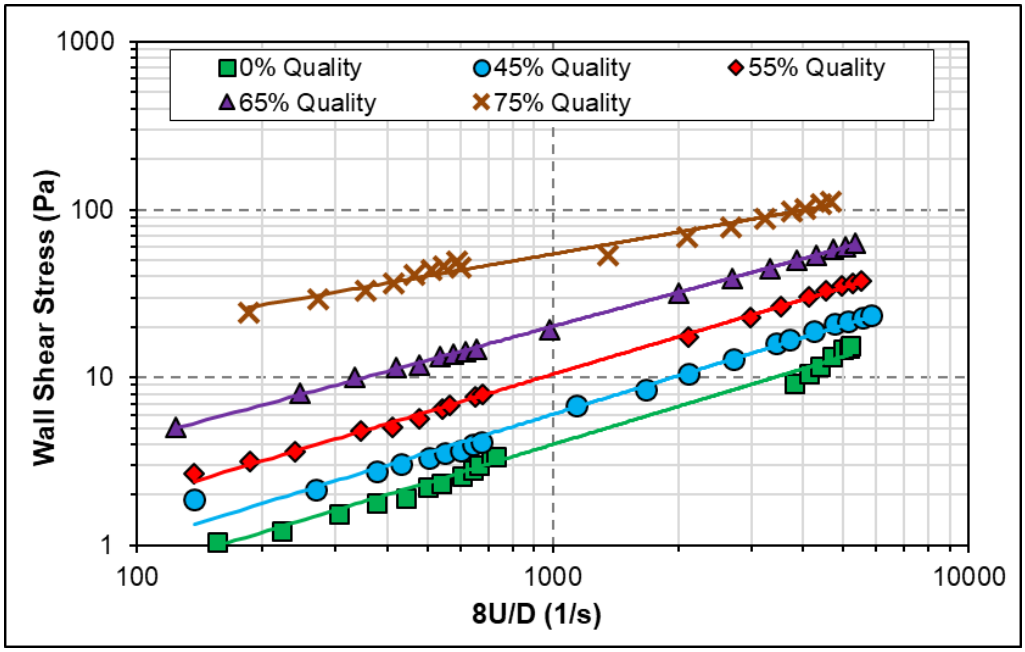

Figure 5.4: Rheograms of PAC foam at 107ºC and different qualities

Fluid rheological measurements indicated a significant increase in fluid consistency index (K_F) and a moderate reduction in fluid behavior index (n_F) with foam quality. At ambient temperature (24ºC), K_F increased from 0.0565 to 8.12 Pa-s^n as the quality was raised from 0 to 75%, while at 107ºC, it increased from 0.0169 to 2.17 Pa-s^n.

Since base fluid viscosity decreases with temperature, the rheograms for all foam qualities shifted downward with temperature. Also, the fluid consistency index for a given foam quality decreased with temperature. This reduction was more pronounced for low-quality; therefore, the viscosity of high-quality foams is less sensitive to temperature than that of low-quality foams. Greater thermal stability of high-quality foam is attributed to the development of bubble structure which governs the foam rheology behavior (Harris, 1989; Herzhaft *et al.*, 2005). On the other hand, low-quality foams do not exhibit a strong bubble structure and their viscous nature is primarily determined by the viscous behavior of their constituent phases.

5.2.2 Effect of Temperature

With an increase in temperature, the base fluids viscosity decreased as its natural tendency to resist continuous deformation diminishes. Similarly, foam viscosity which is a strong function of base fluid viscosity decreases with temperature (Akhtar *et al.*, 2018; Bonilla and Shah, 2000; Gu and Mohanty, 2015b). Additionally, with a decrease in base fluid viscosity, film thickness reduces, resulting in increased foam drainage and foam instability, which explains the difficulty of foam generation at elevated temperatures. Figure 5.5 and Figure 5.6 present the apparent viscosity of base fluid and 75% quality foam at different test temperatures, respectively. As indicated by the slope of these curves (which is "$n-1$" for power fluids), the shear-thinning behavior of the base fluid and foam decreased with temperature. The fluid behavior index of the base fluid, obtained from these plots, increased from 0.700 to 0.834 while it showed limited change (from 0.404 to 0.499) for 75% foam as the temperature was raised from 24 to 149ºC. High-quality foams have a strong bubble structure, which is not directly affected by temperature. As a result, they tend to preserve their shear-thinning behavior as the temperature increases.

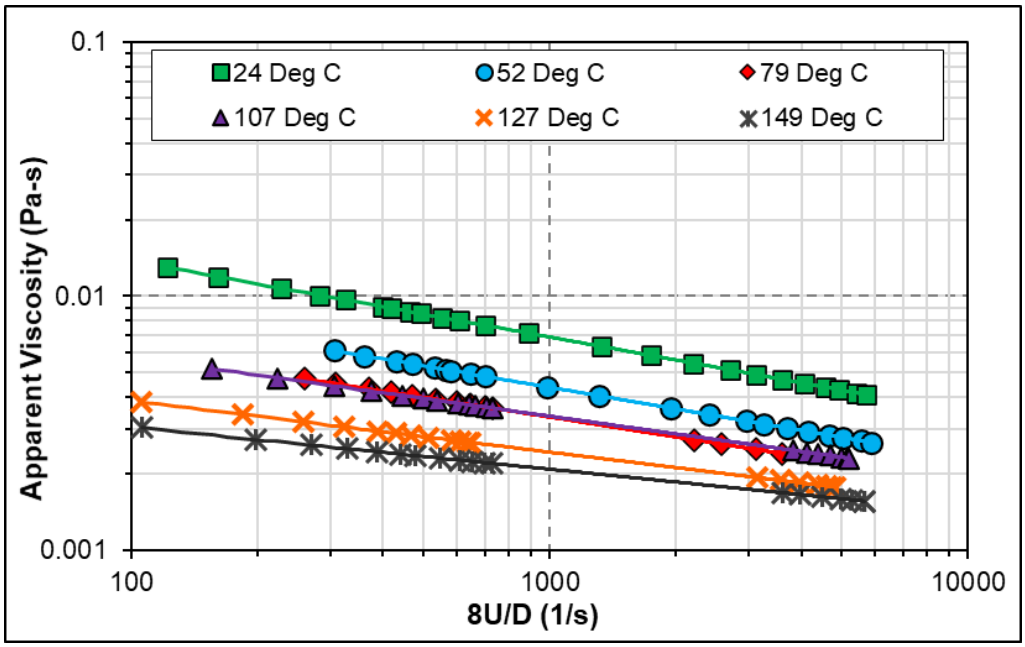

Figure 5.5: Apparent viscosity of the base fluid at different temperatures

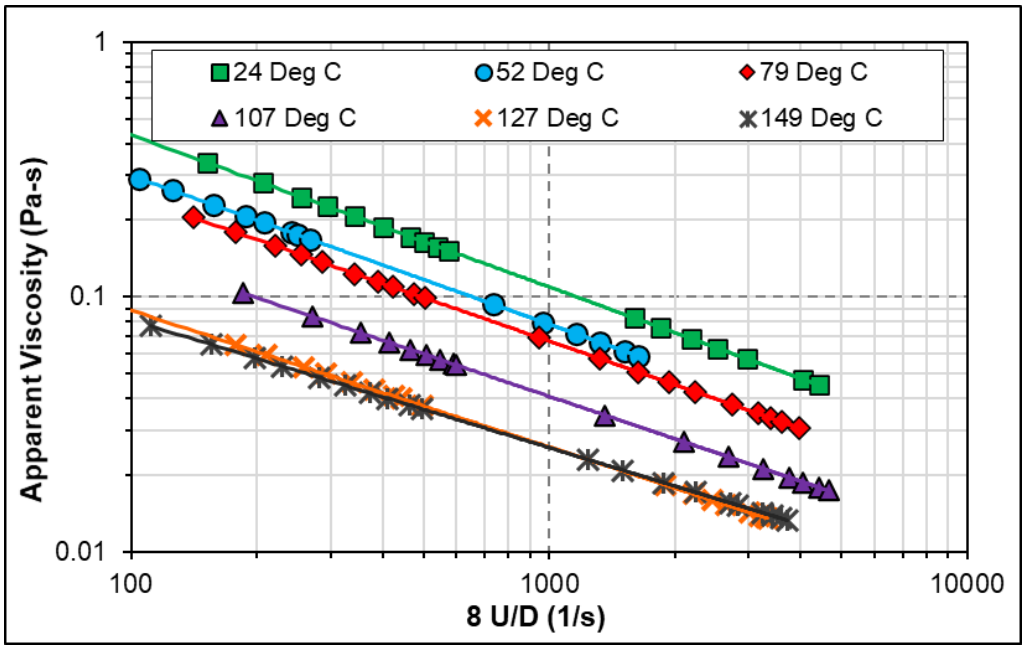

Figure 5.6: Apparent viscosity of 75% quality PAC foam at different temperatures

5.3 Determination of Yield Stress

The presence of yield stress in foams has been reported by a number of studies (Bonilla and Shah, 2000; Gopal and Durian, 1999; Nguyen and Boger, 1992; Reidenbach *et al.*, 1986; Saintpere *et al.*, 2000a; Sani *et al.*, 2001). Mostly, the yield stress of foam is obtained through data

fitting, which is prone to inaccuracies due to extrapolation. In the present study, the "stress relaxation" technique was used to measure the yield stress of foam. All tests were conducted in the medium pipe (6.35 mm) at 6.89 MPa and varying temperature and foam quality. Only high-quality foams (75%) displayed yield stress at ambient temperature, which is in accordance with other studies (Akhtar *et al.*, 2018; Kraynik, 1988), who reported similar observations at high foam qualities.

The "stress relaxation" technique involved abruptly stopping circulation completely and observing the trend of wall shear stress plot with time. Figure 5.7 displays the wall shear stress and needle valve pressure drop variations with time when foam circulation was suddenly stopped at the start of the 13th second as shown in Figure 5.8. For the purpose of measurement analysis and interpretation, the wall shear stress plot is divided into four different sections, i) constant flow rate regime (Regime I); ii) flow deceleration regime (Regime II); iii) fluid recoiling regime (Regime III), and iv) degradation regime (Regime IV).

For fluid that does not exhibit yielding, the flow resistance (wall shear stress) reduces to zero, when the flow is stopped; however, in case of high-quality foam, the wall shear stress reduced to 5 Pa and then began to increase as a result of the recoiling phenomenon. The recoiling observed in Regimes II and III of Figure 5.7 is the typical behavior of yielding fluids. Additionally, the recoiling resulted in the reversal of pressure drop across the needle valve. Wall shear stress plateaued at a value of 8 Pa. With time, the yielding behavior diminished due to loss of foam structure and liquid drainage (Regime IV). Consequently, the pressure drop across the needle valve began to decrease and the wall shear stress started to decline.

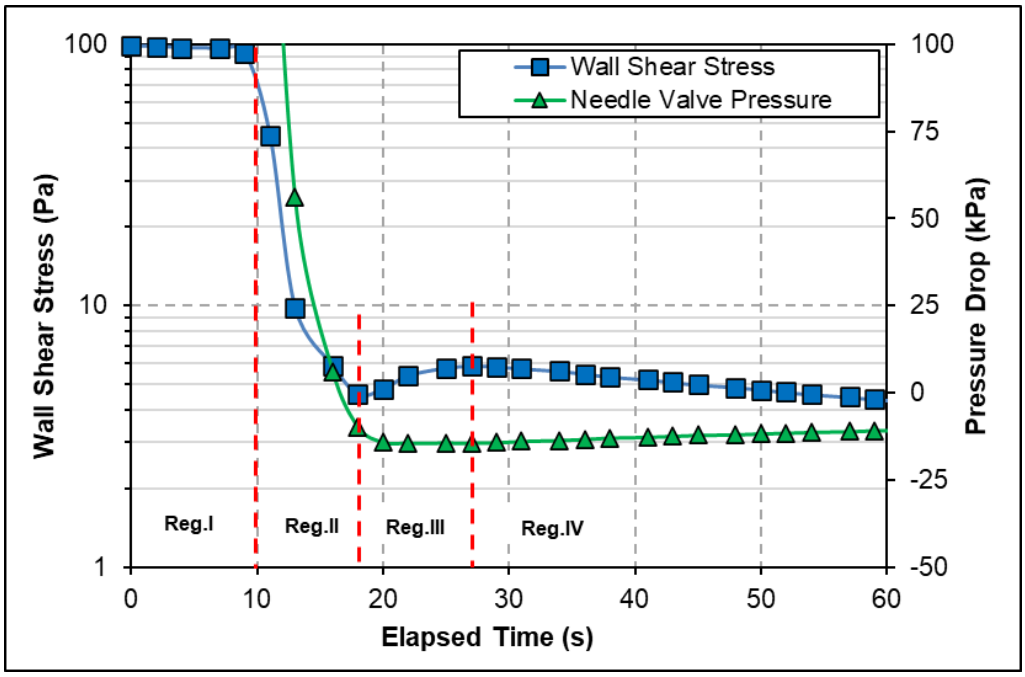

Figure 5.7: Variation of wall shear stress and needle valve pressure loss with time (D = 6.22 mm, 75% quality at 6.89 MPa)

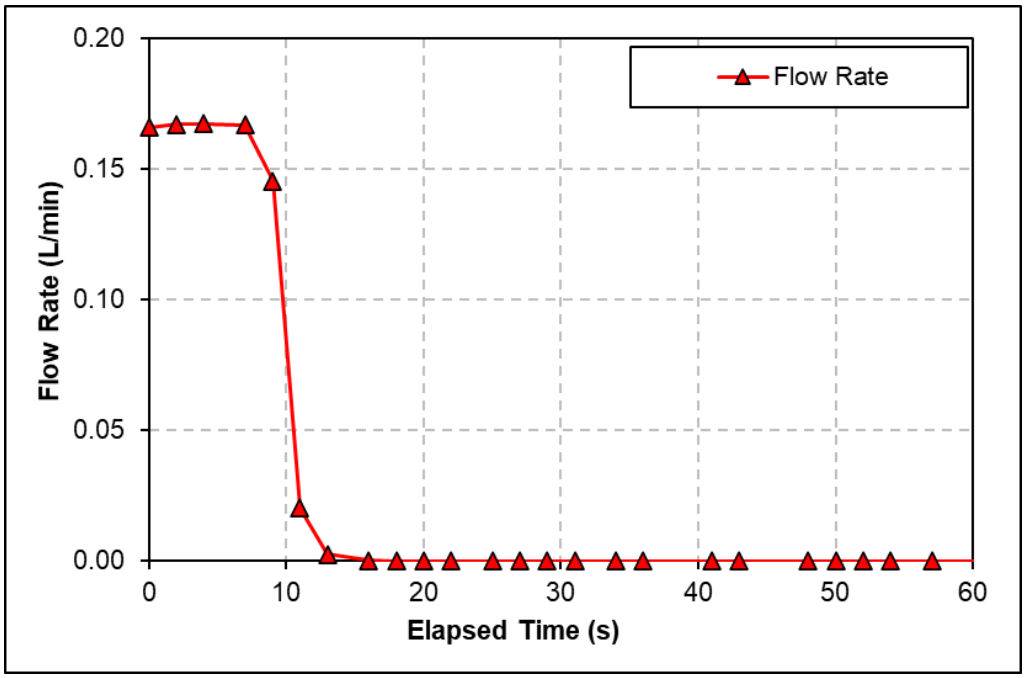

Figure 5.8: Variation of flow rate with time (D = 6.22 mm, 75% quality at 6.89 MPa)

High-quality foams either display a distinctive peak or a plateau on the wall shear stress plot which corresponds to the yield stress of the fluid (Figure 5.9). On the other hand, foams with quality less than 70% demonstrated minor yielding (Fig. 5.10). Results showed a gradual decrease

in wall shear stress when the flow was suddenly stopped. No peak or plateau was observed for 65% quality foam.

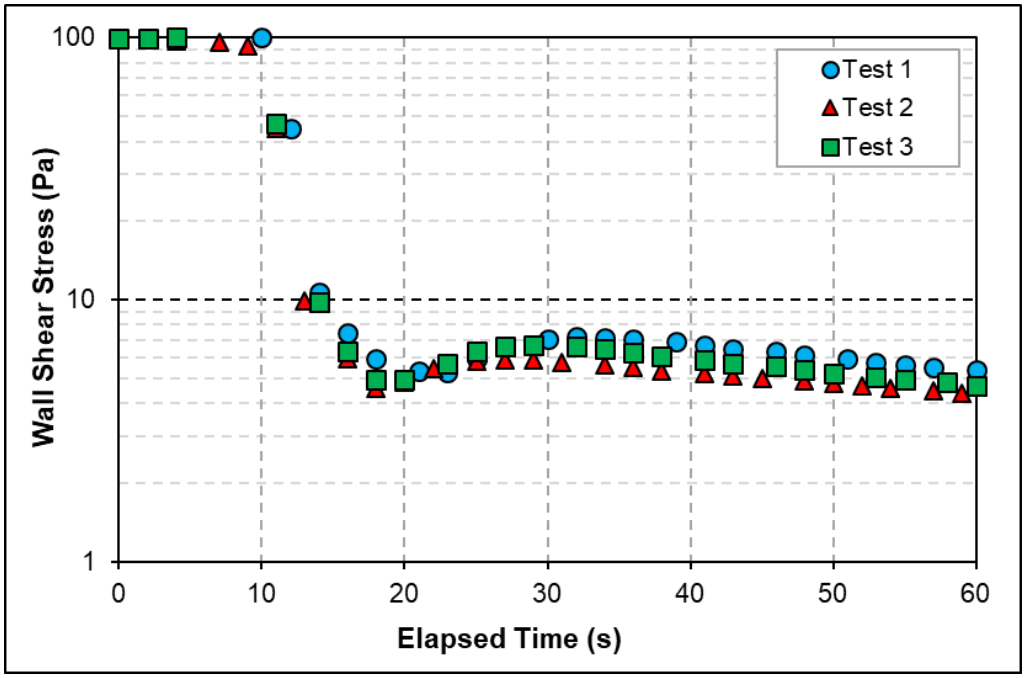

Figure 5.9: Wall shear stress vs. time for the medium pipe at 6.89 MPa for 75% quality foam at ambient temperature

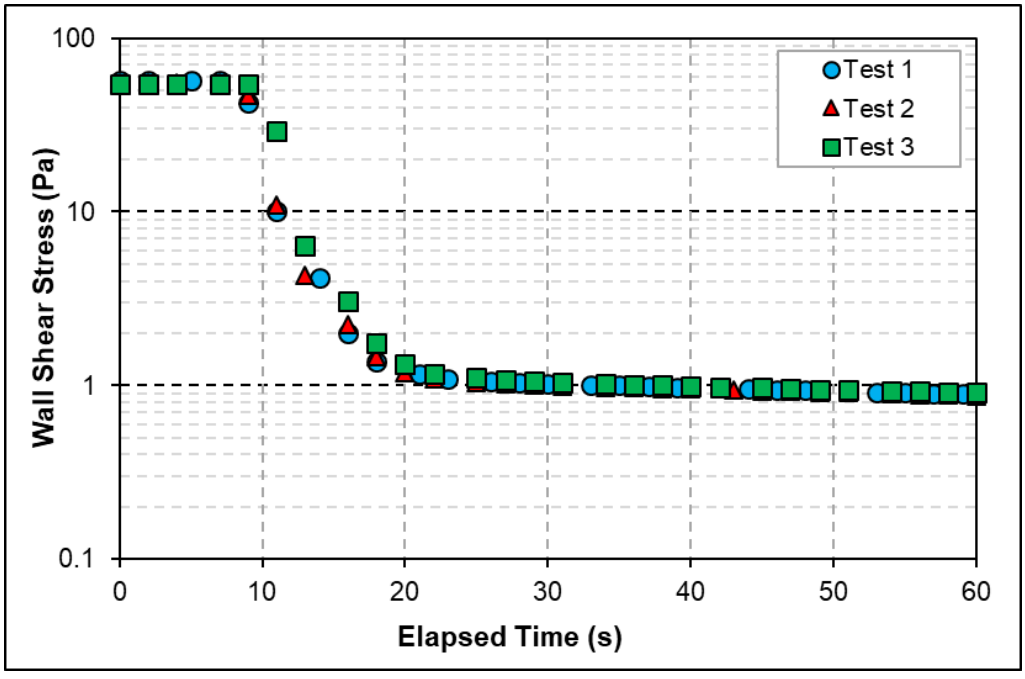

Figure 5.10: Wall shear stress vs. time for the medium pipe at 6.89 MPa for 65% quality foam at ambient temperature

At elevated temperatures, foam bubble rigidity and stability are compromised due to the thermal thinning of the fluid laden bubble film. This results in a weakening of bubble structure and therefore, tests conducted at elevated temperature did not provide consistent results (Figure 5.11) indicating a complete loss of yielding behavior.

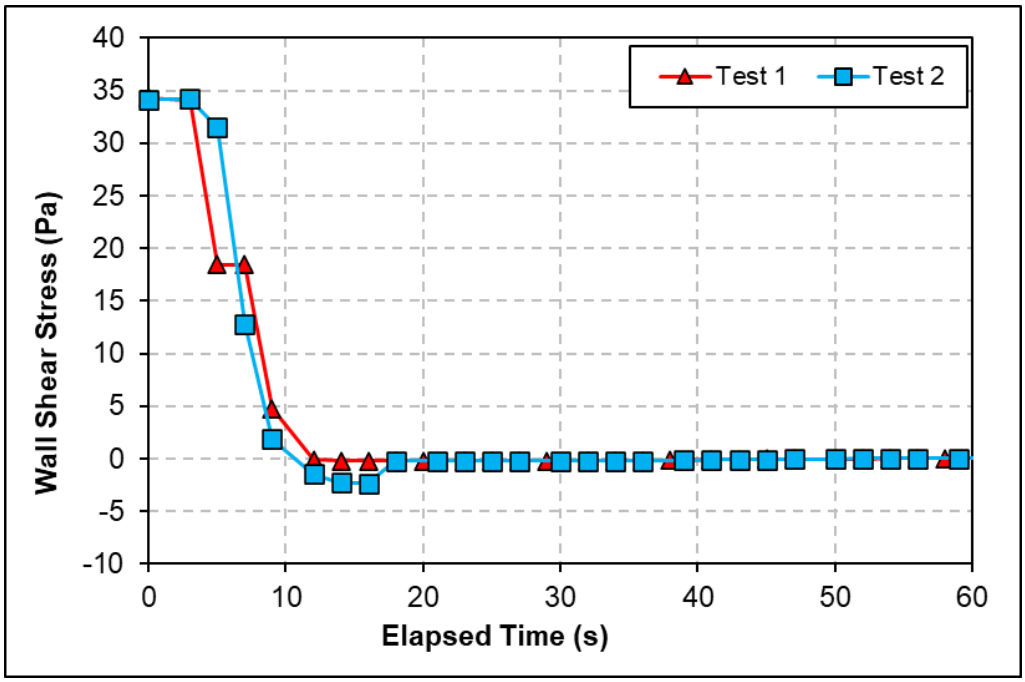

Figure 5.11: Wall shear stress vs. time for the medium pipe at 6.89 MPa for 65% quality foam at ambient temperature

5.4 Development of Correlations for Foam Rheology

Based on the discussion presented in Sections 5.2 and 5.3, it was established that foam rheology is a function of its quality, base fluid rheology, and temperature. Since for shear rate considered in this investigation, foam and its base liquid can be adequately described using the power-law rheology model (yield power-law model can be more accurate for high-quality foams), expressions for model parameters, n_F and K_F are developed relating, them to the aforementioned governing variables. It should be noted that previous studies by (Akhtar, 2017) have shown the negligible effect of system pressures (i.e. secondary effects) on foam rheology, and therefore, all

measurements were obtained at 6.89 MPa (1000 psig). Correlations were developed using curve fitting techniques for both base fluid and foams at different temperatures and qualities.

5.4.1 Expressions for Base Fluid Power Law Parameters

The temperature has a significant effect on the rheology of the base fluid. At elevated temperature, the fluid displays reduced shear thinning behavior. Figure 5.12 shows the plot of relative fluid behavior index (i.e. fluid behavior index which is normalized with its corresponding values at ambient temperature 24°C, $\frac{n_L}{n_{24}}$). The relative fluid behavior index increased slightly (up to 25%) with temperature. Nevertheless, the plot of a normalized consistency index $\left(\frac{K_L}{K_{24}}\right)$ showed a tenfold reduction with temperature, indicating the sensitivity of the base fluid viscosity to the temperature (Figure 5.13).

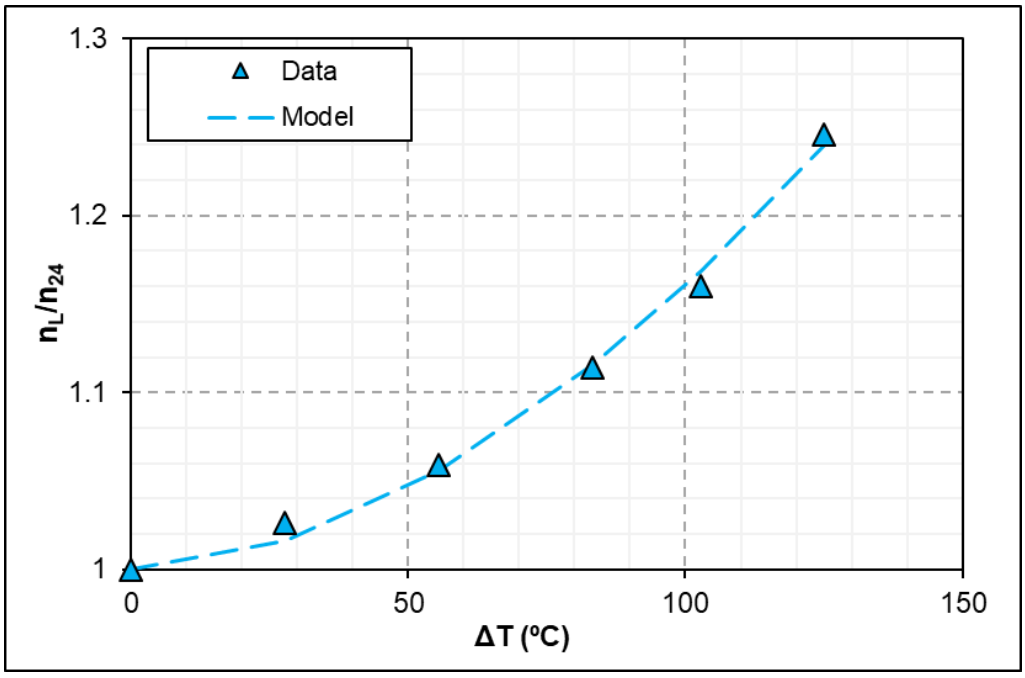

Figure 5.12: Normalized fluid behavior index with temperature

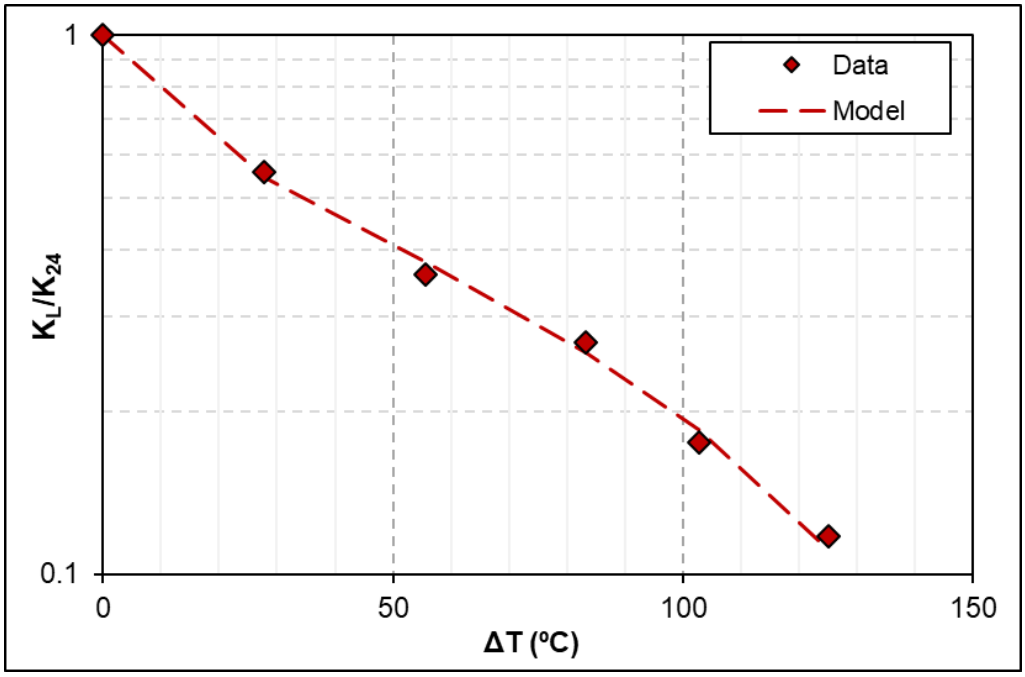

Figure 5.13: Normalized flow behavior index with temperature

Nonlinear regression was applied to plots of relative fluid behavior (n_L/n_{24}) and consistency index (K_L/K_{24}) as a function of temperature change ($\Delta T = T - 24$, ºC) to develop empirical correlations for base fluid rheological parameters. The final mathematical expressions relating base fluid rheological parameters to temperature are:

$$\frac{n_L}{n_{24}} = 1 + 4.162 \times 10^{-5}(\Delta T)^{1.7934} \quad (5.3a)$$

$$\frac{K_L}{K_{24}} = 1 - 0.10397(\Delta T)^{0.4444} \quad (5.3b)$$

5.4.2 Expressions for Foam Power Law Parameters

Foam rheology is governed primarily by the base fluid rheology and foam quality. Foam fluid behavior index decreased slightly with temperature while there was a significant reduction of consistency index. To analyze the relative change, in the foam fluid rheological parameters (n_F and K_F) at a given temperature, the parameters were normalized with the base fluid properties at

the same temperature. Figure 5.14 and 5.15 respectively show the normalized foam fluid behavior index ($\frac{n_F}{n_L}$), and the normalized foam consistency index ($\frac{K_F}{K_L}$) as a function of foam quality for different temperatures.

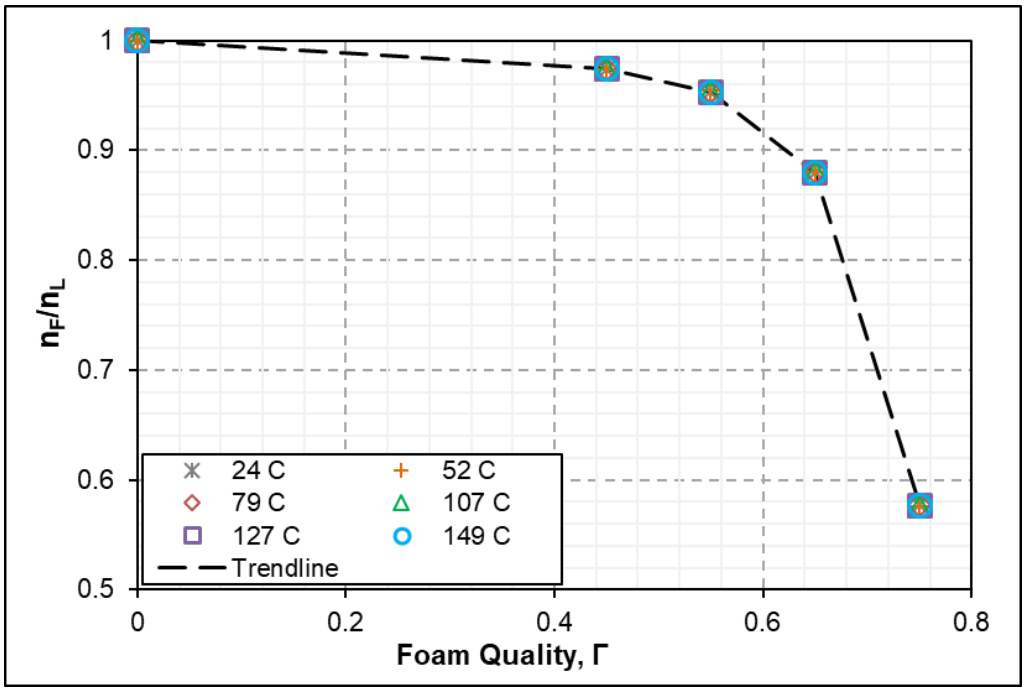

Figure 5.14: Normalized foam flow behavior index with different qualities at different temperatures

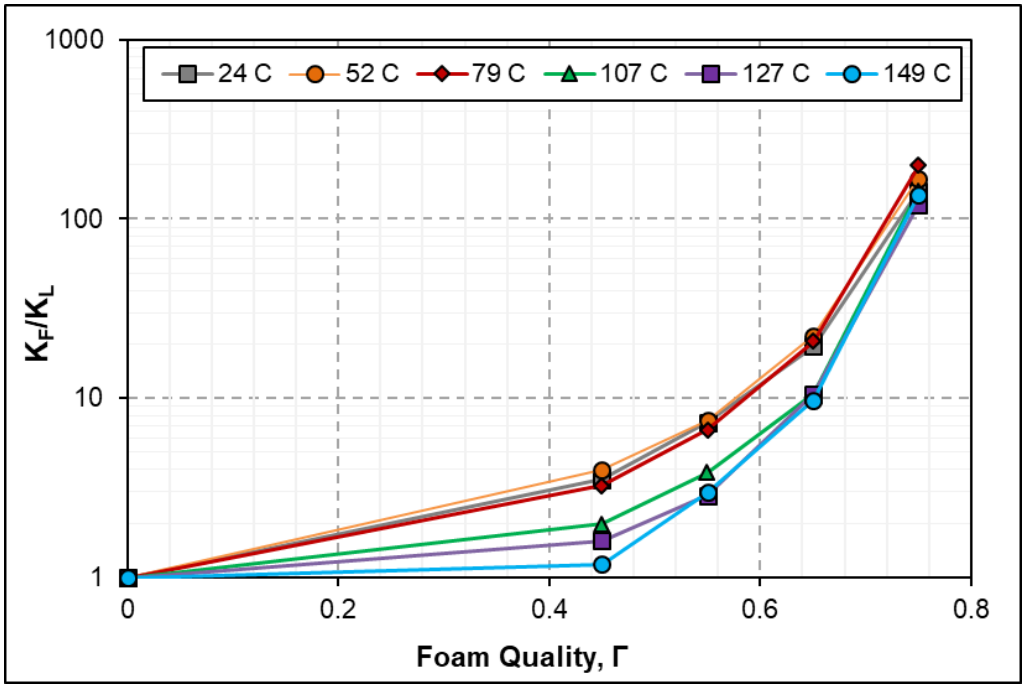

Figure 5.15: Normalized foam consistency index with foam quality and different temperatures

The normalized fluid behavior index is primarily dependent on the foam quality and is not affected by temperature, which demonstrates a minimal impact of temperature change on the foam structure. Furthermore, both the foam and the base fluid flow behavior indices are influenced by temperature in the same magnitude. Regression analysis is applied using the data collected at different foam qualities (0 to 75%) and temperatures (24 to 149°C). The Reynolds number for each data point is determined to verify the establishment of laminar flow conditions during the test. The final expression for relative foam behavior index as a function of foam quality is given as:

$$\frac{n_F}{n_L} = Exp(-0.015934 - 11.32057[\Gamma]^{10.6129}) \quad (5.4a)$$

The normalized consistency index of foam not only varies with quality but also with temperature. The temperature impacts consistency index more significantly in foams than the base fluid and the influence is more pronounced in intermediate quality foams (30 to 50%) as observed in Figure 5.15. Also, the effect of quality on the relative consistency index is moderate at low

qualities (less than 55%) and becomes significant at high qualities (greater than 55%). Similarly, nonlinear regression is applied to develop expressions for this variable as a function of quality. Thus:

$$\frac{K_F}{K_L} = Exp(\alpha_1 + \alpha_2[\Gamma]^{\alpha_3}) \tag{5.4b}$$

where the empirically obtained constants (α_1,α_2, and α_3) are functions of change in temperature ($\Delta T = T - 24$, ºC). The equations to evaluate the constants are provided in Table 5-1. The foam rheological parameters used to develop these correlations are provided in 0.

Table 5-1: Equations for coefficients of rheological parameters

$\boldsymbol{\alpha_1}$	$-3.24 \times 10^{-7}.\Delta T^3 + 3.76 \times 10^{-5}.\Delta T^2 - 5.57 \times 10^{-4}.\Delta T + 0.06248$
$\boldsymbol{\alpha_2}$	$22.9125 - 11.58403/[1 + (1.2946 \times 10^{-2}.\Delta T)^{4.13264}]$
$\boldsymbol{\alpha_3}$	$5.1324 - 2.1695/[1 + (1.454 \times 10^{-2}.\Delta T)^{6.73039}]$

5.5 Comparison of Model Predictions with Experimental Measurements

To check the model accuracy, measured wall shear stress values are compared with model predictions. Figure 5.16 and 5.17 show the actual measurements versus model predictions plots at different temperatures (24 and 149°C). The average deviation is calculated at each foam quality and it remained fairly constant at a given temperature (9% at 24ºC, 13% between 52 to 127ºC, and 12% at 149ºC). At elevated temperature, the rheograms of low-quality foams band together with that of the base fluid, which is related to the changes in the base fluid rheology at high temperatures. Furthermore, at high shear rates, the rheograms taper slightly, indicating a marginally reduced influence of temperature on fluid behavior.

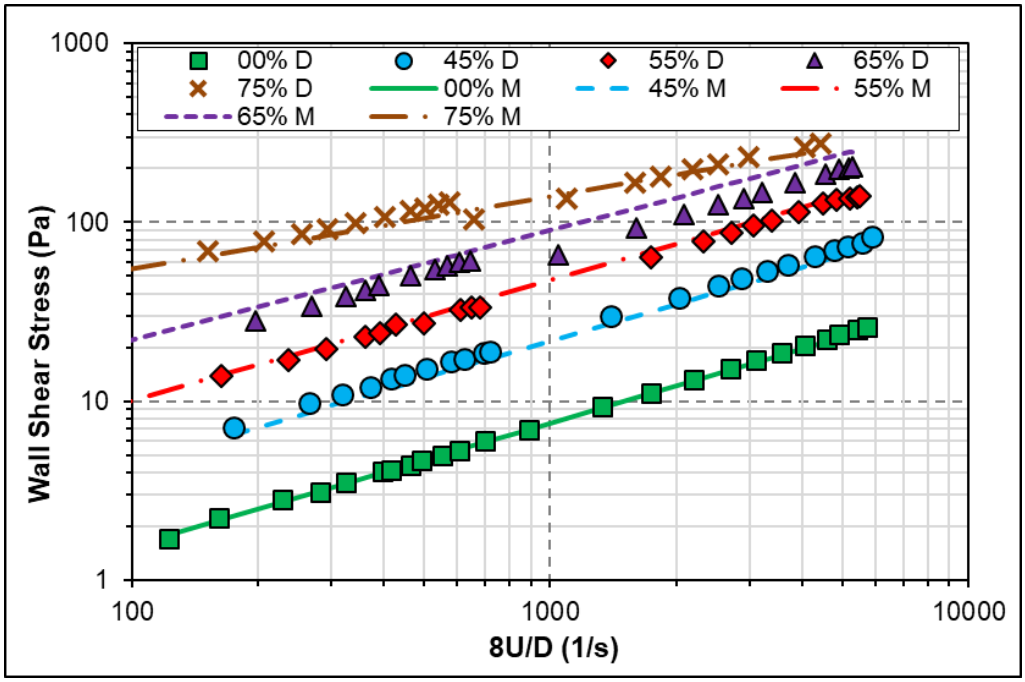

Figure 5.16: Actual data (D) versus Model predictions (M) at 24°C

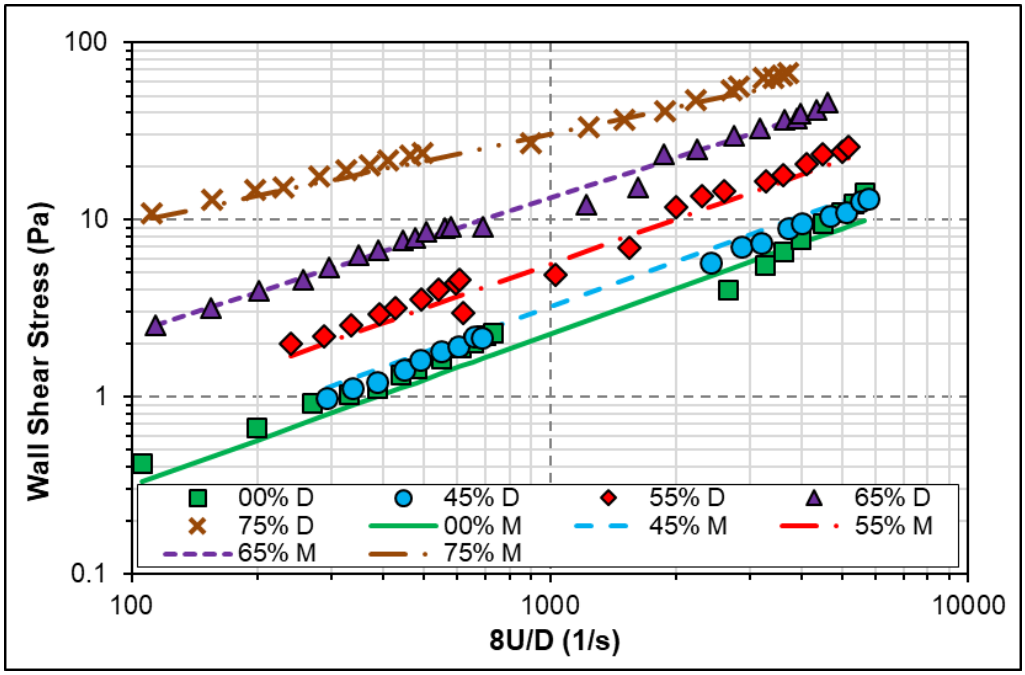

Figure 5.17: Actual data (D) versus Model predictions (M) at 149°C

5.6 Model Sensitivities

The newly developed rheological model has been used to perform a parametric study to quantify the effects of different variables on foam rheology. Based on previous discussions, it is

established that the primary contributor to foam viscosity in high-quality foams is the microscopic bubble structure while the base fluid rheology controls the viscosity of low-quality foams. This can be demonstrated by considering the apparent viscosity plots (Figure 5.18 and 5.19) presented as a function of foam quality at different shear rates and temperatures (24 and 149°C). Even though high-quality foams (qualities greater than 55%) display a reduction in viscosity with temperature, the reduction is not as severe as that of low-quality foams; therefore, the bubble structure is less affected by temperature change than base fluid viscosity. On the other hand, the viscosity of low-quality foams influenced significantly with temperature change.

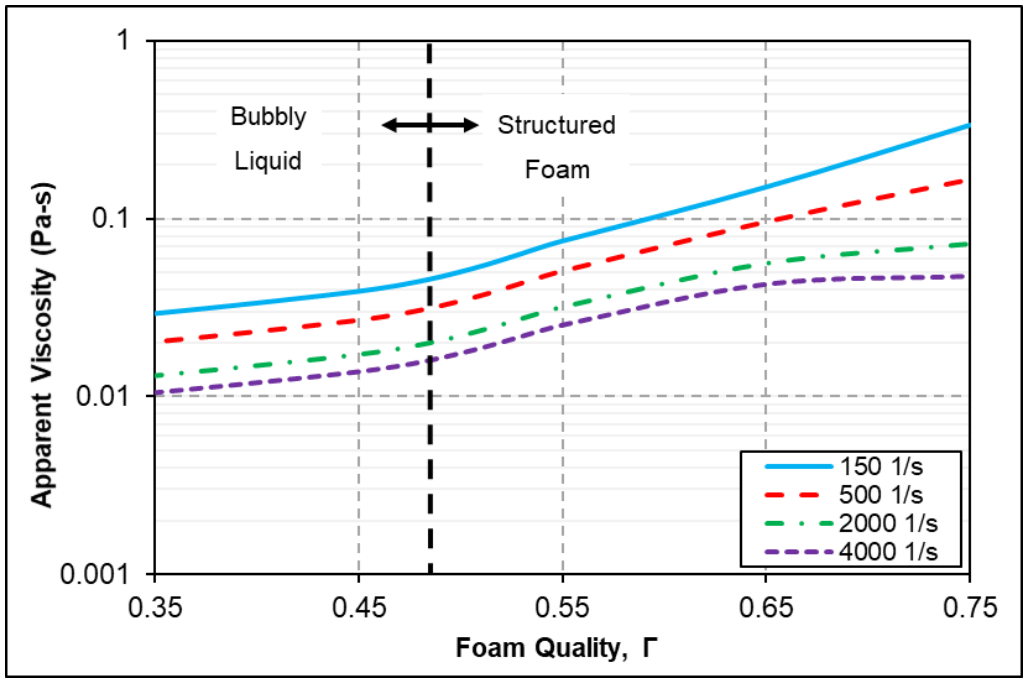

Figure 5.18: Predicted apparent viscosity vs. quality at different shear rates and at 24°C

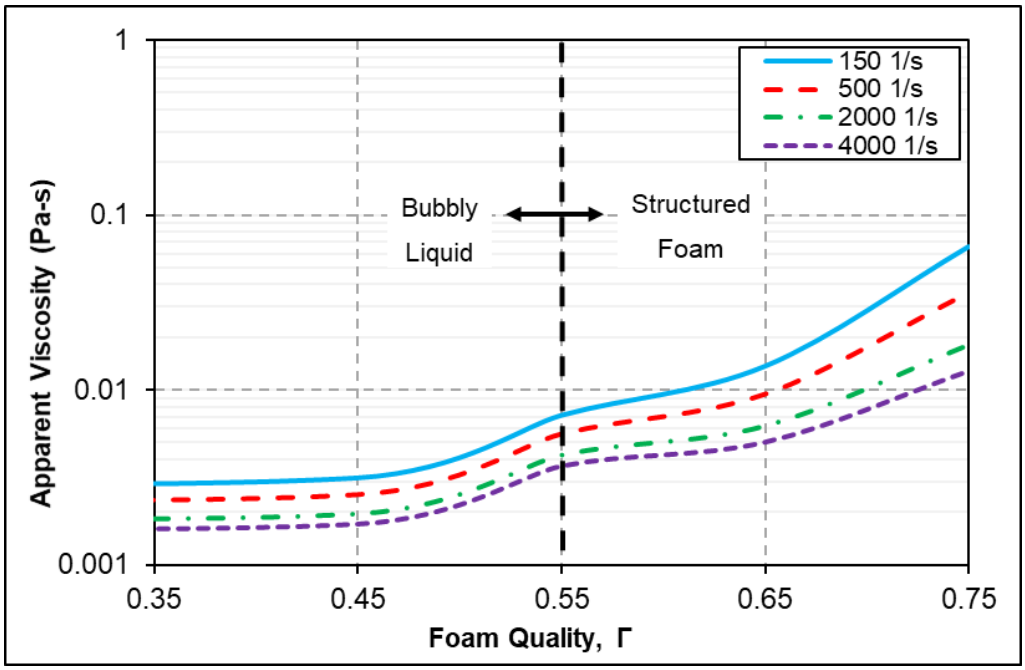

Figure 5.19: Predicted apparent viscosity vs. quality at different shear rates and at 149°C

5.7 Comparison of Experimental Measurements with Existing Models

After performing an extensive literature review, two models (Bonilla and Shah 2000; Harris and Reidenbach 1987) have been identified. The models can predict foam rheology at elevated temperatures. The validity limits of the models are close to the range of experimental variables used in the present study. Therefore, a comparative study is performed to assess the accuracy of the models in reproducing experimental results. The following sections discuss the results of this comparative study.

5.7.1 Comparison with Harris and Reidenbach (1987) Model

Studying guar based foams, Harris and Reidenbach (HR Model) developed correlations that are applicable for a wide range of temperatures (24 – 149ºC). The model predictions closely match (Figure 5.20) the experimental data of low-quality foams (< 55%) obtained at ambient temperature (average error of ~ 29%). However, the model discrepancies increased at elevated temperature (Figure 5.21). This variation in model performance can be attributed to the difference

in base fluid type, surfactant type and concentration, and foam generation technique. Additionally, the model adequately predicts the base fluid properties at all temperatures, except at 149°C, which could be because of the difference in the guar and PAC thermal degradation mechanisms and stability.

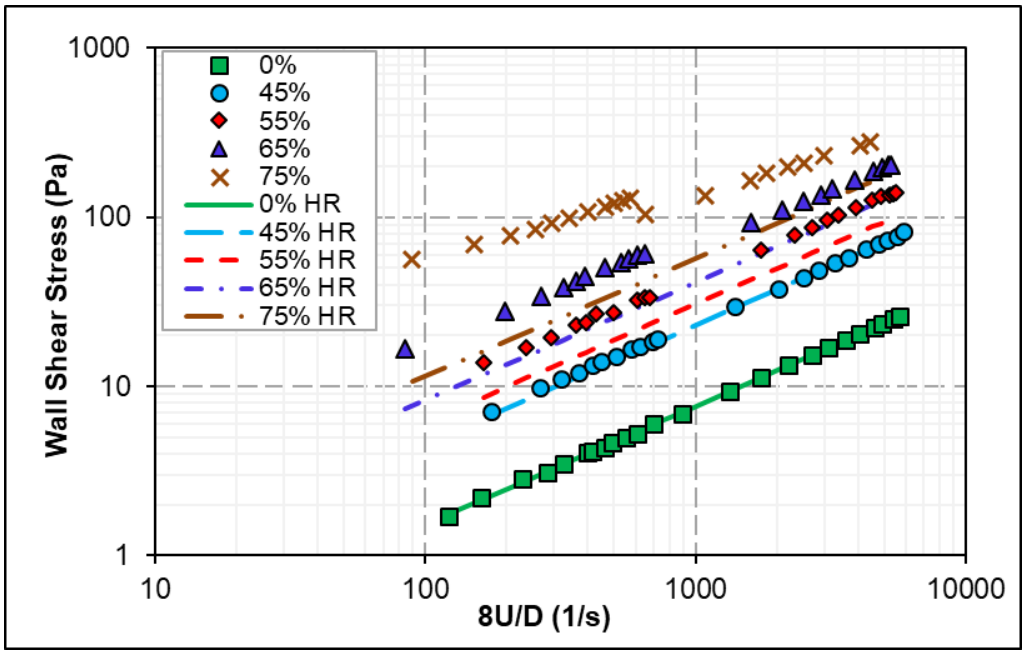

Figure 5.20: Measured and HR Model predicted flow curves at 24°C

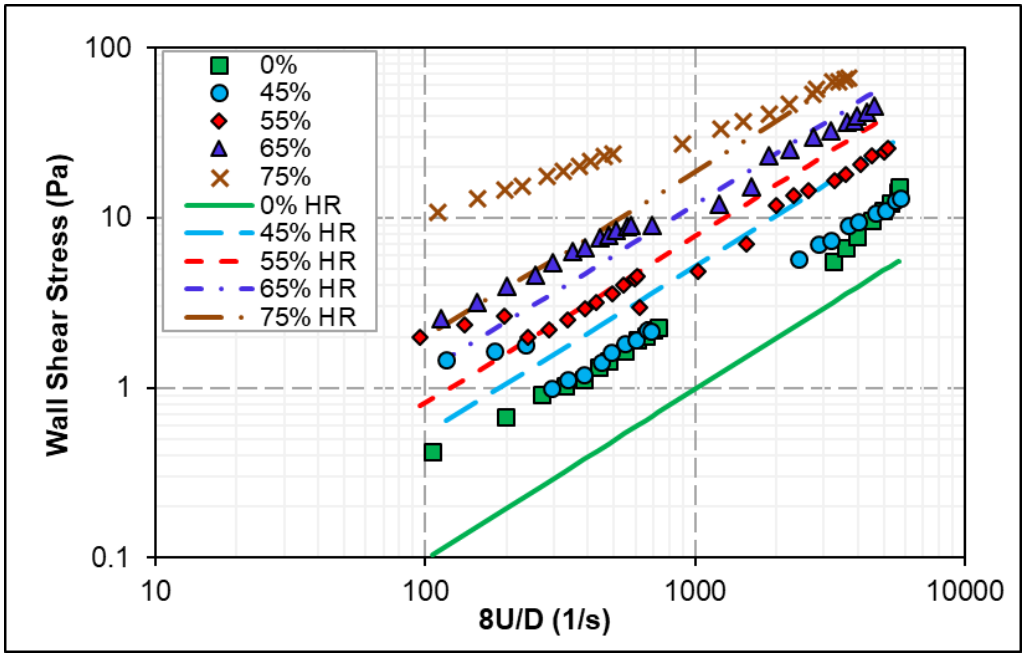

Figure 5.21: Measured and HR Model predicted flow curves at 149°C

5.7.2 Comparison with Bonilla and Shah (2000) Model

Bonilla and Shah (2000) developed an empirical model (BS Model) based on experimental results with guar based stiff foams. At low qualities (< 55%) and temperatures (< 79 °C), the model provides better predictions as compared to the HR model (Figure 5.22). The model is valid in the temperature range of 24 to 79°C. Its accuracy noticeably decreases at elevated temperature due to discrepancies resulting from extrapolation (Figure 5.23). Furthermore, differences in the test conditions add to the uncertainty in the predictions of the model. The BS model is developed on measurements obtained from experiments conducted using lower surfactant concentrations (0.5% v/v) as compared to the present study. Also, the foams were not regenerate between consecutive measurements to restore the microscopic bubble structure and distribution, and subsequently foam rheology.

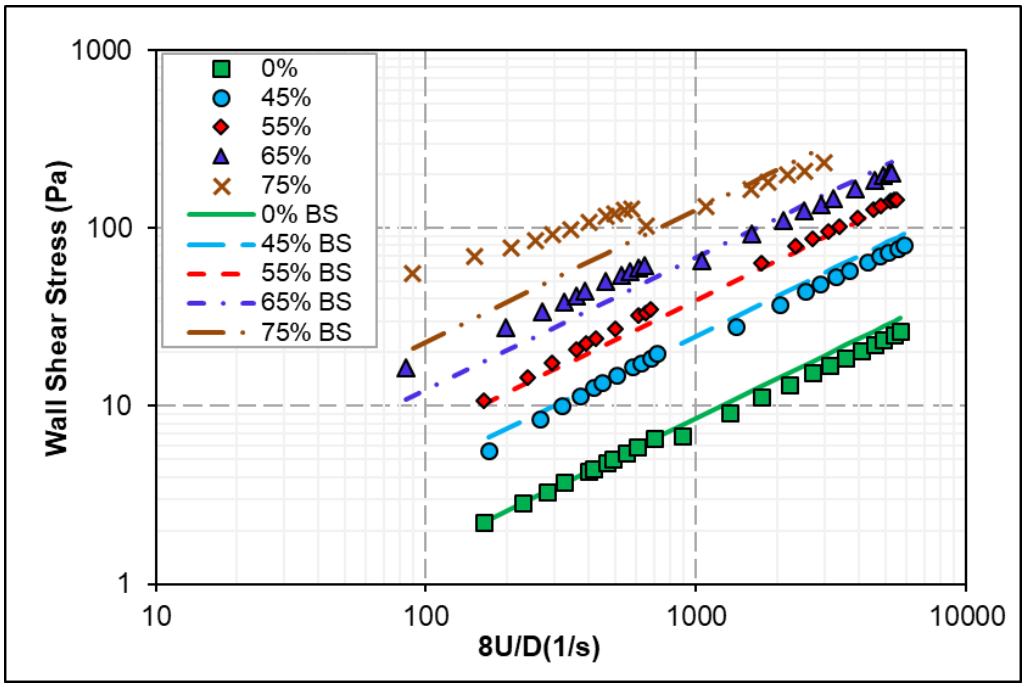

Figure 5.22: Measured and BS Model predicted flow curves at 24°C

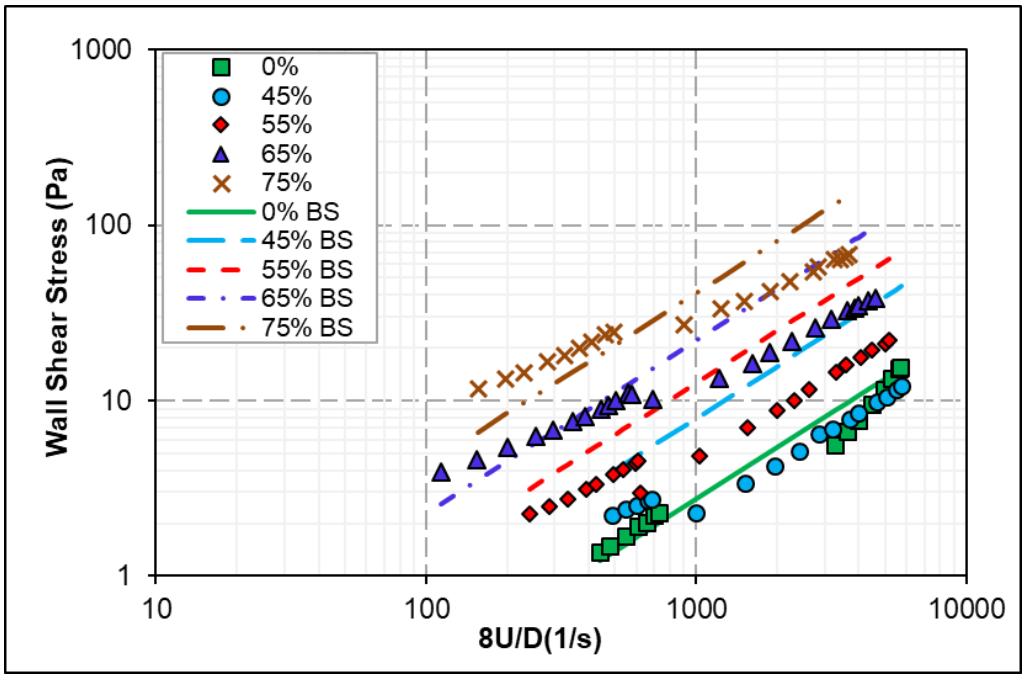

Figure 5.23: Measured and BS Model predicted flow curves at 149°C

5.8 Annular Pressure Prediction

To determine the bottom hole pressure in underbalanced foam drilling operations, an accurate hydraulic model is required to predict the annular pressure loss. In the present study, a

hydraulic model (Ahmed, 2005; Ahmed *et al.*, 2006) developed for yield power-law fluid is used to reproduce measurements obtained from the annular test section. Since the rheologies of foams best fit the power-law model, the yield stress term is equated to "0" in the hydraulic model. During field applications, foam density changes throughout the wellbore due to its compressibility; however, in the present study, the system pressure (6.89 MPa) was maintained high as compared to the pressure drop (Maximum 0.3 MPa) in the test section. Hence, any variation in density due to frictional drag was assumed to be negligible. Furthermore, the differential pressure ports were located at 50 times the internal diameter away from the ends; therefore, the flow is considered to be fully developed. Other model assumptions include no wall slip and isothermal laminar flow condition. The hydraulic model uses geometric parameters (Kozicki and Tiu, 1986), which are applicable for eccentric annular flow under laminar condition. The model is valid for a wide range of fluid behavior index (0.2 to 1.0), eccentricities (0 to 95%) and the diameter ratios (0.2 to 0.8). The average shear rate for a power-law fluid flowing in an eccentric annulus can be expressed as follows:

$$\bar{\dot{\gamma}}_w = a\bar{\tau}_w \frac{d\left(\frac{8U}{D_h}\right)}{d\bar{\tau}_w} + b\left(\frac{8U}{D_h}\right) = \left[\frac{a}{n} + b\right]\left(\frac{8U}{D_h}\right) \tag{5.5}$$

where U is the flow velocity in the annulus; $8U/D_h$ is the nominal Newtonian shear rate; $D_h = (D_o - D_i)$ is the hydraulic diameter of the annulus; and n is the fluid behavior index.

The correlations for the geometric parameters (a and b) are presented (Appendix II) in terms of dimensionless eccentricity ($e = \delta/[R_o - R_i]$), where, δ is the offset distance between centers) and diameter ratio ($\kappa = D_i/D_o$). The correlations have been developed by applying regression analysis on the results of analytical (Piercy *et al.*, 1933) and numerical solutions (Escudier *et al.*, 2002; Fang *et al.*, 1999). After obtaining the average shear rate from Eq. (5.5), the

constitutive equation of power-law model parameters is applied to determine the average wall shear stress as: $\bar{\tau}_w = K_F \bar{\dot{\gamma}}_w^{\,n_F}$. The Reynolds number in annular flow is calculated as $Re = 8\rho U^2/\bar{\tau}_w$ to verify the establishment of laminar flow condition ($Re \leq 2100$) in the annulus. Then, the friction pressure gradient is evaluated as follows:

$$\left(\frac{\Delta P}{\Delta L}\right)_f = 4\frac{\bar{\tau}_w}{D_h} \tag{5.6}$$

where, $\left(\frac{\Delta P}{\Delta L}\right)_f$ = friction pressure gradient in the annulus.

Figure 5.24 and Figure 5.25 compares predicted and observed annular pressure losses at 24ºC and 149ºC respectively. During the design and construction of the annular test section, efforts were made to create a nearly eccentric (approximately 95%) annular geometry. Model predictions and measurements demonstrate reasonable agreement at low temperature (24ºC). However, discrepancies steadily increase with temperature. The disagreement could be due to foam instability, which is detected by the quick reduction of pressure loss measurements during high-temperature experiments. The instability can cause the foam to segregate into two fluid layers: high-quality upper layer and low-quality lower layer. Due to narrow clearance, the lower layer is more or less stagnant, and the flow is mostly in the upper layer which is occupied by high-quality foam. As a result, the pressure loss increases as the foam in the upper layer becomes very dry due to the drainage, which is exacerbated because of increased temperature. Hence, the model under-predicts the measurements. The average deviation increases from 16 to 53 percent when the temperature is raised from 24 to 149ºC. Overall, it gives reasonable predictions for base fluid, except at high temperature (149ºC).

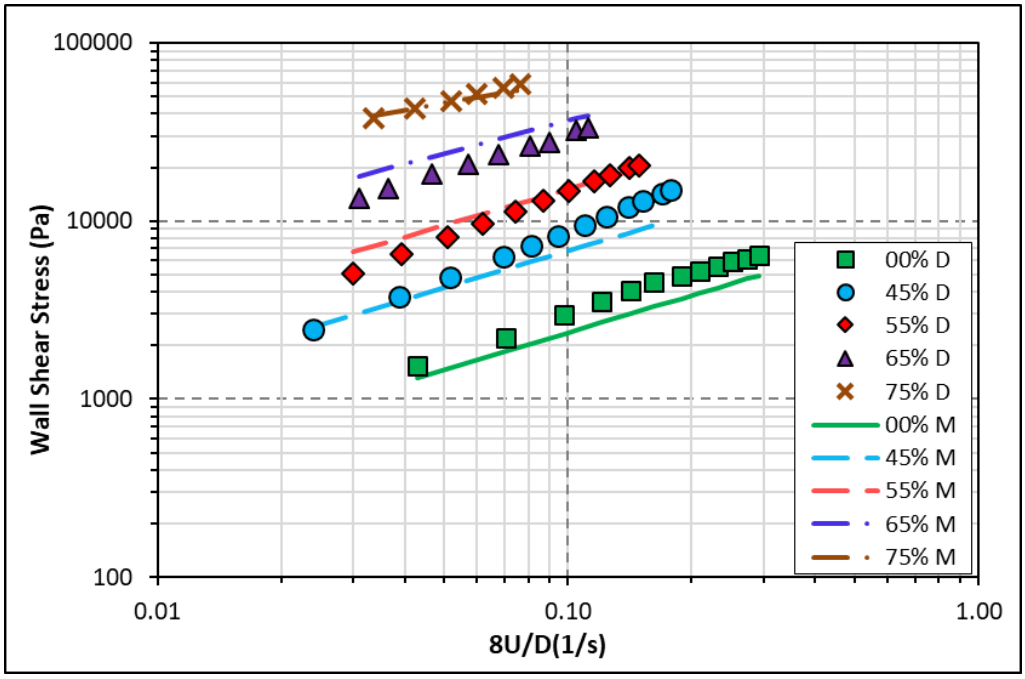

Figure 5.24: Measured and Model predicted wall shear stress at 24°C

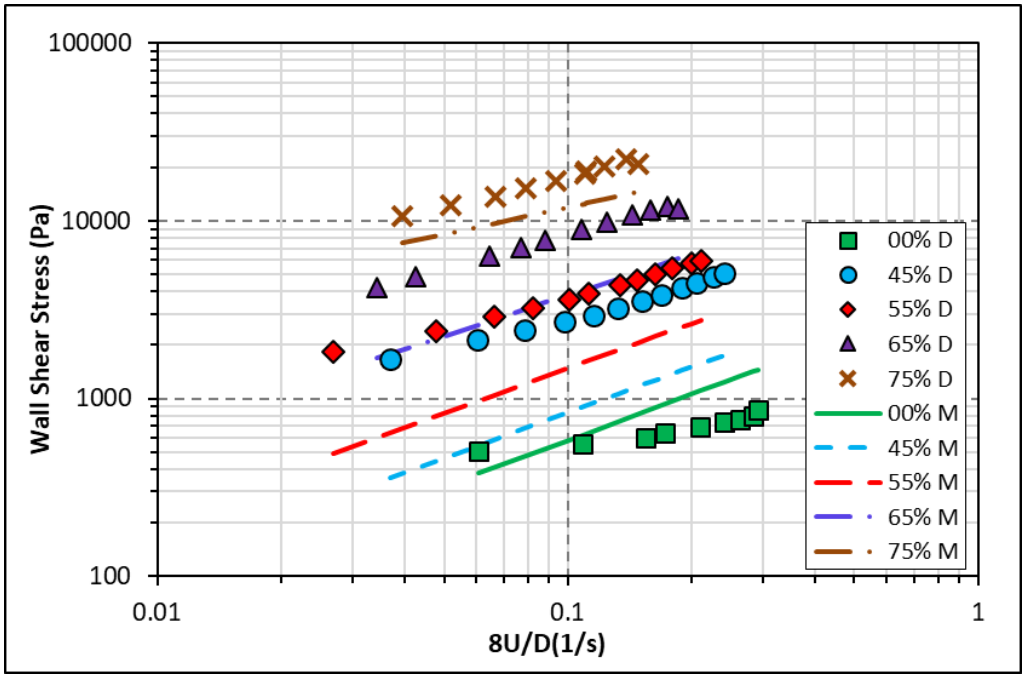

Figure 5.25: Measured and Model predicted wall shear stress at 149°C

Chapter 6

Modeling of Foam Drilling Hydraulics in Wellbore

Modern foam drilling operations have been used in the United States since the 1950's. Foam drilling operations use stable foam (foam qualities between 0.6 to 0.98) for an effective well cleanout (Lyons *et al.*, 2009). At low qualities, foam separates into its constituent phases and at higher qualities, it behaves as a mist and loses its rheological properties. Furthermore, owing to its complex structure and compressibility, foam rheology changes significantly with foam quality, pressure, temperature, surfactant type, and its properties, base fluid properties, flow geometry, and interfacial properties which affects the foam decay rate (Heller and Kuntamukkula, 1987). This makes predicting bottom hole pressure, foam flow velocity, foam density and foam quality during foam drilling operations both very challenging and critically essential. Engineers and drilling supervisory personnel need to make predictive calculations for efficient and cost-effective drilling operations. A comprehensive computer program was developed to predict the BHP by employing different controllable variables for an optimized foam drilling operation.

The mathematical model involves solving the equation of motion and steady-state mechanical energy balance equation for a discretized wellbore geometry (Ahmed *et al.*, 2003b; Chen, 2005). A Eulerian approach was used to define the control volume, and foam was assumed to behave as a continuum fluid. Additionally, the flow was considered in the axial direction with a constant temperature gradient along the wellbore. The wellbore itself comprised of vertical, inclined and horizontal sections and the effect of drilled cuttings on the annular friction pressure as well as hydrostatic was considered in the hydraulic model. The power-law fluid rheology model developed in the study was used as the foam rheology model (Section 5.4).

6.1 Hydraulic Model Formulation

As mentioned earlier, the equation of motion and mechanical energy balance (MEB) was applied to a discretized wellbore geometry. Figure 6.1 shows the cross-sectional area of an inclined pipe where the foam flow is assumed to take place along the downward axial direction through a pipe and upward direction through the annulus. The control volume has a length "dL" with velocity and pressure changing from element "i" to "$i + 1$".

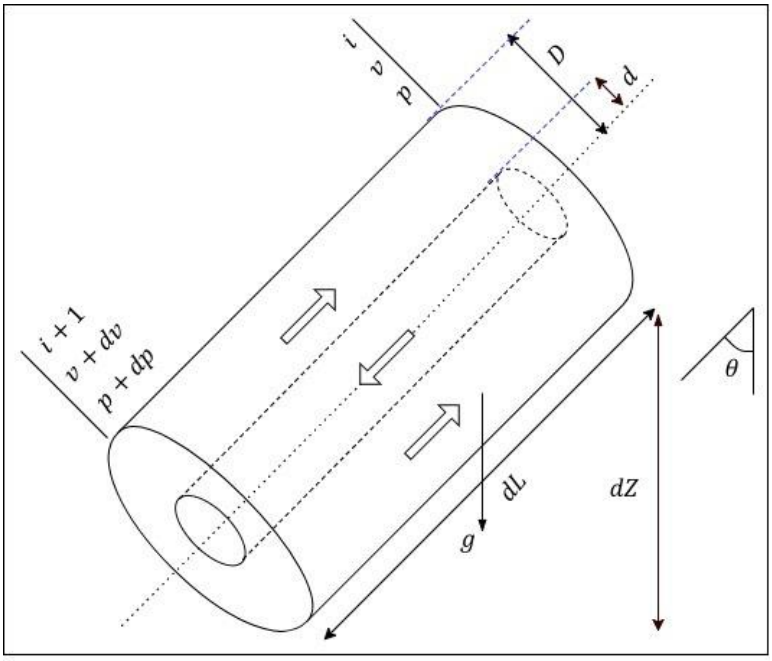

Figure 6.1: Schematic of a small control volume

6.1.1 Density and Equation of State for Foam

The EOS for foam used in the present study is described in Appendix III. The real gas equation is used to determine the density of Nitrogen as:

$$\rho_G = PM/ZRT \tag{6.1}$$

where, ρ_G is gas density; P is pressure; T is temperature; Z is real gas compressibility; M is molecular weight of gas; R is the universal gas constant. The foam density is calculated using the in-situ foam quality and is given as,

$$\rho_F = \Gamma\rho_G + (1-\Gamma)\rho_L + C_s\rho_s = \Gamma\frac{PM}{ZRT} + (1-\Gamma)\rho_L + C_s\rho_s \tag{6.2}$$

where, ρ_F is foam density; ρ_L is base liquid density; ρ_s is solids density; Γ is foam quality; C_s is solids concentration and is given by Eq (6.2) and its value equals "0" for flow inside drill string. For hydraulics calculations, an average of the foam densities at points "i" and "$i+1$" is calculated and is assumed to be constant over the segment length.

6.1.2 Foam Rheology

High foam viscosity results in greater frictional pressure losses as compared to conventional drilling fluids. For precise hydraulic predictions, an accurate rheological model is needed. Foam is assumed to behave like a power-law fluid, and the fluid rheological parameters were calculated using the empirical correlations (Eq. 5.4) developed by analyzing actual measurements from the foam flow experiments in the present study. The detailed description of the foam rheology model is discussed in section 5.4. The rheological models developed in the study are valid for foam qualities lower than 75%. It should be noted that, during drilling operations foam qualities decreases with depth, therefore, at greater well depths, where temperatures are higher, rheological predictions are performed using the new correlations, which account for the effect of temperature.

At shallower depths where the temperatures are lower, foam quality is higher (>75%), and the foam structure and its rheology remain fairly intact, the rheological parameters are predicted using Chen's (2005) model for HEC based polymeric foams.

$$n_F = -0.45\Gamma + 0.7633 \tag{6.3}$$

$$\frac{K_F}{\mu_L} = exp(a.\Gamma^2 + b.\Gamma + c) \tag{6.4a}$$

where, a, b, and c are given as,

$$a = (-0.533{\mu_L}^2 + 3.6735\mu_L - 13.546) \tag{6.4b}$$

$$b = (0.8926{\mu_L}^2 - 6.5877\mu_L + 29.966) \tag{6.4c}$$

$$c = (-0.3435{\mu_L}^2 + 2.5273\mu_L - 14.218) \tag{6.4d}$$

where, $\mu_L =$ base liquid viscosity at 300 s^{-1} in cP. The correlations are valid when the base liquid viscosity remains within 1 to 8.1 cP range.

6.1.3 Mechanical Energy Balance Equations

After performing the mechanical energy balance over the control volume for compressible flow (Appendix III), the final expression for total pressure drop is given as:

$$\frac{dp}{\rho} + \frac{udu}{g_c} = -\left[\frac{g}{g_c}cos\theta + \frac{2fu^2}{g_c d}\right]dL \tag{6.5}$$

where, $\rho =$ foam density; $u =$ foam velocity; $f =$ Fanning friction factor; $g_c =$ conversion factor; $\theta =$ inclination angle.

The first term on the left-hand side of the equation indicates the total pressure drop, while, the second term represents the acceleration pressure drop. The first and the second terms on the right-hand side show the pressure drop due to hydrostatic head and frictional pressure drop respectively. The gravitational acceleration is negative for downward flow. Eq. (6.5) is applicable

for the small segment of length, "dL" for which the density is assumed constant. The value of the Fanning friction factor, "f" varies along the length of the pipe and since, there is no direct relation between the two, Eq. (6.5) cannot be integrated directly over the entire length of the wellbore. Therefore, the mechanical energy equation is discretized and solved numerically. The discretized form of mechanical energy balance equation is given as:

$$2\frac{p_{i+1}-p_i}{\rho_{i+1}+\rho_i}+\frac{u_{i+1}^2-u_i^2}{2g_c}=-\left[\frac{g}{g_c}cos\theta+\frac{f(u_{i+1}+u_i)^2}{g_c D_h}\right](L_{i+1}-L_i) \tag{6.6}$$

where index "i" refers to the element number; D_h = hydraulic diameter.

Equation (6.6) can be solved iteratively for p_{i+1}. Terms ρ_{i+1} and u_{i+1} are calculated at downstream of the control volume and therefore, their variation with respect to p_{i+1} is needed. These relations are obtained by using the material balance of gas and liquid phases and from the equation of state and are discussed in detail in Appendix III.

6.1.4 Closure Equations

The generalized Reynolds number for the control volume was calculated using the averaged values of the parameters,

$$Re\approx\frac{(\rho_{i+1}+\rho_i)[0.5(u_{i+1}+u_i)]^{2-[0.5(n_i+n_{i+1})]}D_h{}^{[0.5(n_i+n_{i+1})]}}{(K_{i+1}+K_i)8^{[0.5(n_i+n_{i+1})]-1}} \tag{6.7}$$

Fanning friction factors for foam flow in the wellbore for the laminar flow regime ($Re<2100$) was calculated using empirical correlations developed by Deshpande and Barigou (2000) for a pseudoplastic fluid,

$$f=\frac{18.36}{Re^{0.97}} \tag{6.8}$$

where Re = generalized Reynolds number.

For a turbulent flow of non-Newtonian foam in the wellbore ($Re > 2100$), an iterative solution for Fanning friction factor proposed by Szilas *et al.* (1981), was used, which accounts for the roughness in the wellbore and tubular.

$$f = \left\{-2.log_{10}\left[\frac{\epsilon_{av}}{3.7D_h} + \frac{6.9^{-\chi/2}}{Re.f^{(2-n)/2n}}\right]\right\}^{-2} \tag{6.9}$$

where, $\chi = 1.51^{1/n}\left[\frac{0.707}{n} + 2.12\right] - \frac{4.015}{n} - 1.057$; $D_h =$ hydraulic radius; $\epsilon_{av} =$ average absolute roughness of the surfaces in the control volume. In case of foam flow through the drill pipe and cased annulus sections, all steel surfaces are assumed to have an absolute roughness of "$\epsilon_{av} = 0.0002$ m". For foam flow in the open-hole section of the annulus, approximate average roughness is calculated as (Lyons *et al.*, 2009):

$$\epsilon_{av} = \frac{\epsilon_{OH}{D_{OH}}^2 + \epsilon_{DP}{D_{DP}}^2}{{D_{OH}}^2 + {D_{DP}}^2} \tag{6.10}$$

where, $\epsilon_{OH} =$ absolute roughness of openhole = 0.003 m; $D_{OH} =$ openhole internal diameter; $\epsilon_{DP} =$ absolute roughness of steel pipe = 0.0002 m; $D_{DP} =$ outer diameter of drill pipe.

Okpobiri and Ikoku (1983) concluded that the cuttings and mud suspension friction factor can be assumed to be a sum of individual friction factors for the fluid and the drilled solids. Therefore, with an increase in the concentration of drilled solids at fixed Reynolds number of the foam, the friction pressure drop increases. In the present investigation, solids friction factor correlation calculated using Okpobiri and Ikoku (1986) empirical relation developed for foam and mist drilling was used.

$$f_s = \frac{39.36}{Re^{0.9907}} \left\{ \frac{[0.5(\rho_{i+1} + \rho_i)]^2}{g d_s} \right\}^{0.0296} \left\{ \frac{\rho_s}{0.5(\rho_{i+1} + \rho_i)} \right\}^{0.1403} C_s^{0.3844} \quad (6.11)$$

where, d_s = cuttings diameter; ρ_s = cuttings density; C_s = cuttings concentration and is calculated for each segment using the following equation,

$$C_s = \frac{(1 - \phi) \cdot D_{OH}^2 \cdot ROP}{4 Q_F} \quad (6.12)$$

where, $\phi =$ formation porosity; $D_{OH} =$ openhole diameter; $ROP =$ rate of penetration; $Q_F =$ volumetric foam flow rate.

6.1.5 Wellbore Configuration

For the purposes of developing a computer program to simulate foam drilling hydraulics, a three-segment wellbore, similar to one proposed by Chen (2005) was assumed (Figure 6.2). The X-axis indicates the horizontal direction, while, Y-axis indicates the vertical direction. The wellbore consists of a vertical, inclined, and horizontal sections; part of the wellbore is cased, and the drill bit is drilling through an open hole section. The foam flows from the drill pipe, through the bit and comes out of the annulus, where the back pressure is P_2. At the end of the control volume of length, ΔL_1, the pressure is P_1. For flow inside the drill string, the upstream and the downstream pressures are denoted as P_{2P} and P_{1P} respectively.

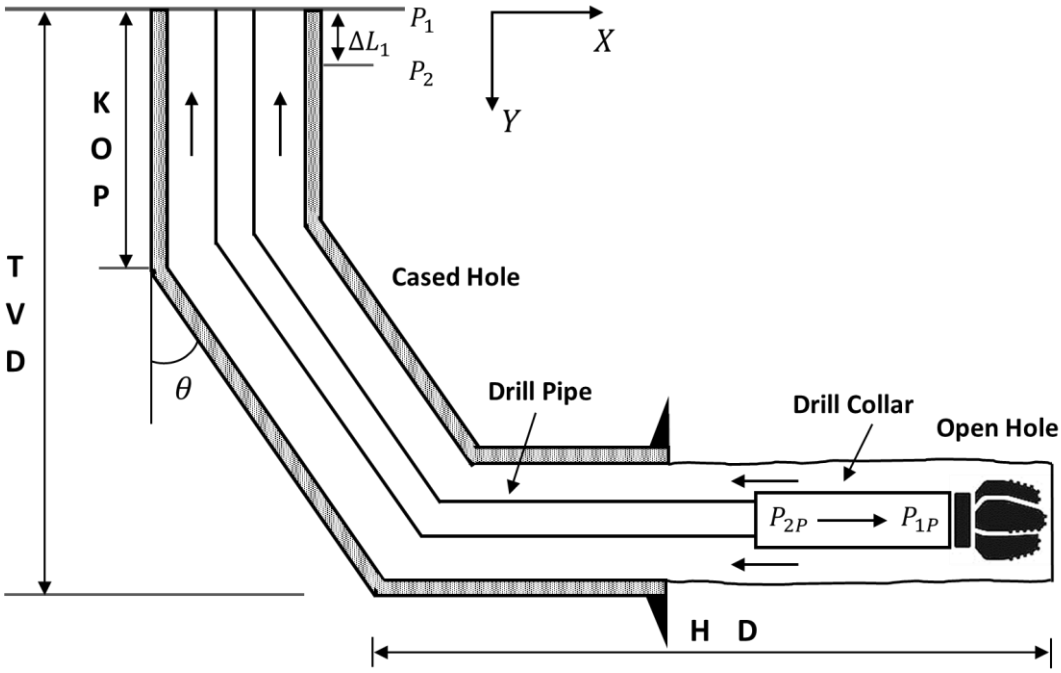

Figure 6.2: Foam flow through the pipe and annular sections during drilling

Flow-Through Drill String: Applying the discretized MEB equation (Eq. 6.6), for downward flow of foam in the drill string, the pressure at downstream point, "P_{2P}" is given as,

$$P_{2P} = P_{1P} + \left[-\frac{g\bar{\rho}}{g_c} cos\,\theta + \frac{f\bar{\rho}(u_{1P} + u_{2P})^2}{2g_c D_h}\right]\Delta L - \frac{\bar{\rho}(u_{1P}^2 - u_{2P}^2)}{2g_c} \tag{6.13}$$

where, $\bar{\rho}$ = average foam density. The MEB is integrated between two neighboring points "2" and "1" upstream and downstream of the direction of flow in the drill string.

Flow-Through Annulus: Similarly, for upward flow through the annulus, applying the discretized MEB equation, pressure at downstream point " P_{2P}" is expressed as,

$$P_2 = P_1 + \left[\frac{g\bar{\rho}}{g_c} cos\,\theta + \frac{f\bar{\rho}(u_2 + u_1)^2}{2g_c D_h}\right]\Delta L - \frac{\bar{\rho}(u_2^2 - u_1^2)}{2g_c} \tag{6.14}$$

where, the MEB equation is integrated between the two neighboring points in the annulus.

6.1.6 Pressure Drop Across Drill Bit

Figure 6.3 shows the schematic of a drill bit and the foam flowing across the bit. Pressure drop was calculated using the equations proposed by (Okpobiri, 1982). The Eqs. (6.15) to (6.18) are solved iteratively for bit pressure drop, ΔP_{bit}.

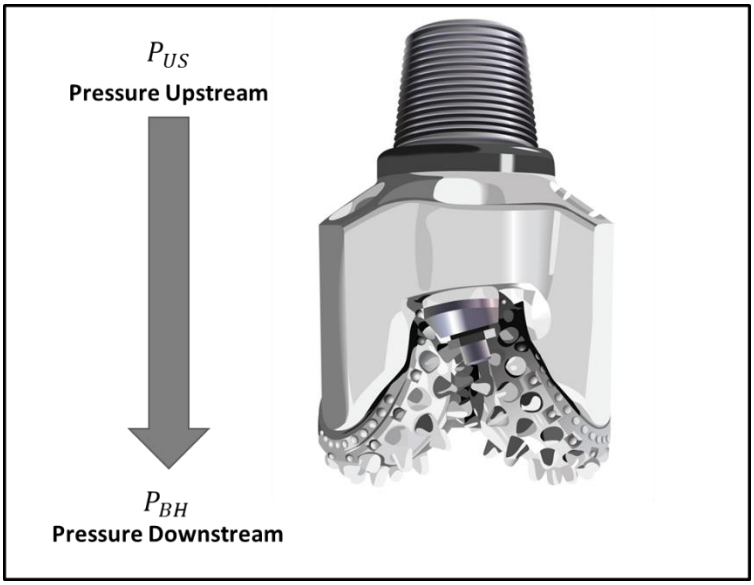

Figure 6.3: Schematic for Pressure Drop Across the Drill Bit

$$P_{BH} = P_{US} \cdot exp\left(\frac{B\Delta P_{bit}}{A} - E \cdot u_n^2\right) \tag{6.15}$$

where, u_n = average foam velocity through the nozzle; ΔP_{bit} = Pressure drop across the bit.

$$A = \frac{\dot{m}_G}{(\dot{m}_G + \dot{m}_L)} \cdot \frac{ZRT}{M} \tag{6.16}$$

$$E = \frac{1}{2.A.g_c} \tag{6.17}$$

$$B = \frac{\dot{m}_G}{\rho_L(\dot{m}_G + \dot{m}_L)} \tag{6.18}$$

where, $\dot{m}_G$ = mass flow rate of gas; $\dot{m}_L$ = mass flow rate of liquid; g_c = conversion constant 1 (kg-m)/(N-s^2).

The average flow velocity across the drill bit nozzles, u_n, is calculated using at equivalent nozzle diameter, $D_{n_{eq}}$,

$$D_{n_{eq}} = (n_n \cdot D_n)^{0.5} \tag{6.19}$$

where, n_n = number of nozzles on the bit and D_n = diameter of each nozzle. The average foam velocity is calculated as,

$$u_n = \frac{Q_F}{\left(\pi {D_{n_{eq}}}^2/4\right)} \tag{6.20}$$

where, Q_F = the foam flowing across the drill bit.

6.2 Calculation Procedure

A typical wellbore profile includes the vertical, buildup and horizontal sections. The hydraulic calculations were performed separately for each section. The calculation starts at the top of the annulus where the foam quality is monitored, and relevant back pressure is maintained. The flow conditions at the top of the annulus at given back pressure, surface temperature, gas, and liquid injection rates are calculated. Using these as the initial conditions at point "1" (Figure 6.2), the pressure at point "2" is calculated using Eq. (6.14). Foam density, velocity, rheology, are re-calculated at the updated value of pressure and the steps are repeated till pressure values converge. The pressure at the top of the next grid is set equal to pressure value at point "2" and the calculation moves on through the vertical, inclined and horizontal section till the wellbore measured depth is reached. The pressure drop across the drill bit is calculated iteratively using bottom hole pressure in the annulus as bit downstream pressure and with an assumed value of drill bit pressure drop (ΔP_{bit}). The calculation then moves into the drill string with the pressure just upstream of the drill bit, point "P_{1P}" (Figure 6.2) as the initial condition. The pressure at the top of the grid (point "P_{2P}")

is calculated using Eq. (6.13). Flow conditions at the point "P_{2P}" are updated at the new pressure value. The steps are repeated until the pressure values converge. The calculation moves upward and reaches the top of the drill string, i.e. the standpipe.

For implementing the hydraulic model, MATLAB® simulation software was used. It is a matrix-based calculation language that provides a rigorous and fast way of analyzing large data with easy quality-checking and code-debugging capabilities. A detailed step by step procedure is provided in Appendix IV.

6.3 Sample Simulation Cases

The calculations are performed first for the annulus section, followed by calculation of pressure across drill bit, and finally in the drill string. A parametric study was performed using the foam hydraulics simulator by changing the operational parameters such as desired foam quality at top of annulus section, liquid injection rate, gas injection rate, back pressure, geothermal gradient, rate of penetration, and for different wellbore configuration, i.e., a vertical and a three segment wellbore.

As presented in Table 6-1, a vertical and three segment uniform wellbore configurations were considered for the present investigation. The wellbore consists of a $7^{7}/_{8}$-in. (200 mm) open hole section drilled below an API $8^{5}/_{8}$-in. (219 mm, 201.2 mm ID) the intermediate casing which is set at depth of 2134 m (7000 ft). The measured depth in both cases is 3048 m (10000 ft), while, the TVD for the three-segment wellbore is nearly 1560 m (5119 ft). The drill string configurations are the same in both cases, comprising of a 3048 m (10,000 ft) long, API $4^{1}/_{2}$-in. (114 mm, 92.46 mm ID) drill pipe. For simplicity, no drill collars were not considered as a part of the drill string.

Table 6-1: Vertical and Three Segment Wellbore Configurations

Wellbore Type	Section Type	MD (m)	Inc. Angle (deg.)	Annulus Section: ID (in.) / Length (m)		Drill String: OD (in.) / Length (m)	
				Open hole	Inner Casing	Drill pipe	Drill Collars
Vertical	Vertical	3048	0	8.5 / 914	8.625 / 2134	4.5 / 3048	-
Three Segment	Vertical	914	0	8.5 / -	8.625 / 914	4.5 / 914	-
	Inclined	914	45	8.5 / -	8.625 / 914	4.5 / 914	-
	Horizontal	1220	90	8.5 / 914	8.625 / 306	4.5 / 1220	-

For the base case simulations, regular field foam drilling gas and liquid injection rates were assumed. The formation was assumed to be comprised of sandstone limestone sedimentary rock with an average rock cutting specific gravity of 2.7 and porosity of 0.2. The temperature was assumed to increase linearly based on a constant geothermal gradient of 18 °C/km. Additional input parameters are provided in Table 6-2.

Table 6-2: Input Data for Hydraulic Simulation

Input Parameter	Value (Unit)
Foam Consistency Index, (K_F)	Eqs. (5.4b) and (6.4a)
Foam Flow Behavior Index, (n_F)	Eqs. (5.4) and (6.3)
Yield Point of Fluid, (τ_Y)	0 (Pa)
Base Fluid Density, (ρ_L)	1000 (kg/m^3)
Gas Molecular Weight, (M)	28 (Kg/Kmol)
Liquid Flowrate, (Q_L)	11.36 m^3/hr (50 gal/min)
Gas Flowrate, (Q_G)	2000 (Sm^3/hr)
Foam Quality Desired at Back Pressure Valve, (Γ_{bp})	0.95
Geothermal Gradient, (ΔT)	18 (°C/km)
Surface Temperature, (T_{bp})	30 (°C)
Surface Back Pressure, (P_{bp})	0.69 MPa (100 psi)
Rate of Penetration, (ROP)	18.3 (m/hr)
Surface roughness (open hole and steel tubing)	0.003 m; 0.0002 m
Formation Porosity, (ϕ)	0.2
Cuttings Specific Gravity, (ρ_s)	2.7
Mean Particle Size, (d_s)	5 (mm)
Drill bit Nozzles	$^{12}/_{32}$, $^{12}/_{32}$, $^{12}/_{32}$ (inch)

6.4 Simulation Results

The simulations were performed for both the vertical and three-segment wellbores for the base input variables. The results are discussed in the following sections for both wellbore configurations.

6.4.1 Vertical Wellbore

Figure 6.4 presents the plot of pressure drop versus measured depth while, Figure 6.5 shows the foam drilling parameters such as pressure gradient, foam quality, velocity and density in the vertical wellbore in the drill string and annulus. The annulus pressure drop at the bottom increases to 18.2 MPa (2645 psi) from 0.69 MPa (100 psi), while the foam quality decreases from 0.96 to 0.51, the foam density increases to 640 kg/m^3 from 48 kg/m^3 and the foam velocity decreases to 0.3 m/s from 4 m/s at the top of annulus upstream of the backpressure valve. Pressure drop across the bit is around 0.25 MPa (~35 psi). The injection pressure required at the top of the drill string is back calculated from pressure at the bottom of the drill string and is used to establish the compressor requirements. Results of the simulation in a vertical wellbore for base case inputs are provided in Appendix V (Table V.2).

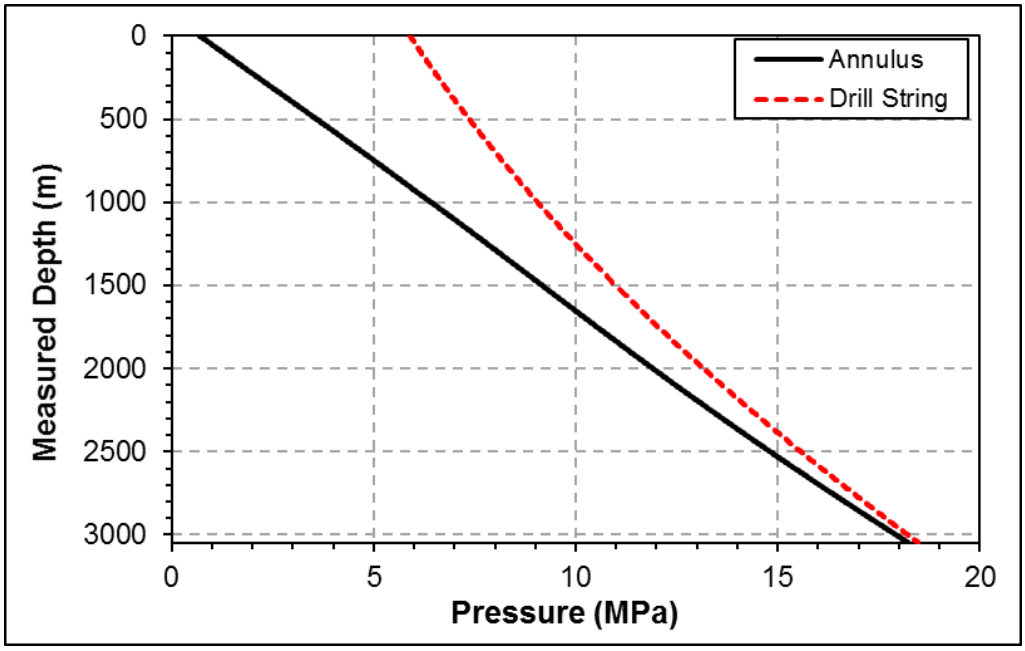

Figure 6.4: Pressure Drop vs. Measured Depth in Vertical Wellbore

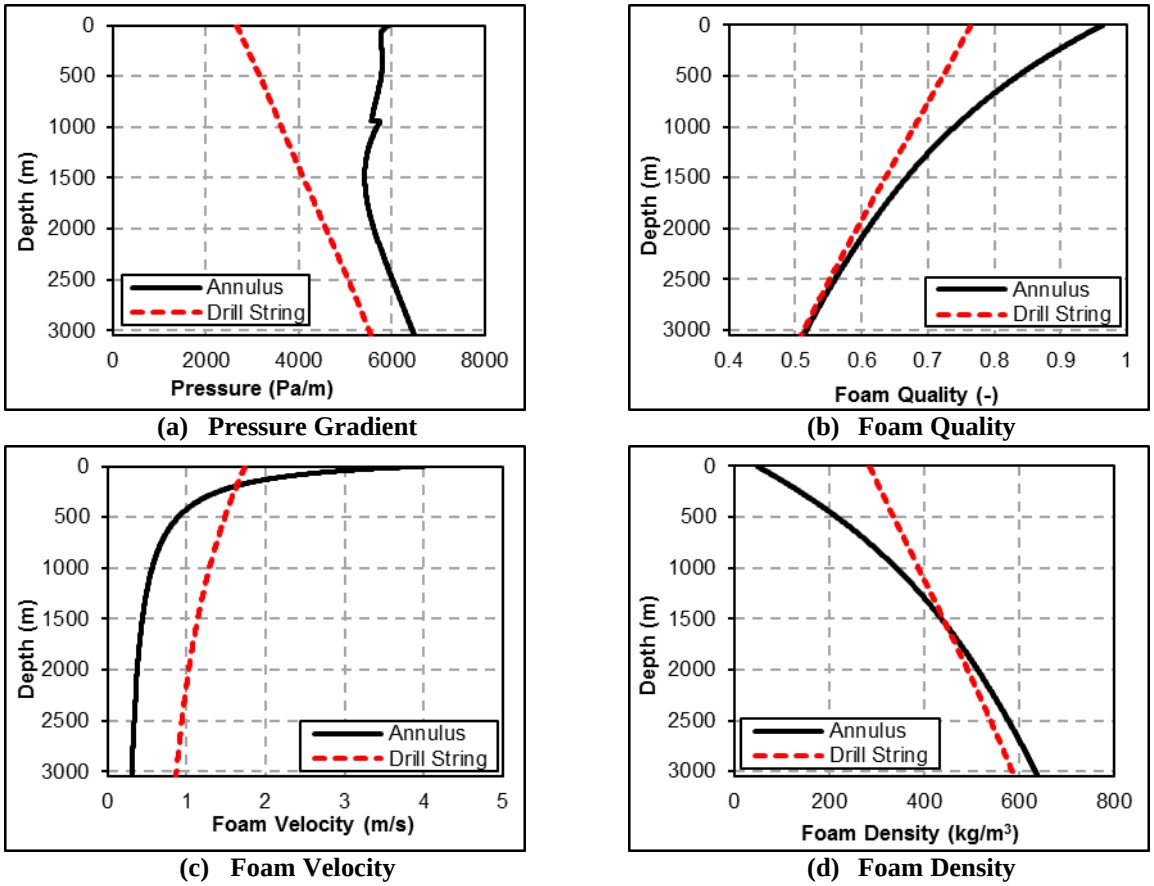

(a) Pressure Gradient **(b) Foam Quality**

(c) Foam Velocity **(d) Foam Density**

Figure 6.5: Foam Drilling Parameters vs. Measured Depth in Vertical Wellbore

From Figure 6.5 (b) and (d) it can be observed that the foam quality and density at the top of the annulus are high and therefore the pressure gradient is mostly friction dominated. Also, the fluid density in annulus is higher as it accounts for the presence of drilled cuttings. With an increase in depth the frictional pressure gradient decreases and the hydrostatic head increases. The sharp change in the annular pressure gradient is a result of varying cross-section across the open hole section (Figure 6.5a). Foam quality, velocity, and density show only gradual changes with respect to measured depth inside the drill string. The friction pressure gradient decreases with depth inside the drill string as well. It should be noted that since the hydrostatic head contributes to pressure at the bottom of the drill string, the injection pressure requirements at top of the drill string are low.

6.4.2 Three Segment Wellbore

Bottom hole pressure in a three-segment wellbore 10.4 MPa (1508 psi) is lower than that observed in the vertical wellbore (Figure 6.6). Additional drilling parameters like foam quality decreases from 0.96 to 0.66, foam density increases to 443 kg/m^3 from 48 kg/m^3 and the foam velocity decreases to 0.44 m/s from 3.97 m/s at the top of annulus upstream of the back-pressure valve (Figure 6.7 b, c, and d). Results of the simulation in a three-segment wellbore for base case inputs are provided in Appendix V (Table V.2).

In the vertical and inclined sections of the wellbore, pressure, foam quality, velocity and density change sharply. Significant expansion occurs in the vertical and inclined sections due to higher gas compressibility and therefore the pressure gradient is high. With increasing inclination, the hydrostatic head is reduced and therefore the pressure and foam properties vary more gradually in the inclined and horizontal sections. In fact, only friction pressure contributes to the total pressure in the horizontal section. Additionally, both foam compressibility and pressure gradients decrease with measured depth resulting in only marginal changes in foam properties, this is due to reduced hydrostatic head. Sudden changes in the annular pressure gradient are attributed to differences in the elevation profile and the cross-sectional areas.

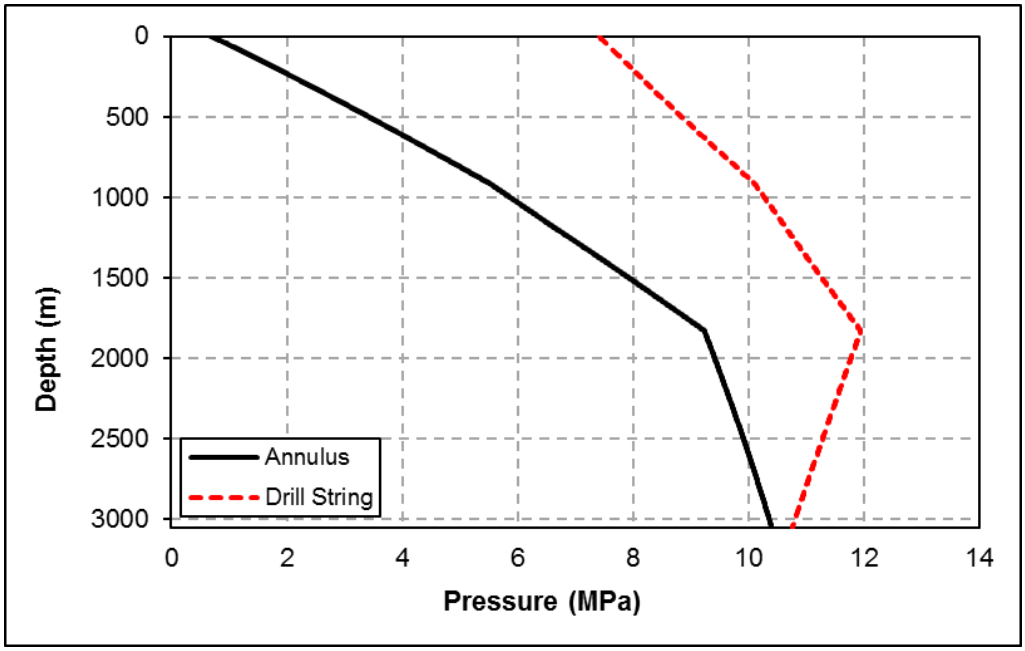

Figure 6.6: Pressure Drop vs. Measured Depth in Three-Segment Wellbore

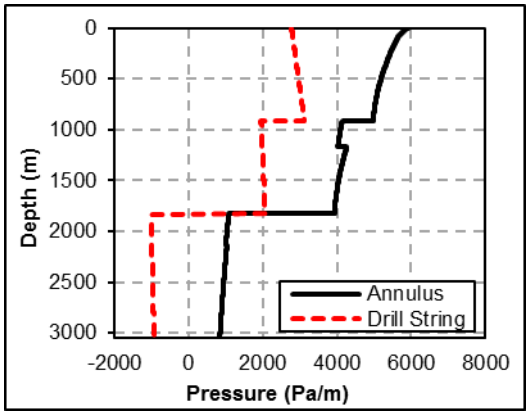

(a) Pressure Gradient

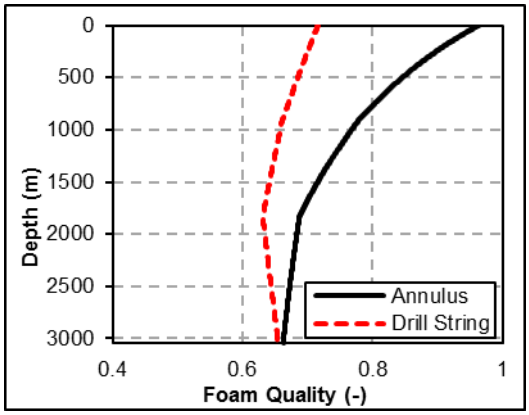

(b) Foam Quality

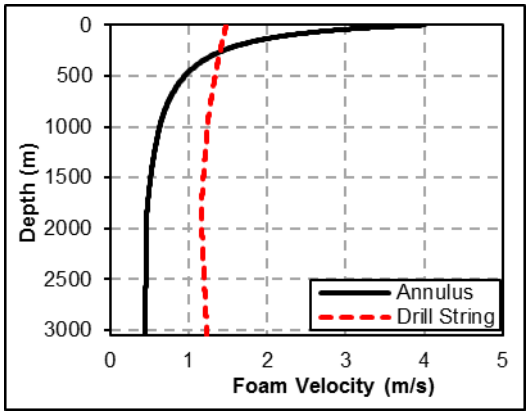

(c) Foam Velocity

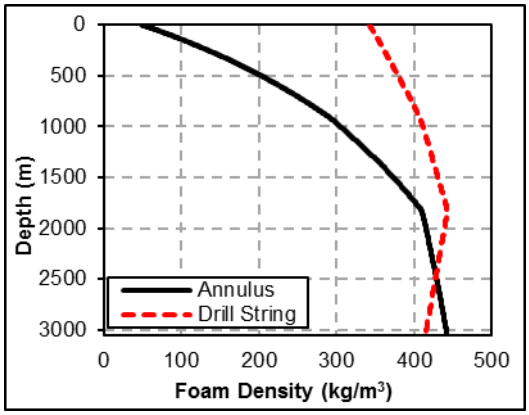

(d) Foam Density

Figure 6.7: Foam Drilling parameters vs. Measured Depth in Three-Segment Wellbore

Inside the drill string, the pressure gradient changes more gradually (Figure 6.7a) along the flow path. Pressure drop is friction dominated in the horizontal section and the hydrostatic gradient dominates in the vertical and inclined sections. Moreover, loss in hydrostatic moving up the drill string is lower as compared to a vertical wellbore. This results in higher injection pressure requirements at the top of the drill string (7.4 MPa in three-segment wellbore versus 5.9 MPa in vertical wellbore). To help with the compressor needs, injection rates at the top of the drill string can be reduced and the foam quality in the annulus can be controlled by changing the backpressure at the top of the annulus. The effect of varying parameter values on the bottom hole pressure is discussed in the following sections.

6.5 Parametric Study

Using the foam drilling simulator, a sensitivity analysis was performed on the effect of bottom hole pressure on changing the values of different operating variables during a foam drilling job. A detailed discussion on the results of the parametric study is presented in the subsequent sections.

6.5.1 Effect of Increasing Drilled Depth

Vertical Wellbore: Foam quality at bottom hole decreases from 0.58 to 0.51 and bottom hole pressure increases from 13.8 MPa (1954 psi) to 18.2 MPa (2645 psi) the injection pressure requirement initially remains fairly constant (~5.99 MPa or 869 psi), since, the foam qualities at the end of the drill string are similar. The gravitation component increases with depth and contributes to the pressure at the bottom of the drill string.

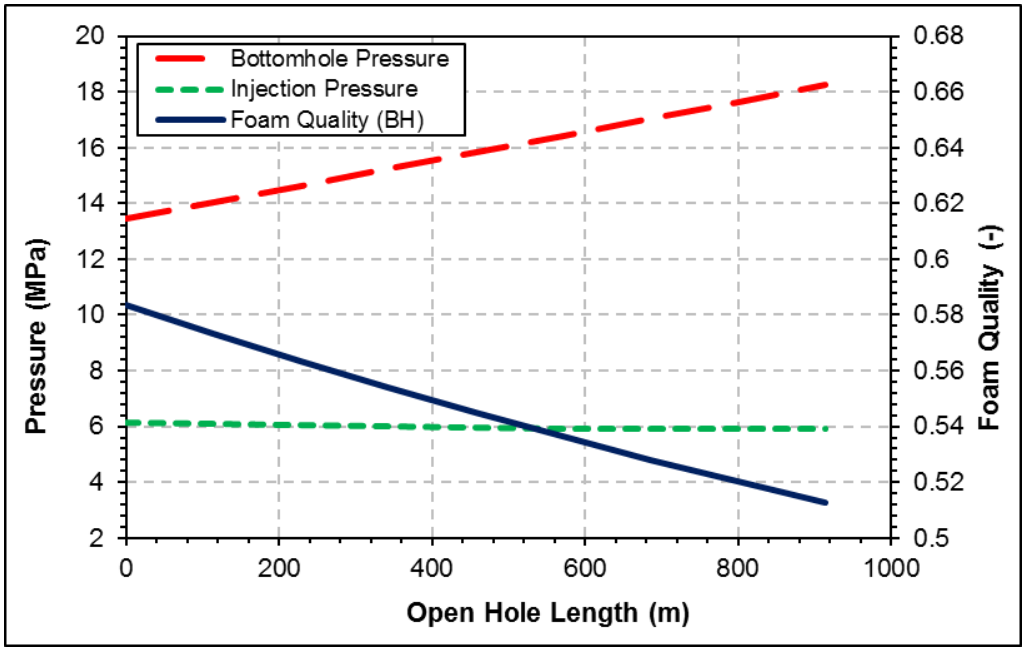

Figure 6.8: Effect of Drilled Depth on Drilling Parameters in a Vertical Wellbore

Three Segment Wellbore: Gradual changes in the drilling parameters is observed with foam quality changing from 0.64 to 0.61 and annular pressure changes from 9.2 MPa (1340 psi) to 10.4 MPa (1508 psi). Since the gravitational contribution to pressure at the bottom of the drill string is low, the injection pressure requirements are higher in a three-segment wellbore. Additionally, the foam quality at the bottom is higher at the bottom of drill string therefore, injection pressures show gradual increase. The range of injection pressure for the current set of drilling parameters in a three-segment wellbore is between 6.3 MPa (921 psi) to 7.4 MPa (1075 psi).

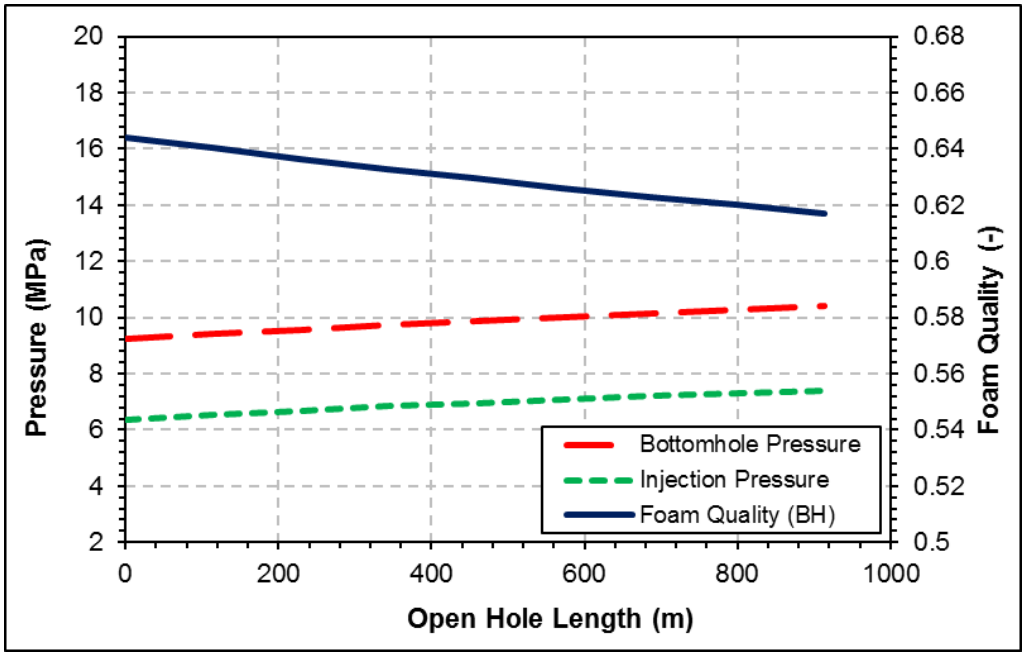

Figure 6.9: Effect of Drilled Depth on Drilling Parameters in a Three-Segment Wellbore

6.5.2 Effect of Gas and Liquid Injection Rates

Vertical Wellbore: Figure 6.10 shows the bottom hole pressure as a function of gas injection rates plotted for varying liquid flow rates. The bottom hole pressure initially decreases with increasing gas injection rate and then stabilizes to a fairly constant value. Also, pressure increases with the liquid injection rate. Foam starts building viscosity roughly at qualities greater than 0.55 (Section 5.6). Therefore, for a given liquid rate and low gas rates (less than that required for 55% quality foam) pressure is primarily governed by the hydrostatic head. At higher gas injection rates friction pressure also starts increasing along with the measured depth, however, hydrostatic still dominates. Similar trends have been reported by other authors in vertical wellbores (Ahmed *et al.*, 2003b; Devaul and Coy, 2003).

Foam quality at the bottom of the wellbore initially increases linearly with gas rate and then tapers off. This is probably due to the increased compressibility of foam at higher rates. Obviously, foam quality decreases with liquid flow rates (Figure 6.11).

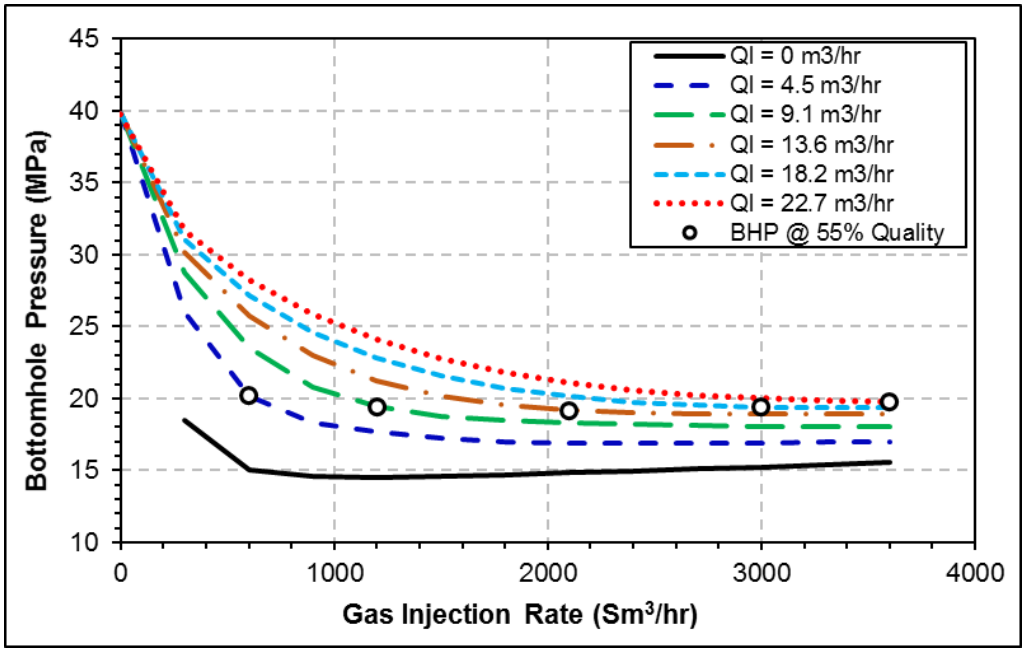

Figure 6.10: Effect of Gas and Liquid Injection Rates on Bottom Hole Pressure in a Vertical Wellbore

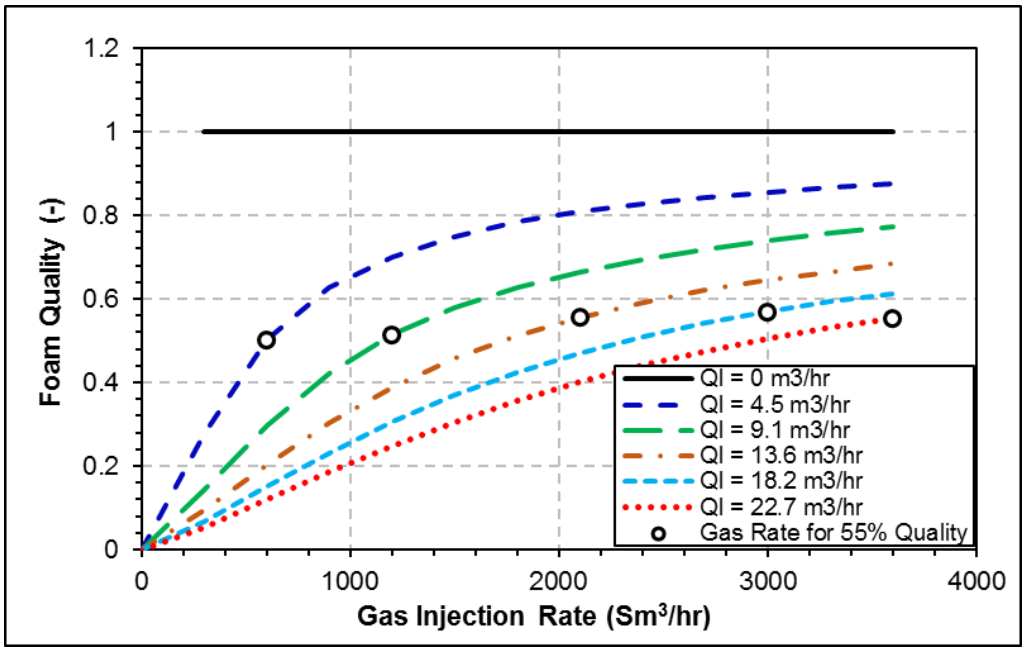

Figure 6.11: Effect of Gas and Liquid Injection Rates on Foam Quality at the Bottom of a Vertical Wellbore

Three Segment Wellbore: As opposed to a vertical wellbore, the contribution due to the hydrostatic head is lower in the inclined section and reduces to zero in the horizontal portion of the wellbore. At a given liquid injection rate, the bottom hole pressure initially decreases with increasing gas

rate due to reduced hydrostatic and reaches a minimum at a foam quality of 55 percent. With a further increase in gas rate, the frictional pressure dominates, and the bottom hole pressure starts increasing (Figure 6.12). Furthermore, due to lower bottom hole pressures as compared to a vertical wellbore, gas expansion is more. This results in higher foam quality and velocity and therefore, higher frictional pressure losses are observed in the three-segment wellbore.

To the left of the lowest bottom hole pressure point, the flow is gravity dominated and bottom hole pressure increases with increasing liquid rate. However, as the gas injection rates increase beyond the lowest pressure point, the flow becomes friction dominated and the trends reverse, i.e. higher quality foams (i.e., low liquid rates) show higher bottom hole pressures at high gas injection rate.

As explained earlier, since, the bottom hole pressures are lower in a three-segment wellbore, resulting foam qualities are higher at the bottom of the wellbore (Figure 6.13).

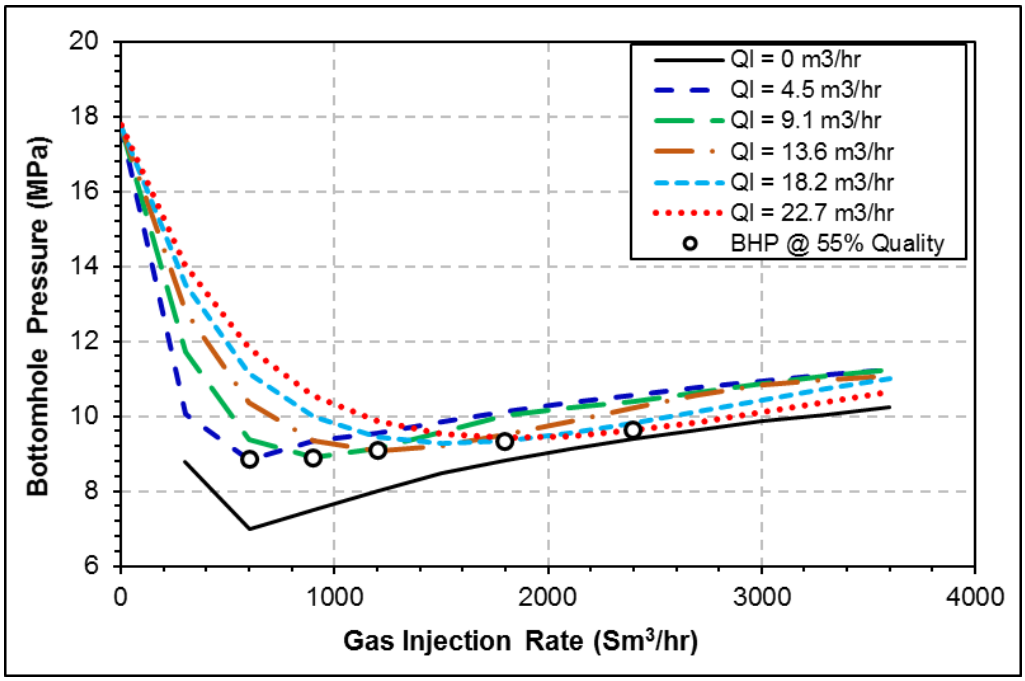

Figure 6.12: Effect of Gas and Liquid Injection Rates on Bottom Hole Pressure in a Three-Segment Wellbore

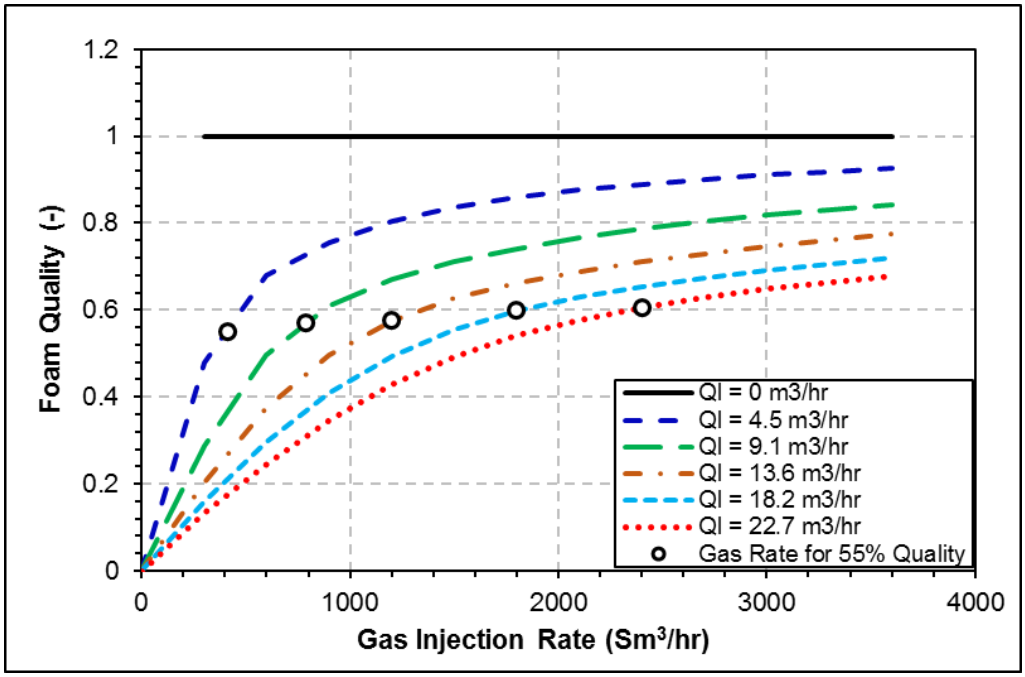

Figure 6.13: Effect of Gas and Liquid Injection Rates on Foam Quality at Bottom of a Three-Segment Wellbore

6.5.3 Effect of Backpressure

Using the base case gas and liquid injection rates, the backpressure at the top of the annulus was varied and its effect on the bottom hole pressure, required injection pressure, and foam quality at the bottom hole was observed in both the vertical and three-segment wellbores. Bottom hole pressure and injection pressures increased with backpressure, while the foam qualities at bottom of wellbore decreased. The rate of change of pressures (bottom hole pressure increased from 17.7 to 23.3 MPa; injection pressure increased from 5.9 to 8.2 MPa) and quality (decreased from 0.52 to 0.45) in the vertical wellbore is steeper (Figure 6.14), due to presence of hydrostatic head as compared to the three-segment wellbore (Figure 6.15). For the three-segment wellbore bottom hole pressure increased from 10.1 to 13.5 MPa, the injection pressure increased from 7.6 to 8 MPa, while the quality decreased from 0.62 to 0.55. It should be noted that higher injection pressures are required in the three-segment wellbore due to reduced contributions from hydrostatic inside the drill string.

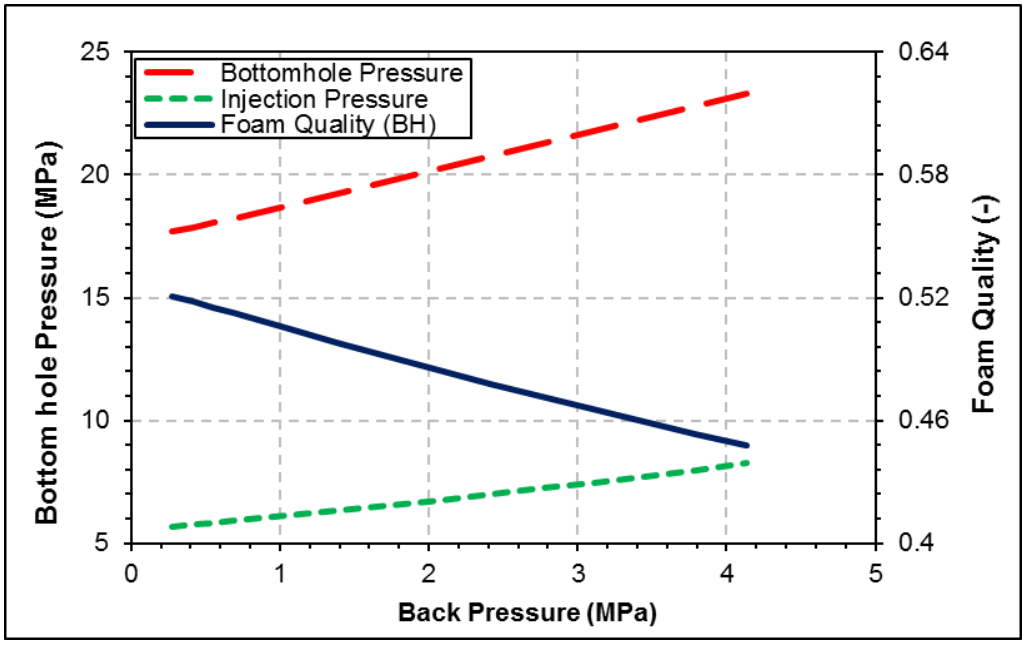

Figure 6.14: Effect of Changing Back Pressure on Bottom Hole Pressure and Foam Quality in a Vertical Wellbore

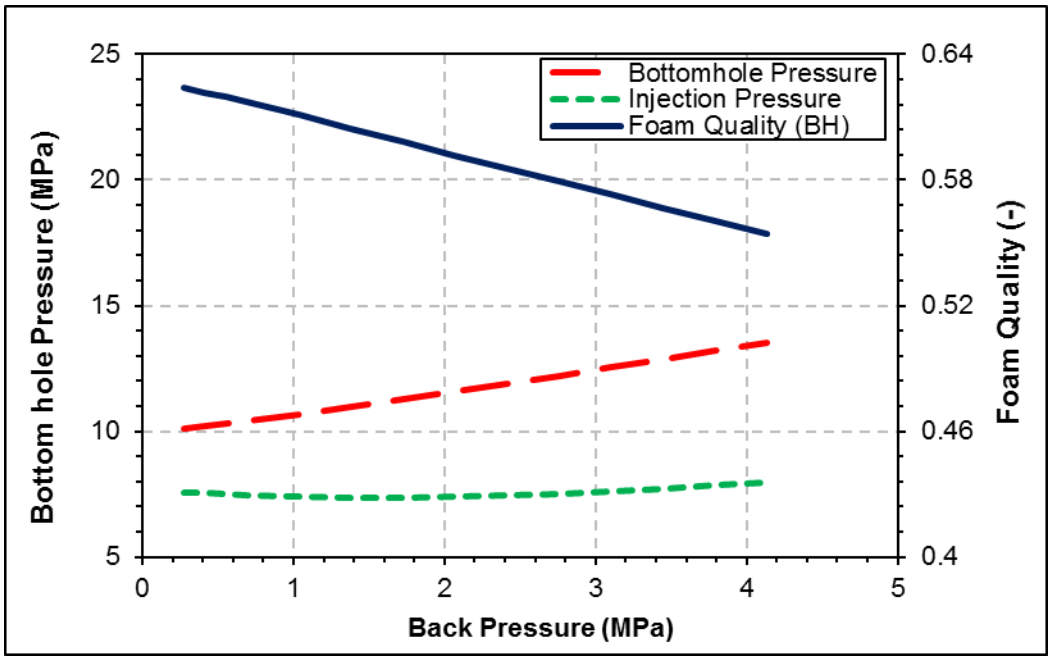

Figure 6.15: Effect of Changing Back Pressure on Bottom Hole Pressure and Foam Quality in a Three-Segment Wellbore

6.5.4 Effect of Rate of Penetration

A parametric study on the effect of ROP on the annular pressure, injection pressure and the foam quality were performed for vertical and three-segment wellbores. With increasing ROP the

annular cuttings concentration increases and results in higher solids friction factor. The additional frictional pressure drop due to the presence of solids is directly related to the cuttings concentration raised to the power of "0.3844", i.e., $C_s{}^{0.3844}$ (Eq. 6.11). Therefore, the annular pressure drop increases with ROP, and consequently, the required injection pressures also increase. Since the net frictional pressure drop is only dependent on the length of the flow path, therefore, rate of change of pressures in both vertical (Figure 6.16) and three-segment wellbores (Figure 6.17) are similar. It should be noted that the effect of cuttings in the hydrostatic was not accounted for in the present model. The foam qualities at the wellbore bottom show a steady decline due to higher pressures and reduced gas compressibility.

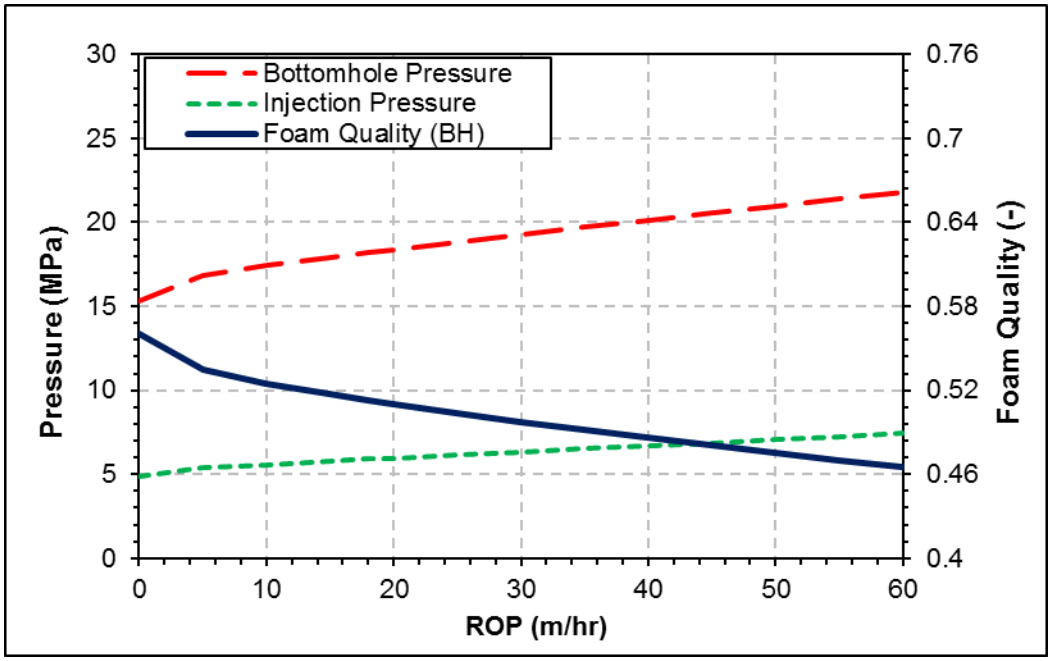

Figure 6.16: Effect of Changing Rate of Penetration on Bottom Hole Pressure and Foam Quality in a Vertical Wellbore

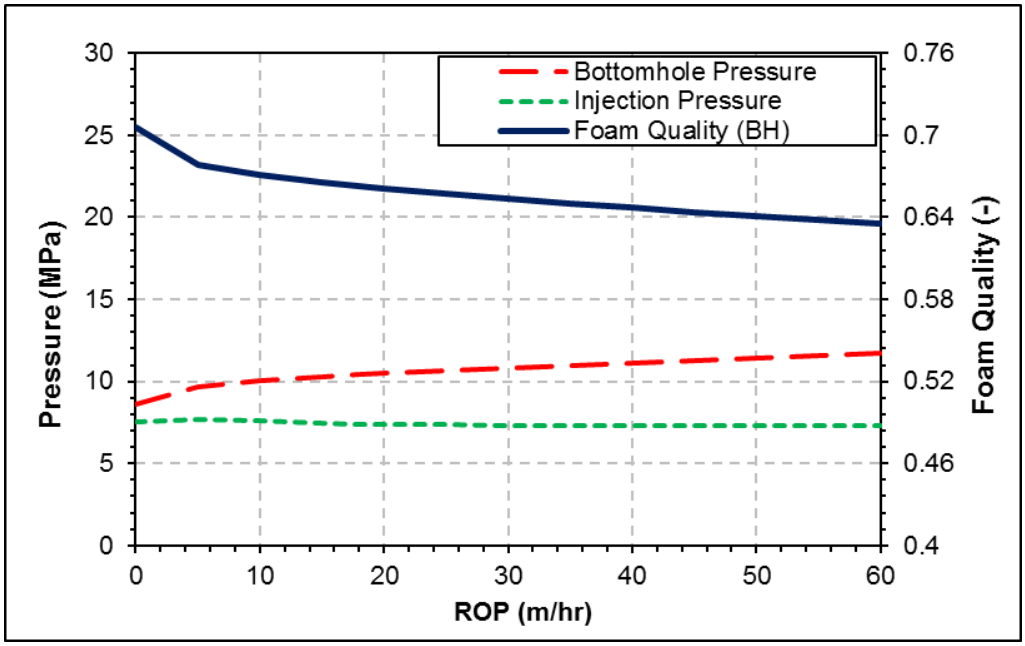

Figure 6.17: Effect of Changing Rate of Penetration on Bottom Hole Pressure and Foam Quality in a Three-Segment Wellbore

6.5.5 Effect of Geothermal Gradient

With increasing geothermal gradient, the resulting temperature along the wellbore is higher. This results in more gas expansion, and therefore, higher qualities along the wellbore. Foam quality influences both the hydrostatic and frictional pressures. From Figure 6.18 it can be observed that in a vertical wellbore, foam qualities along the wellbore increase steeply as the true vertical depth is greater, the resulting annular pressure is reduced as the foam expands with temperature. A similar trend is also observed in the three-segment wellbore, however, the rate of change of parameters is more gradual, due to lower downhole temperature, and marginal changes in the foam quality (Figure 6.19).

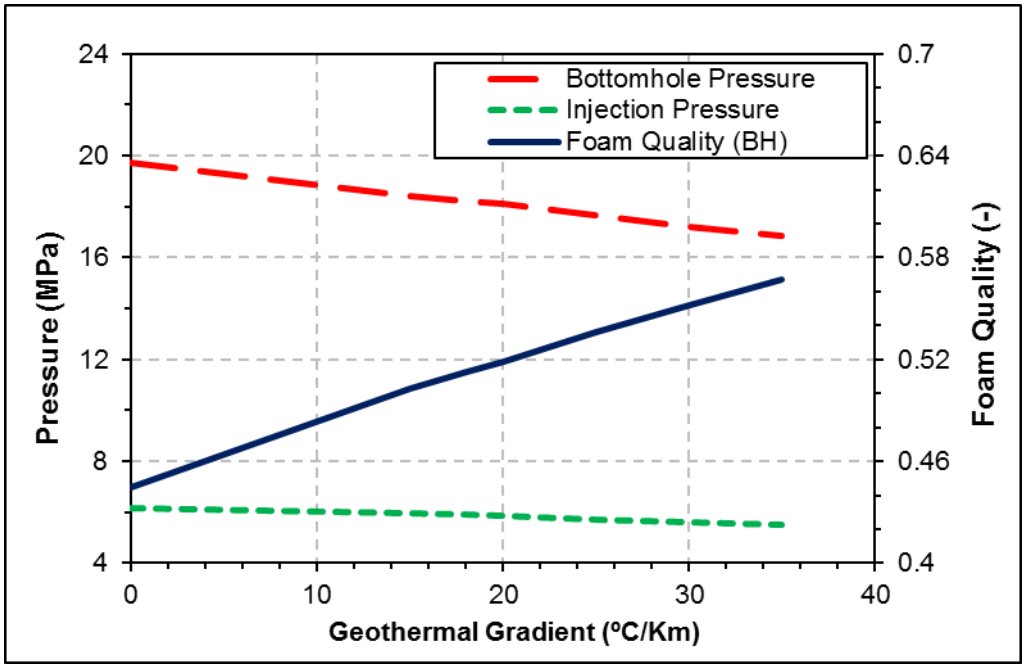

Figure 6.18: Effect of Changing Geothermal Gradient on Bottom Hole Pressure and Foam Quality in a Vertical Wellbore

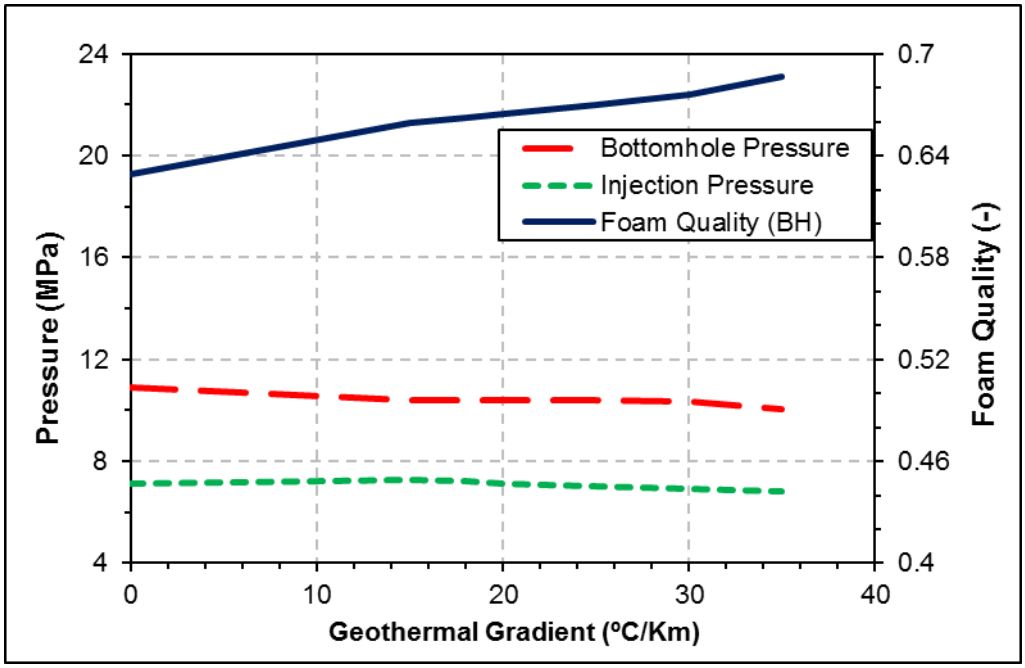

Figure 6.19: Effect of Changing Geothermal Gradient on Bottom Hole Pressure and Foam Quality in a Three-Segment Wellbore

Chapter 7

Conclusions and Recommendations

7.1 Conclusions

To investigate the rheology of foam, flow experiments were conducted using a recirculating flow loop equipped with pipe viscometers and eccentric annular sections. All tests were conducted at a pressure of 6.89 MPa (1000 psig), for a temperature range of 24°C (75°F) to 149°C (300°F) and for foam qualities between 0% to 75%. Based on experimental measurements, empirical correlations that account for the effect of temperature are developed to predict the rheology of PAC based polymeric foams. The performance of these correlations was checked against the pressure drop measurements obtained from an annular test section. Based on this investigation, the following conclusions can be made:

- Except a slight data scattering due to experimental variations, flow data from different pipe viscometers displayed a single flow curve at all tested temperatures, indicating the absence of an appreciable wall-slip in PAC-based polymer foams.
- High-quality PAC foam (75%) displayed yield stress of 8 Pa at ambient temperature; therefore, its rheology could be more accurately represented using a Herschel-Bulkley model.
- Temperature significantly affects the rheological properties of foams. Fluid behavior indices of both the base fluid and foam increased with temperature, approximately by a similar order of magnitudes. As a result, the normalized fluid behavior index of foams did not change with temperature. The increase in temperature reduced the consistency index of foam more

than that of the base fluid. Consequently, the normalized consistency index of foam mostly decreased with temperature.

- Experimental data is mostly in good agreement with the Bonilla-Shah (2000) model for the specific range for which the model is applicable.
- Experimental data matched hydraulic model predictions accurately at ambient temperature. However, discrepancies increased with temperature due to foam instability.
- In a vertical wellbore, the bottom hole pressure initially decreases as the gas injection rate increases and reaches a minimum value at a given liquid rate. This is because annular pressure is initially governed primarily by the hydrostatic head and as foam builds viscosity at high qualities (>55%), friction pressure starts taking effect. The bottom hole pressure increases with increasing liquid rates. Foam quality increases with gas injection rates and decreases with liquid rates.

7.2 Recommendations

This section lists a few recommendations and scope for future work that can be used to fill in the gaps in the present study and improve the overall reliability of the hydraulics prediction in an actual field operation.

- The present rheology model is valid to a maximum foam quality of 75%, which can accurately predict foam rheology and hydraulics, downhole at elevated temperatures. At shallower depths, the rheology model can be coupled with other published models to cover the range of foam qualities expected during normal UBD operations. However, while drilling geothermal wells where even at shallow depths the temperatures can be significantly high. This requires foam rheology models that account for temperature effect in higher quality foams (>75%). Therefore, experiments need to be extended to incorporate

higher foam qualities ranging to a maximum value of 95% as expected during field operations.

- To check the effect of higher polymer concentrations on foam rheology, flow tests should be conducted for aqueous foams and for a range of concentrations of PAC polymers. Higher polymer concentrations in the base fluid may improve foam performance at elevated temperatures by increasing film stability. Moreover, polymer concentrations in the base fluid are generally small, and therefore, there is no significant impact on the overall UBD economics.
- Although only minor scatter was observed in the current flow data, it is possible that the magnitude of the wall-slip was small and could not be identified. Furthermore, for a higher polymer concentration in the base fluid may cause noticeable wall slip which would require detailed wall slip corrections for rheology measurements.
- The present foam hydraulics model assumes a fully suspended cuttings flow both in vertical and 3-segment wellbores, which is not always true. Therefore, the hydraulics model can be coupled with a cuttings transport model, to predict the solids concentration profile along the wellbore. This will aid in examining the effectiveness of wellbore cleanout during foam fluid UBD. The addition of a cuttings transport model will aid in optimizing the hole cleaning by dynamically controlling the gas and liquid injection rates.
- Foam rheology is significantly affected by changes in temperature. In the current hydraulics model, a constant geothermal gradient was assumed. To improve the accuracy of the model predictions a more rigorous thermal model can be incorporated, which accounts for both vertical and radial heat transfer.

- Since, pipe rotation affects the velocity profiles, and pressure distribution in the annulus, which has a direct bearing on the cuttings distribution. Therefore, the effect of pipe rotation should be incorporated into the hydraulics model.

References

Ahmed, R.M. 2005. Experimental Study and Modeling of Yield Power Law Fluid Flow in Pipes and Annuli. Tulsa University Drilling Research Projects (TUDRP) Report.

Ahmed, R.M.; Kuru, E.; Saasen, A. 2003a. Critical review of drilling foam rheology. Annual Transactions of the Nordic Rheology Society 11.

Ahmed, R.; Kuru, E.; Saasen, A. 2003b. Mathematical Modeling of Drilling Foam Flows.: Canada.

Ahmed, R.; Miska, S. 2009. Advanced Drilling and Well Technology. *In* Advanced Wellbore Hydraulics. Society of Petroleum Engineers.

Ahmed, R.M.; Miska, S.Z.; Miska, W.Z. 2006. Friction Pressure Loss Determination of Yield Power Law Fluid in Eccentric Annular Laminar Flow. *In* Wiertnictwo Nafta Gaz, No. 23: Wiertnictwo Nafta Gaz: Krakow, Poland.

Ahmed, R.M.; Takach, N.E.; Khan, U.M.; Taoutaou, S.; James, S.; Saasen, A.; Godøy, R. 2009. Rheology of foamed cement. Cement and Concrete Research 39 (4): 353–361.

Akhtar, T.F. 2017. Rheology of Aqueous and Polymer-Based Nitrogen Foams at High pressure and High Temperature (HPHT) Conditions. Masters Thesis, Univeristy of Oklahoma: Norman, Oklahoma.

Akhtar, T.F.; Ahmed, R.; Elgaddafi, R.; Shah, S.; Amani, M. 2018. Rheological behavior of aqueous foams at high pressure. Journal of Petroleum Science and Engineering 162: 214–224.

Amro, M.; Finck, M.; Jaeger, P. 2015. Foams at Elevated Pressure in EOR. *In* SPE-172712-MS: Society of Petroleum Engineers: Manama, Bahrain.

Argillier, J.-F.; Saintpere, S.; Herzhaft, B.; Toure, A. 1998. Stability and Flowing Properties of Aqueous Foams for Underbalanced Drilling. *In* SPE-48982-MS: Society of Petroleum Engineers: New Orleans, Louisiana.

Babatola, D.F. 2014. Rheology of PAC polymer-based foams using pipe viscometers. MS thesis, University of Oklahoma: Norman, Oklahoma.

Barthes-Biesel, D.; Chhim, V. 1981. The constitutive equation of a dilute suspension of spherical microcapsules. International Journal of Multiphase Flow 7 (5): 493–505.

Batchelor, G. 1967. *In* An Introduction to Fluid Dynamics. Cambridge University Press: 247–253.

Bennion, D.B.; Thomas, F.B.; Bietz, R.F.; Bennion, D.W. 1998. Underbalanced Drilling: Praises and Perils. SPE-52889-PA.

Beyer, A.H.; Millhone, R.S.; Foote, R.W. 1972. Flow Behavior of Foam as a Well Circulating Fluid. *In* SPE-3986-MS: Society of Petroleum Engineers: San Antonio, Texas.

Blauer, R.E.; Mitchell, B.J.; Kohlhaas, C.A. 1974. Determination of Laminar, Turbulent, and Transitional Foam Flow Losses in Pipes. *In* SPE-4885-MS: Society of Petroleum Engineers: SPE.

Bonilla, L.F.; Shah, S.N. 2000. Experimental Investigation on the Rheology of Foams. *In* SPE-59752-MS: Society of Petroleum Engineers: Calgary, Alberta, Canada.

Brkić, D. 2011. Review of explicit approximations to the Colebrook relation for flow friction. Journal of Petroleum Science and Engineering 77 (1): 34–48.

Capo, J.; Yu, M.; Miska, S.Z.; Takach, N.E.; Ahmed, R.M. 2006. Cuttings Transport With Aqueous Foam at Intermediate-Inclined Wells. SPE Drilling & Completion 21 (2): 99–107.

Cawiezel, K.E.; Niles, T.D. 1987a. Rheological Properties of Foam Fracturing Fluids Under Downhole Conditions. *In* SPE-16191-MS: Society of Petroleum Engineers: Oklahoma City, Oklahoma.

Cawiezel, K.E.; Niles, T.D. 1987b. Rheological Properties of Foam Fracturing Fluids Under Downhole Conditions. *In* SPE-16191-MS: Society of Petroleum Engineers: Oklahoma City, Oklahoma.

Chen, Z. 2005. Cuttings transport with foam in horizontal concentric annulus under elevated pressure and temperature conditions. PhD Dissertation, University of Tulsa: Tulsa, Oklahoma.

Chen, Z.; Ahmed, R.M.; Miska, S.Z.; Takach, N.E.; Yu, M.; Pickell, M.B. 2005a. Rheology and Hydraulics of Polymer (HEC) Based Drilling Foams at Ambient Temperature Conditions. *In* SPE-94273-MS: Society of Petroleum Engineers: SPE.

Chen, Z.; Ahmed, R.M.; Miska, S.Z.; Takach, N.E.; Yu, M.; Pickell, M.B.; Hallman, J.H. 2005b. Rheology of Aqueous Drilling Foam Using a Flow-through Rotational Viscometer. *In* SPE-93431-MS: Society of Petroleum Engineers: The Woodlands, Texas.

Chen, Z.; Ahmed, R.M.; Miska, S.Z.; Takach, N.E.; Yu, M.; Pickell, M.B.; Hallman, J.H. 2005c. Rheology of Aqueous Drilling Foam Using a Flow-through Rotational Viscometer. *In* SPE-93431-MS: Society of Petroleum Engineers: The Woodlands, Texas.

Chen, Z.; Ahmed, R.M.; Miska, S.Z.; Takach, N.E.; Yu, M.; Pickell, M.B.; Saasen, A. 2005d. Rheology Characterization of Polymer Drilling Foams using a Novel Apparatus. ANNUAL TRANSACTIONS OF THE NORDIC RHEOLOGY SOCIETY 13.

Chen, Z.; Duan, M.; Miska, S.Z.; Yu, M.; Ahmed, R.M.; Hallman, J.H. 2009. Hydraulic Predictions for Polymer-Thickened Foam Flow in Horizontal and Directional Wells. SPE Drilling & Completion 24 (1): 40–49.

Clunie, J.S.; Goodman, J.F.; Ingram, B.T. In press. This Liquid Films. *In* Surface and Colloidal Science. Wiley: 167–239. New York.

Coussot, P. 2014. Yield stress fluid flows: A review of experimental data. Journal of Non-Newtonian Fluid Mechanics 211: 31–49.

David, A.; Marsden, S.S., Jr. 1969. The Rheology of Foam. *In* SPE-2544-MS: Society of Petroleum Engineers: Denver, Colorado.

Deshpande, N.S.; Barigou, M. 2000. The flow of gas–liquid foams in vertical pipes. Chemical Engineering Science 55 (19): 4297–4309.

Devaul, T.; Coy, A. 2003. Underbalanced horizontal drilling improves productivity. World Oil 224 (4): 33–36.

Dodge, D.W.; Metzner, A.B. 1959. Turbulent flow of non-newtonian systems. AIChE Journal 5 (2): 189–204.

Driscoll, P.L.; Bowen, J.G.; Roberts, M.A. 1980. Oil Base Foam Fracturing Applied To The Niobrara Shale Formation. *In* SPE-9335-MS: Society of Petroleum Engineers: SPE.

Duan, M.; Miska, S.Z.; Yu, M.; Takach, N.E.; Ahmed, R.M.; Hallman, J.H. 2008. The Effect of Drillpipe Rotation on Pressure Losses and Fluid Velocity Profile in Foam Drilling. *In* SPE-114185-MS: Society of Petroleum Engineers: Bakersfield, California, USA.

Durian, D.; Weitz, D. In press. Foams. In Kirk-Othmer Encyclopedia of Chemical Technology. 4th edn. 783–805 p. 1994.

Edrisi, A.; Gajbhiye, R.; Kam, S.I. 2014. Experimental Study of Polymer-Free and Polymer-Added Foams for Underbalanced Drilling: Are Two Foam-Flow Regimes Still There? SPE Journal 19 (1).

Edrisi, A.; Kam, S.I. 2014a. A New Foam Model in Pipes for Drilling and Fracturing Application. SPE Journal 19 (4): 576–585.

Edrisi, A.; Kam, S.I. 2014b. A New Foam Model in Pipes for Drilling and Fracturing Application. SPE Journal 19 (4): 576–585.

Edrisi, A.R.; Kam, S.I. 2015. New Foam Drilling Hydraulics Calculations by Using Two Foam Flow Regimes. *In* SPE-174769-MS: Society of Petroleum Engineers: Houston, Texas, USA.

Einstein, A. 1906. Eine Neve Bestimmung Der Molekuldimensionen. Annalen Der Physik 19 (SFR 4): 289.

Enzendorfer, C.; Harris, R.A.; Valkó, P.; Economides, M.J.; Fokker, P.A.; Davies, D.D. 1994. Pipe viscometry of foams. Journal of Rheology 39: 345–358.

Escudier, M.P.; Oliveira, P.J.; Pinho, F.T. 2002. Fully developed laminar flow of purely viscous non-Newtonian liquids through annuli, including the effects of eccentricity and inner-cylinder rotation. International Journal of Heat and Fluid Flow 23 (1): 52–73.

Exerowa, D.; Kruglyakov, P.M. 1997. Foam and foam films: theory, experiment, application. Elsevier.

Fang, P.; Manglik, R.M.; Jog, M.A. 1999. Characteristics of laminar viscous shear-thinning fluid flows in eccentric annular channels. Journal of Non-Newtonian Fluid Mechanics 84 (1): 1–17.

Farajzadeh, R.; Vincent-Bonnieu, S.; Bourada, N.B. 2014. Effect of Gas Permeability and Solubility on Foam. Journal of Soft Matter 2014: 1–7.

Frankel, N.A.; Acrivos, A. 1970. The constitutive equation for a dilute emulsion. J. Fluid Mech. 44 (1): 65–78.

Fredrickson, A.; Bird, R.B. 1958. Non-Newtonian Flow in Annuli. Industrial & Engineering Chemistry 50 (3): 347–352.

Gajbhiye, R.N. 2011. Characterization of foam flow in pipes using two flow regime concept. Dissertation for PhD, Louisiana State University.

Gajbhiye, R.N.; Kam, S.I. 2012. The effect of inclination angles on foam rheology in pipes. Journal of Petroleum Science and Engineering 86–87: 246–256.

Gardiner, B.S.; Dlugogorski, B.Z.; Jameson, G.J. 1998. Rheology of fire-fighting foams. Fire Safety Journal 31 (1): 61–75.

Gopal, A.D.; Durian, D.J. 1999. Shear-Induced "Melting" of an Aqueous Foam. Journal of Colloid and Interface Science 213 (1): 169–178.

Gopal, A.D.; Durian, D.J. 2003. Relaxing in Foam. PHYSICAL REVIEW LETTERS 91 (188303).

Govindu, A.; Ahmed, R.; Shah, S.; Amani, M. 2019. Stability of foams in pipe and annulus. Journal of Petroleum Science and Engineering 180: 594–604.

Gu, M.; Mohanty, K.K. 2015a. Rheology of polymer-free foam fracturing fluids. Journal of Petroleum Science and Engineering 134: 87–96.

Gu, M.; Mohanty, K.K. 2015b. Rheology of polymer-free foam fracturing fluids. Journal of Petroleum Science and Engineering 134: 87–96.

Haaland, S.E. 1983. Simple and Explicit Formulas for the Friction Factor in Turbulent Pipe Flow. Journal of Fluids Engineering 105 (1): 89–90.

Harris, P.C. 1985. Dynamic Fluid Loss Characteristics of Foam Fracturing Fluids. Journal of Petroleum Technology 37 (10): 1847–1852.

Harris, P.C. 1989. Effects of Texture on Rheology of Foam Fracturing Fluids. SPE Production Engineering 4 (03): 249–257.

Harris, P.C.; Heath, S.J. 1996. High-Quality Foam Fracturing Fluids. *In* SPE-35600-MS: Society of Petroleum Engineers: Calgary, Alberta, Canada.

Harris, P.C.; Pippin, P.M. 2000. High-Rate Foam Fracturing: Fluid Friction and Perforation Erosion. SPE Production & Facilities 15 (1): 27–32.

Harris, P.C.; Reidenbach, V.G. 1987. High-Temperature Rheological Study of Foam Fracturing Fluids. Journal of Petroleum Technology 39 (5).

Hatschek, E. 1911. Die Viskosität der Dispersoide. Wissenschaftliche und technische Rundschau für das Gesamtgebiet der Kolloide 8 (1): 34–39.

Heller, J.P.; Kuntamukkula, M.S. 1987. Critical review of the foam rheology literature. Industrial & Engineering Chemistry Research 26 (2): 318–325.

Herzhaft, B. 1999. Rheology of Aqueous Foams: a Literature Review of some Experimental Works. Oil & Gas Science and Technology 54 (5): 587–596.

Herzhaft, B. 2002. Correlation between Transient Shear Experiments and Structure Evolution of Aqueous Foams. Journal of Colloid and Interface Science 247 (2): 412–423.

Herzhaft, B.; Kakadjian, S.; Moan, M. 2005. Measurement and modeling of the flow behavior of aqueous foams using a recirculating pipe rheometer. Colloids and Surfaces A: Physicochemical and Engineering Aspects 263 (1–3): 153–164.

Hutchins, R.D.; Miller, M.J. 2003. A Circulating Foam Loop for Evaluating Foam at Conditions of Use. *In* SPE-80242-MS: Society of Petroleum Engineers: Houston, Texas.

Kakadjian, S.; Herzhaft, B.; Neau, L. 2003. HP/HT Rheology of Aqueous Compressible Fluids for Underbalanced Drilling Using A Recirculating Rheometer. *In* SPE-80207-MS: Society of Petroleum Engineers: Houston, Texas.

Khade, S.D.; Shah, S.N. 2004. New Rheological Correlations for Guar Foam Fluids. SPE Production & Facilities 19 (2): 77–85.

Khan, S.A.; Armstrong, R.C. 1986. Rheology of foams: I. Theory for dry foams. Journal of Non-Newtonian Fluid Mechanics 22 (1): 1–22.

Khan, S.A.; Schnepper, C.A.; Armstrong, R.C. 1988. Rheology of foams: III. Measurement of Shear Flow Properties. Journal of Rheology 32: 69–92.

Kozicki, W.; Tiu, C. 1986. Parametric Modeling of Flow Geometries in Non-Newtonian Flows. *In* Encyclopedia of Fluid Mech. 200–248.

Kraynik, A. 1982. Paper B-10, Annual meeting of the Society of Rheology.

Kraynik, A.M. 1988. Foam Flows. Ann. Rev. Fluid Mech 20: 325–357.

Kraynik, A.M.; Hansen, M.G. 1986. Foam rheology: a model of viscous phenomena. Journal of Rheology 31 (175): 175–205.

Kroezen, A.B.J.; Wassink, J.G.; Schipper, C.A.C. 1988. The flow properties of foam. Twente Unioersity of Technoiogy. Enschede, The Netherlands, JSDC Volume 104: 393–400.

Lam, C.; Jefferis, S.A. 2014. Interpretation of viscometer test results for polymer support fluids. Geotechnical Special Publication, American Society of Civil Engineers: 439–449.

Li, Y.; Kuru, E. 2005. Numerical Modelling of Cuttings Transport With Foam in Vertical Wells. Journal of Canadian Petroleum Technology 44 (03).

Llewellin, E.W.; Mader, H.M.; Wilson, S.D.R. 2002. The rheology of a bubbly liquid. Proceedings of the Royal Society A: Mathematical, Physical and Engineering Sciences 458 (2020): 987–1016.

Llewellin, E.W.; Manga, M. 2005. Bubble suspension rheology and implications for conduit flow. Journal of Volcanology and Geothermal Research 143 (1): 205–217.

Lourenco, A.M.F.; Miska, S.Z.; Reed, T.D.; Pickell, M.B.; Takach, N.E. 2004a. Study of the Effects of Pressure and Temperature on the Viscosity of Drilling Foams and Frictional Pressure Losses. SPE Drilling & Completion 19 (03): 139–146.

Lourenco, A.M.F.; Miska, S.Z.; Reed, T.D.; Pickell, M.B.; Takach, N.E. 2004b. Study of the Effects of Pressure and Temperature on the Viscosity of Drilling Foams and Frictional Pressure Losses. SPE Drilling & Completion 19 (03): 139–146.

Lyons, W.C.; Guo, B.; Graham, R.L.; Hawley, G.D. 2009. Chapter 6: Direct Circulation Models. *In* Air and Gas Drilling Manual: Applications for Oil and Gas Recovery Wells and Geothermal Fluids Recovery Wells. Elsevier.

Mader, H.M.; Llewellin, E.W.; Mueller, S.P. 2013. The rheology of two-phase magmas: A review and analysis. Journal of Volcanology and Geothermal Research 257: 135–158.

Marsden, S.S.; Eerligh, J.P.; Albrecht, R.A.; David, A. 1967. Use of Foam in Petroleum Operations. *In* WPC-12224: World Petroleum Congress: WPC.

Martins, A.L.; Lourenço, A.M.F.; Sa, C.H.M.; Silva, V., Jr. 2001. Foam Rheology Characterization as a Tool for Predicting Pressures While Drilling Offshore Wells in UBD Conditions. *In* SPE-67691-MS: Society of Petroleum Engineers: Amsterdam, Netherlands.

Mitchell, B.J. 1970. Viscosity of foam. Dissertation (Ph.D.), University of Oklahoma.

Mooney, M. 1951. The viscosity of a concentrated suspension of spherical particles. Journal of Colloid Science 6 (2): 162–170.

Nguyen, Q.D.; Boger, D.V. 1992. Measuring the Flow Properties of Yield Stress Fluids. Annual Review of Fluid Mechanics 24 (1): 47–88.

Nguyen, A.V.; Farrokhpay, S.; Wang, J. 2016. A critical review of the growth, drainage and collapse of foams. Advances in Colloid and Interface Science 228: 55–70.

Obeida, T.A.; Heinemann, Z.E.; Kriebernegg, M. 1997. Accurate Calculations of Compressibility Factor for Pure Gases and Gas Mixtures. *In* SPE-37440-MS: Society of Petroleum Engineers: 11. SPE.

Okpobiri, G.A. 1982. Experimental determination of solids friction factors and minimum volumetric requirements in foam and mist drilling and well cleanout operations. PhD Dissertation, University of Tulsa: Tulsa, Oklahoma.

Okpobiri, G.A.; Ikoku, C.U. 1983. Experimental Determination of Friction Factors for Mist and Foam Drilling and Well Cleanout Operations. Journal of Energy Resources Technology 105 (4): 542.

Okpobiri, G.A.; Ikoku, C.U. 1986. Volumetric Requirements for Foam and Mist Drilling Operations. SPE Drilling Engineering 1 (1): 71–88.

Ozbayoglu, M.E. 2002. Cuttings Transport with in horizontal and highly inclined wellbores. Ph.D. Dissertation, University of Tulsa: Tulsa, Oklahoma.

Ozbayoglu, M.E. 2007. Pressure Drop at the Bit During Foam Drilling. *In* PETSOC-2007-212: Petroleum Society of Canada: PETSOC.

Ozbayoglu, M.E.; Akin, S.; Eren, T. 2005. Foam Characterization Using Image Processing Techniques. *In* SPE-93860-MS: Society of Petroleum Engineers: Irvine, California.

Ozbayoglu, M.E.; Kuru, E.; Miska, S.; Takach, N. 2002. A Comparative Study of Hydraulic Models for Foam Drilling. Journal of Canadian Petroleum Technology 41 (06): 52–61.

Patton, J.T.; Holbrook, S.T.; Hsu, W. 1983. Rheology of Mobility-Control Foams. Society of Petroleum Engineers Journal 23 (3): 456–460.

Peysson, Y.; Herzhaft, B. 2005. Lubrication Process at the Wall in Foam Flow - Application to Pressure Drop Estimation While Drilling UBD Wells. *In* PETSOC-2005-149: Petroleum Society of Canada: Calgary, Alberta.

Phillips, A.M.; Couchman, D.D.; Wilke, J.G. 1987. Successful Field Application of High-Temperature Rheology of CO2 Foam Fracturing Fluids. *In* SPE-16416-MS: Society of Petroleum Engineers: Denver, Colorado.

Piercy, N.A.V.; Hooper, M.S.; Winny, H.F. 1933. Viscous flow through pipes with core. London Edinburgh Dublin Phil. Mag J. Sci. 15: 647–676.

Princen, H.M. 1983. Rheology of foams and highly concentrated emulsions: I. Elastic properties and yield stress of a cylindrical model system. Journal of Colloid and Interface Science 91 (1): 160–175.

Princen, H.M. 1985. Rheology of foams and highly concentrated emulsions. II. experimental study of the yield stress and wall effects for concentrated oil-in-water emulsions. Journal of Colloid and Interface Science 105 (1): 150–171.

Prud'Homme, R.K. 1981. *In* 53rd Annula Meeting of the Society of Rheology: Paper E-7: Louisville Inn, Louisville, KY.

Prud'homme, R.K.; Khan, S.A. 1996. Experimental results on foam rheology. In Foams: Theory, Measurements, and Applications. CRC Press.: 217–243 p.

Raza, S.H.; Marsden, S.S. 1967. The Streaming Potential and the Rheology of Foam. Society of Petroleum Engineers Journal 7.

Reidenbach, V.G.; Harris, P.C.; Lee, Y.N.; Lord, D.L. 1986. Rheological Study of Foam Fracturing Fluids Using Nitrogen and Carbon Dioxide. SPE Production Engineering 1 (01).

Rojas, Y.; Kakadjian, S.; Aponte, A.; Marquez, R.; Sanchez, G. 2001. Stability and Rheological Behavior of Aqueous Foams for Underbalanced Drilling. *In* SPE-64999-MS: Society of Petroleum Engineers: Houston, Texas.

Rust, A.C.; Manga, M. 2002. Effects of bubble deformation on the viscosity of dilute suspensions. Journal of Non-Newtonian Fluid Mechanics 104 (1): 53–63.

Saintpere, S.; Marcillat, Y.; Bruni, F.; Toure, A. 2000a. Hole Cleaning Capabilities of Drilling Foams Compared to Conventional Fluids. *In* SPE-63049-MS: Society of Petroleum Engineers: SPE.

Saintpere, S.; Marcillat, Y.; Bruni, F.; Toure, A. 2000b. Hole Cleaning Capabilities of Drilling Foams Compared to Conventional Fluids. *In* SPE-63049-MS: Society of Petroleum Engineers: SPE.

Sanghani, V. 1982. Rheology of Foam and Its Implications in Drilling and Cleanout Operations. MS thesis, University of Tulsa: Tulsa, Oklahoma.

Sanghani, V.; Ikoku, C.U. 1983. Rheology of Foam and Its Implications in Drilling and Cleanout Operations. Journal of Energy Resources Technology 105 (3): 362–371.

Sani, A.M.; Shah, S.N.; Baldwin, L. 2001. Experimental Investigation of Xanthan Foam Rheology. *In* SPE-67263-MS: Society of Petroleum Engineers: Oklahoma City, Oklahoma.

Schramm, L.L. 1994. Foams fundamentals and applications in the petroleum industry / Laurier L. Schramm, editor. Washington, DC : American Chemical Society: Washington, DC.

Sepulveda, J.J.; Falana, O.M.; Kakadjian, S.; Morales, J.D.; Zamora, F.; DiBiasio, M.; Marshall, E.C.; Shirley, G.L.; Benoit, D.J.; Tkach, S.A. 2008. Oil-Based Foam and Proper Underbalanced-Drilling Practices Improve Drilling Efficiency in a Deep Gulf Coast Well. *In* SPE-115536-MS: Society of Petroleum Engineers: SPE.

Shah, S.N.; Shanker, N.H.; Ogugbue, C.C. 2010. Future Challenges of Drilling Fluids and Their Rheological Measurements. *In* AADE-10-DF-HO-41: Houston, TX, US.

Sherif, T.; Ahmed, R.; Shah, S.; Amani, M. 2015a. Rheological and Wall-Slip Behaviors of Polymer Based Drilling Foams. (56581): V010T11A036.

Sherif, T.; Ahmed, R.; Shah, S.; Amani, M. 2015b. Rheological behavior of oil-based drilling foams. Journal of Natural Gas Science and Engineering 26: 873–882.

Szilas, A.P.; Bobok, E.; Navratil, L. 1981. Determination of turbulent pressure loss of non-newtonian oil flow in rough pipes. Rheologica Acta 20 (5): 487–496.

Tan, H.C.S.; McGowen, J.M. 1991. Friction Pressure Correlation for CO2 Foam Fluids. *In* SPE-21856-MS: Society of Petroleum Engineers: SPE.

Thondavadi, N.N.; Lemlich, R. 1985. Flow Properties of Foam With and Without Solid Particles. Industrial & Engineering Chemistry Process Design and Development 24: 748–753.

Truby, J.M.; Mueller, S.P.; Llewellin, E.W.; Mader, H.M. 2014. The rheology of three-phase suspensions at low bubble capillary number. Proceedings of the Royal Society A: Mathematical, Physical and Engineering Science 471 (2173).

Valko, P.; Economides, M.J. 1992. Volume Equalized Constitutive Equations for Foamed Polymer Solutions. Journal of Rheology 6: 1033–1055.

Washington, A. 2004. A preliminary study of the rheology of foam using rotational viscometer. Masters Thesis, University of Tulsa: Oklahoma.

Weaire, D.L.; Hutzler, S. 2001. The Physics of foams. Oxford University Press.

Weaire, D.; Hutzler, S.; Drenckhan, W.; Saugey, A.; Cox, S.J. 2006. The Rheology of Foams. *In* Smart Colloidal Materials (Richtering, W.; editor). Springer Berlin Heidelberg: 100–105. Berlin, Heidelberg.

Wendorff, C.L.; Earl, R.B. 1983. Foam Fracturing Laboratory. *In* SPE-12025-MS: Society of Petroleum Engineers: San Francisco, California.

Wilson, A.J. 1996. Experimental Techniques for the Characterization of Foams. *In* Foams: Theory Measures and Applications. Marcel Dekker Inc.: 243–275.

Zamora, M.; Lord, D.L. 1974. Practical Analysis of Drilling Mud Flow in Pipes and Annuli. *In* SPE-4976-MS: Society of Petroleum Engineers: SPE.

Nomenclature

A	Surface area of foam
c	Compressibility
Ca	Capillary number
d_s	Diameter of drilled solids
D	Diameter
D_{bob}	Diameter of the bob in a rotational viscometer
D_{cup}	Diameter of the cup in a rotational viscometer
$\mathrm{D}_{\mathrm{n_{eq}}}$	Equivalent diameter of the drill bit nozzles
e	Pipe eccentricity
E	Surface energy
f	Fanning friction factor
g	Acceleration due to gravity, 9.81 m/s^2
g_c	Conversion factor, 1 (kg-m)/(N-s^2)
G'	Elastic modulus
H_{bob}	Height of bob in a rotational viscometer
k_{T}	Torsion spring constant of a rotational viscometer
K	Fluid consistency index
L	Pipe section length
M	Molecular weight of a gas
n	Fluid flow behavior index for power-law fluid
n_n	Number of nozzles on the drill bit
N	Generalized fluid flow behavior index
P	Pressure
ΔP_{bit}	Pressure drop across bit
$\Delta P/_{\Delta L}$	Pressure gradient
Q	Volumetric flow rate
r_b	Average bubble radius

r_{cell}	Average radius of two-dimensional pencil stack foam model
R	Universal gas constant
R	Pipe Radius
R_{bob}	Radius of rotational viscometer bob
R_{cup}	Radius of rotational viscometer cup
R_{vane}	Radius of rotational vane viscometer bob
Re	Reynolds number
Re_{VE}	Volume equalized Reynolds number
ROP	Rate of penetration
T	Temperature
$d\Delta T/dL$	Geothermal gradient
u	Velocity
U	Mean velocity
V	Volume
Z	Gas compressibility factor in the real gas equation of state

Greek Symbols

β	Ratio of bob to cup diameter in a rotational viscometer, D_{bob}/D_{cup}
β_{slip}	Slip correction coefficient
$\dot{\gamma}$	Shear rate
$\dot{\gamma}_c$	Critical shear rate to begin fluid deformation
$\dot{\gamma}_w$	Wall shear rate
δ	Offset distance between two centers in an eccentric annulus
δ_{film}	Liquid layer thickness at the pipe wall
ε	Specific volume expansion ratio
ϵ	Absolute roughness
θ	Inclination angle
θ_{bob}	Angular displacement of the torsion spring
κ	Ratio of diameters in an annulus, D_i/D_o

λ	Ratio of the viscosity of dispersed phase to continuous phase, μ_{dis}/μ_{con}
μ	Apparent viscosity
μ_{dis}	Dispersed phase viscosity
μ_{con}	Continuous Phase viscosity
μ_e	Effective viscosity
μ_p	Plastic viscosity
μ_r	Relative viscosity
μ_{sus}	Suspension viscosity
ρ	Density
σ	Surface tension
τ	Shear stress
τ_w	Wall shear stress
τ_Y	Yield stress
T	Torque on the surface of the bob in a rotational viscometer
ϕ	Formation porosity
ϕ_b	Bubble fraction
Ω	Angular velocity of rotation sleeve in a rotational viscometer

Subscripts

24	Foam properties at 24ºC
av	Average
b	Bubble
bp	Backpressure
bit	Bit
bob	Bob
BH	Bottom hole
c	Critical
con	Continuous phase
$core$	Flow in the pipe core

cup	Cup
dis	Dispersed phase
DP	Drill pipe
e	Effective
eq	Equivalent pipe diameter in the annulus
eq	Equivalent nozzle diameter
f	Friction component
$fluid$	Flow due to fluidity
F	Foam
G	Gas
h	Hydraulic diameter
i	Internal
L	Base liquid
n	Nozzle
o	Outer
OH	Open hole
p	Plastic
r	Relative
s	Drilled solids/cuttings
sc	Standard conditions, 100 kPa, and 0ºC
$slip$	Flow due to slip
sus	Suspension
T	Torsion
T	Isothermal
US	Upstream
$vane$	Rotational vane viscometer
w	Wall
$water$	Water
Y	Yield

Appendix I

Experimental Data for Development of Foam Rheology Correlations

Table I-1 presents the experimentally determined fluid behavior and consistency indices for PAC based foams gathered at different temperatures and foam qualities.

Table I-1: Fluid Parameters used to formulate foam rheology correlations

Quality (%)	T (°C)	n_F (Dimensionless)	K_F (Pa-s^n)
0%	24	0.70	0.0565
45%	24	0.68	0.1999
55%	24	0.67	0.4145
65%	24	0.62	1.0975
75%	24	0.40	8.1072
0%	52	0.72	0.0314
45%	52	0.70	0.1248
55%	52	0.69	0.2364
65%	52	0.63	0.7023
75%	52	0.42	5.2592
0%	79	0.74	0.0204
45%	79	0.73	0.0662
55%	79	0.71	0.1354
65%	79	0.65	0.4238
75%	79	0.43	4.0473
0%	107	0.77	0.0169

Quality (%)	T (ºC)	n_F (Dimensionless)	K_F (Pa-s^n)
45%	107	0.76	0.0302
55%	107	0.74	0.0583
65%	107	0.67	0.1609
75%	107	0.45	2.1745
0%	127	0.80	0.0099
45%	127	0.79	0.0151
55%	127	0.77	0.0287
65%	127	0.68	0.1060
75%	127	0.46	1.2005
0%	149	0.83	0.0067
45%	149	0.82	0.0079
55%	149	0.80	0.0199
65%	149	0.70	0.0648
75%	149	0.50	0.9109

Appendix II

Correlations Used to Calculate Geometric Factors

To express the generalized shear rate ($\bar{\gamma}_w$) in terms of nominal Newtonian shear rate, the geometric factors (a and b) in Eq. (5.5) is obtained using the following set of correlations (Ahmed *et al.*, 2006) Ahmed et al. 2006).

$$a = a_0 e^3 + a_1 e^2 + a_2 e + a_3 \tag{II.1}$$

$$b = b_0 e^3 + b_1 e^2 + b_2 e + b_3 \tag{II.2}$$

where e is the dimensionless pipe eccentricity.

The constants ($a_0, a_1, a_2, a_3, b_0, b_1, b_2, b_3$) in the above equation are calculated using the following set of equations,

$$a_0 = -2.8711\kappa^2 - 0.1029\kappa + 2.6581 \tag{II.3}$$

$$a_1 = 2.8156\kappa^2 + 3.6114\kappa - 4.9072 \tag{II.4}$$

$$a_2 = 0.7494\kappa^2 - 4.8048\kappa + 2.2764 \tag{II.5}$$

$$a_3 = -0.3939\kappa^2 + 0.7211\kappa + 0.1503 \tag{II.6}$$

$$b_0 = 3.0422\kappa^2 + 2.4094\kappa - 3.1931 \tag{II.7}$$

$$b_1 = -2.7817\kappa^2 - 7.9865\kappa + 5.8970 \tag{II.8}$$

$$b_2 = -0.3406\kappa^2 + 6.0164\kappa - 3.3614 \tag{II.9}$$

$$b_3 = 0.2500\kappa^2 - 0.5780\kappa + 1.3591 \tag{II.10}$$

where, κ = diameter ratio (D_i/D_o).

Appendix III

Hydraulic Model Formulation

III.1 Equation of State

The Equation of State (EOS) was derived assuming that gas was compressible, and the liquid phase was incompressible. The real gas equation was used to calculate the density of gas at specific values.

$$PV_G = ZnRT = Z\frac{m_G}{M}RT \text{ or } \quad PM = Z\frac{m_G}{V_G}RT = Z\rho_G RT \tag{III.1}$$

where M is Molecular weight of gas; m_G is the mass of gas; V_G is Volume of gas; ρ_G is the Density of gas; R is gas constant. Above equation can be further simplified to determine the volume of gas,

$$V_G = \frac{ZnRT}{P} = Z\frac{m_G}{PM}RT \tag{III.2}$$

Using the definition of foam quality,

$$\Gamma = \frac{V_G}{V_G + V_L} \tag{III.3}$$

$$V_L = Z\frac{m_G}{PM}RT\left(\frac{1}{\Gamma} - 1\right) \tag{III.4}$$

Since, the fluid is incompressible, the liquid volume, V_L = constant, i.e.,

$$\frac{ZT}{P}\left(\frac{1}{\Gamma} - 1\right) = constant \tag{III.5}$$

or,

$$\frac{Z_1 T_1}{P_1}\left(\frac{1}{\Gamma_1} - 1\right) = \frac{Z_2 T_2}{P_2}\left(\frac{1}{\Gamma_2} - 1\right) \tag{III.6}$$

where, Pressure, P, Temperature, T, and Compressibility factor, Z are calculated at two different positions, "1" and "2".

Nitrogen gas was used for the present study and the compressibility factor for nitrogen gas at varying conditions was calculated using the empirical relations provided by (Obeida *et al.*, 1997). The compressibility factor of pure Nitrogen is expressed as,

$$Z_{N_2} = a_0 + a_1 P + a_2 P^2 \quad \text{(III.7a)}$$

where, Z_{N_2} = Z-factor of pure nitrogen gas; P = system pressure (bar); a_0, a_1, and a_2 are parameters which are a function of temperature and are expressed as

$$a_0 = b_0 + b_1 T + b_2 T^2 \quad \text{(III.7b)}$$

$$a_1 = c_0 + c_1 T + c_2 T^2 \quad \text{(III.7c)}$$

$$a_2 = d_0 + d_1 T + d_2 T^2 \quad \text{(III.7d)}$$

where, T = temperature (°C); and regression constants $b_0, b_1, b_2, c_0, c_1, c_2, d_0, d_1$, and d_2 are provided in Table III-1.

Table III-1: Regression parameters for calculating the Z factor for Nitrogen gas

Parameter	Value	Parameter	Value	Parameter	Value
b_0	9.902E-1	c_0	-2.078E-4	d_0	2.273E-6
b_1	7.827E-5	c_1	7.45E-6	d_1	-2.051E-8
b_2	-1.791E-7	c_2	-2.534E-8	d_2	6.79E-11

III.2 Material Balance

Mass balance for each phase can be written under the following assumptions:

- Mass transfer between phases is negligible.
- No fluid influx from the formation

- The cuttings volume fraction is very small
- Flow is isothermal in the small control volume
- Liquid phase is incompressible

Mass balance for Gas Phase

Applying the equation of state:

$$Q_{i+1} = \frac{Z_{i+1} Q_i P_i T_{i+1} \Gamma_i}{Z_i P_{i+1} T_i \Gamma_{i+1}} \tag{III.8}$$

where, Q_i = foam volume flow rate in element i.

Mass balance for Liquid Phase

For incompressible liquid phase:

$$Q_{i+1}(1 - \Gamma_{i+1}) = Q_i(1 - \Gamma_i) \tag{III.9}$$

Combining Equations III.8 and III.9, equation of quality as a function of pressure can be obtained in isothermal flow:

$$\Gamma_{i+1} = \frac{1}{(1 + \beta P_{i+1}/(Z_{i+1} \times T_{i+1}))} \tag{III.10}$$

where $\beta = \frac{Z_{bp} T_{bp}}{P_{bp}} \left(\frac{1}{\Gamma_{bp}} - 1 \right)$, and "bp" symbolizes the parameter values at the backpressure valve at the top of the annulus.

Foam Density

Using the equation of state for gas density and calculating the cuttings concentration in the next section, foam density can be calculated using the following equation:

$$\rho_{i+1} = \Gamma_{i+1} \frac{p_{i+1} M}{Z_{i+1} RT} + (1 - \Gamma_{i+1}) \rho_L + \mathrm{C_s}_{i+1} \rho_s \tag{III.11}$$

Note that for flow inside drill string the cuttings concentration, C_s, is "0" throughout.

Average Foam Velocity

$$u_{i+1} = \frac{Q_{i+1}}{A} \tag{III.12}$$

where, A = cross-sectional area.

III.3 Mechanical Energy Balance

The general form of mechanical energy balance for the control volume can be written in differential form as,

$$dU + d\left(\frac{P}{\rho}\right) + \frac{udu}{g_c} + \frac{g}{g_c}dZ + dq + dW_s = 0 \tag{III.13}$$

where dU = change in internal energy of the system; $d\left(\frac{P}{\rho}\right)$ = change in energy due to expansion or compression; $\frac{udu}{g_c}$ = change in kinetic energy; $\frac{g}{g_c}dZ$ = change in potential energy; dq = heat energy added to the system; dW_s = work done on the fluid by the surroundings, g_c= 1 (kg-m/N-s^2).

is difficult to apply due to the internal energy term, therefore, using thermodynamic relations, the change in internal energy of the system is written as,

$$dU = dh - d\left(\frac{P}{\rho}\right) \tag{III.14}$$

where, dh = change in enthalpy and is expressed in terms of change in entropy, dS,

$$dh = TdS + \left(\frac{dP}{\rho}\right) \tag{III.15}$$

or,

$$dU = TdS + \frac{dp}{\rho} - d\left(\frac{P}{\rho}\right) \quad \text{(III.16)}$$

Substituting and simplifying Eq. I.13,

$$TdS + \frac{dp}{\rho} + \frac{udu}{g_c} + \frac{g}{g_c}dZ + dq + dW_s = 0 \quad \text{(III.17)}$$

Pipe flow is an irreversible process, and Clausis inequality states that in such cases, the following inequality holds true,

$$dS \geq -\frac{dq}{T} \quad \text{(III.18)}$$

or,

$$TdS = -dq + dLw \quad \text{(III.19)}$$

where, dL_w = losses introduced due to irreversibility like friction.

If no external work was performed on the fluid contained in the control volume, general mechanical balance equation reduces to,

$$\frac{dp}{\rho} + \frac{udu}{g_c} + \frac{g}{g_c}dZ + dL_w = 0 \quad \text{(III.20)}$$

In case of an inclined pipe section,

$$\frac{dp}{\rho} + \frac{udu}{g_c} + \frac{g}{g_c}dl\cos\theta + dL_w = 0 \quad \text{(III.21)}$$

where $dZ = dL\ \cos\theta$. Multiplying both sides of the equation by, $\frac{\rho}{dL}$,

$$\frac{dp}{dL} + \frac{\rho udu}{g_c dL} + \frac{g}{g_c}\rho\cos\theta + \rho\left(\frac{dL_w}{dL}\right) = 0 \quad \text{(III.22)}$$

If pressure loss is assumed to be positive in the direction of flow, then Eq. I.34 can be evaluated for pressure loss along the length of the pipe section.

$$\frac{dp}{dL} = -\left[\frac{g}{g_c}\rho\cos\theta + \frac{\rho u du}{g_c dL} + \rho\left(\frac{dL_w}{dL}\right)\right] \tag{III.23}$$

The term, $\rho\left(\frac{dL_w}{dL}\right) = \left(\frac{dp}{dL}\right)_f$ = pressure gradient due to viscous shear or friction losses.

Most of the viscous shearing occurs at the wall, and therefore a ratio of wall shear stress, τ_w, to the kinetic energy per unit volume, $(\rho u^2/2g_c)$ provides the relative importance of wall shear stress towards contribution to total losses.

$$f = \frac{2\tau_w g_c}{\rho u^2} \tag{III.24}$$

where f = dimensionless Fanning friction factor. Also, wall shear stress is expressed as $\tau_w = \frac{d}{4}\left(\frac{dP}{dL}\right)_f$.

The expression for friction pressure loss,

$$\left(\frac{dP}{dL}\right)_f = \frac{2\,f\rho u^2}{g_c d} \tag{III.25}$$

Substituting and simplifying,

$$\frac{dp}{dL} = -\left[\frac{g}{g_c}\rho\cos\theta + \frac{\rho u du}{g_c dL} + \frac{2\,f\rho u^2}{g_c d}\right] \tag{III.26}$$

The generic form of mechanical energy balance, therefore,

$$\frac{dp}{dL} = \left(\frac{dp}{dL}\right)_{el} + \left(\frac{dp}{dL}\right)_f + \left(\frac{dp}{dL}\right)_{acc} \tag{III.27}$$

where,

$\left(\frac{dP}{dL}\right)_{el} = \frac{g}{g_c}\rho cos\theta$ = hydrostatic gradient due to elevation change.

$\left(\frac{dP}{dL}\right)_{f} = \frac{2f\rho u^2}{g_c d}$ = friction loss gradient, always acting opposite to the direction of flow.

$\left(\frac{dP}{dL}\right)_{acc} = \frac{\rho u du}{g_c\, dL}$ = kinetic energy or convection acceleration gradient.

Appendix IV

Calculation Procedure for Foam Drilling Hydraulics Model

The stepwise calculation procedure involved in the hydraulic modeling of the foam drilling process (Figure 6.2) is listed in the following sections.

Foam Hydraulics in the Annulus

1. The calculation begins at the top of the annulus (point "1") at the back pressure valve, where the flow parameters, β_{bp}, Z_{bp}, $Q_{G_{bp}}$, $Q_{F_{bp}}$, $u_{F_{bp}}$, Γ_{bp}, $\rho_{G_{bp}}$, $\rho_{F_{bp}}$, $n_{F_{bp}}$, $K_{F_{bp}}$ were calculated using Eqs. III.8 to III.12 (Appendix III).

$$\beta_{bp} = \frac{Z_{bp}T_{bp}}{P_{bp}}\left(\frac{1}{\Gamma_{bp}} - 1\right) \tag{IV.1}$$

where, β_{bp} remains constant for the entire wellbore.

$$Q_{G_{bp}} = \left(Z_{bp}T_{bp}P_{sc}\ Q_{G_{sc}}\right)/\left(Z_{sc}T_{sc}P_{bp}\right) \tag{IV.2}$$

where subscript "sc" is parameters measured at standard conditions.

$$Q_{F_{bp}} = Q_{G_{bp}} + Q_L \tag{IV.3}$$

where, $Q_L =$ liquid injection rate.

$$u_{F_{bp}} = Q_{F_{bp}}/A_{annulus} \tag{IV.4}$$

where, $A_{annulus} = \pi(D_{OH}^2 - D_{DP}^2)/4$ = Annular area.

2. The temperature at the bottom of the grid was calculated

$$T_2 = T_1 + \left(\frac{d\Delta T}{dL}\right)_{Geothermal}\Delta L \tag{IV.5}$$

3. The flow parameters (Z_2, Q_{G_2}, Q_{F_2}, u_{F_2}, Γ_2, ρ_{G_2}, ρ_{F_2} , n_{F_2}, K_{F_2}) at point "2" in the annulus are initialized using pressure at top of the grid, P_1, and temperature at the bottom of the grid, T_2.
4. The average values of all parameters for the grid, which are then substituted are calculated for the entire grid.

$$Re \approx \frac{\left(\rho_{F_2} + \rho_{F_1}\right)\left[0.5\left(u_{F_2} + u_{F_2}\right)\right]^{2-\left[0.5\left(n_{F_2}+n_{F_1}\right)\right]} D_h{}^{\left[0.5\left(n_{F_2}+n_{F_1}\right)\right]}}{\left(K_{F_2} + K_{F_1}\right)8^{\left[0.5\left(n_{F_2}+n_{F_1}\right)\right]-1}} \tag{IV.6}$$

5. The fluid Fanning friction factors are calculated using the calculated Reynolds number and applying Eqs. (6.8) to (6.10) for laminar and turbulent flow.
6. The cuttings concentration is calculated for the control volume.

$$C_s = \frac{(1-\phi)\times {D_{OH}}^2 \times ROP}{4\left[0.5\left(Q_{F_2}+Q_{F_1}\right)\right]} \tag{IV.7}$$

7. The cuttings friction factor was calculated by applying Eq. (6.11). The net friction factor in the annulus section is the summation of the fluid and solids friction factors.
8. The frictional pressure loss, hydrostatic and the pressure drop due to fluid acceleration are calculated and the net pressure drop at the bottom of the grid "P_{bot}" was calculated using Eq. (6.15).
9. Using the newly calculated value of pressure and temperature, at the bottom of the section, i.e., at point "2", the flow parameters ($Z_{2_{new}}$, $Q_{G_{2_{new}}}$, $Q_{F_{2_{new}}}$, $u_{F_{2_{new}}}$, $\Gamma_{2_{new}}$, $\rho_{G_{2_{new}}}$, $\rho_{F_{2_{new}}}$, $n_{F_{2_{new}}}$, $K_{F_{2_{new}}}$) are recalculated using the procedure listed in step 1.
10. With the new initial values at point "2", steps 4 to 8 are repeated and the new value of pressure at the bottom of the section, "$P_{bot_{new}}$" was calculated.

11. The difference between the pressure at the two iterations ($\Delta P = P_{bot_{new}} - P_{bot}$) was calculated.
12. If the value of "ΔP" does not meet the desired accuracy, steps 9 to 11 were repeated using the new values of pressure "$P_{bot_{new}}$" at the end of the segment.
13. The entire procedure was repeated until the calculations reached the bottom of the wellbore.

Pressure drop across the drill bit

14. The terms A, E, and B are calculated at bottom hole conditions using Eqs. (6.16) to (6.18),

$$A = \frac{\dot{m}_{G_{BH}}}{\left(\dot{m}_{G_{BH}} + \dot{m}_{L_{BH}}\right)} \cdot \frac{Z_{BH} R T_{BH}}{M} \tag{IV.8}$$

$$E = \frac{1}{2.A.g_c} \tag{IV.9}$$

$$B = \frac{\dot{m}_{G_{BH}}}{\rho_L\left(\dot{m}_{G_{BH}} + \dot{m}_{L_{BH}}\right)} \tag{IV.10}$$

15. The average foam velocity across the nozzles is calculated using an equivalent diameter concept as described in Eqs. (6.19) and (6.20).

$$u_n = \frac{Q_{F_{BH}}}{\left(\pi {D_{n_{eq}}}^2/4\right)} \tag{IV.11}$$

16. Assuming an initial value for the pressure drop across the drill bit, the pressure upstream of the drill bit inside the drill string was calculated iteratively by applying Eq. (6.15).

$$P_{BH} = P_{US} \cdot exp\left(\frac{B\Delta P_{bit}}{A} - E \cdot u_n^2\right) \tag{IV.12}$$

Pressure drop inside the drill string

17. After estimating the pressure just above the drill bit, the calculations move inside the drill string until it reaches the surface.

18. Using the pressure and the temperature at the bottom hole condition, values of the flow parameters (Z_{BH}, $Q_{G_{BH}}$, $Q_{F_{BH}}$, $u_{F_{BH}}$, Γ_{BH}, $\rho_{G_{BH}}$, $\rho_{F_{BH}}$, $n_{F_{BH}}$, $K_{F_{BH}}$) at point "P_{1P}" were calculated using Eqs. III.8 to III.12 (Appendix III).

$$Q_{G_{BH}} = \left(Z_{BH}T_{BH}P_{sc}\, Q_{G_{sc}}\right)/(Z_{sc}T_{sc}P_{BH}) \tag{IV.13}$$

where subscript "sc" is parameters measured at standard conditions.

$$Q_{F_{BH}} = Q_{G_{BH}} + Q_L \tag{IV.14}$$

where, Q_L = liquid injection rate.

$$u_{F_{bp}} = Q_{F_{bp}}/A_{Drillstring} \tag{IV.15}$$

where, $A_{Drillstring} = \pi(D_{DP}^2)/4$ = Cross-sectional flow area of the drill pipe.

20. The temperature at point "P_{2P}" is calculated using the geothermal gradient,

$$T_{2P} = T_{1P} - \left(\frac{d\Delta T}{dL}\right)_{Geothermal} \Delta L \tag{IV.16}$$

where ΔL = length of the segment of the drill string.

21. Using the pressure at the bottom of the section inside the drill string, i.e., "P_{1P}" as the initial input and temperature at the top of the section i.e., "T_{2P}", the flow parameters (Z_{2P}, $Q_{G_{2P}}$, $Q_{F_{2P}}$, $u_{F_{2P}}$, Γ_{2P}, $\rho_{G_{2P}}$, $\rho_{F_{2P}}$, $n_{F_{2P}}$, $K_{F_{2P}}$) at the point "2P" is calculated.

22. The arithmetic mean of the parameters are calculated for the drill pipe segment, and the averaged generalized Reynolds is calculated using the following equation,

$$Re \approx \frac{\left(\rho_{F_{2P}} + \rho_{F_{1P}}\right)\left[0.5\left(u_{F_{2P}} + u_{F_{2P}}\right)\right]^{2-\left[0.5\left(n_{F_{2P}}+n_{F_{1P}}\right)\right]} D_h^{\left[0.5\left(n_{F_{2P}}+n_{F_{1P}}\right)\right]}}{\left(K_{F_{2P}} + K_{F_{1P}}\right)8^{\left[0.5\left(n_{F_{2P}}+n_{F_{1P}}\right)\right]-1}} \tag{IV.17}$$

23. Using the Reynolds number values the fluid Fanning friction factors are calculated by applying Eqs. (6.8) to (6.10) for laminar and turbulent flow.
24. The frictional pressure loss, hydrostatic head loss and the pressure drop due to fluid acceleration components along the segment lengths are calculated and the net pressure drop at the top of the grid "P_{top}" was calculated using Eq. (6.13).
25. Using the new value of pressure and temperature, at top of the grid, i.e., at point "2P", the flow parameters ($Z_{2P_{new}}$, $Q_{G_{2P_{new}}}$, $Q_{F_{2P_{new}}}$, $u_{F_{2P_{new}}}$, $\Gamma_{2P_{new}}$, $\rho_{G_{2P_{new}}}$, $\rho_{F_{2P_{new}}}$, $n_{F_{2P_{new}}}$, $K_{F_{2P_{new}}}$) are recalculated using the procedure listed in step 18.
26. With the new initial values at point "2P", step 24 is repeated and the new value of pressure at the bottom of the section, "$P_{top_{new}}$" was calculated.
27. The difference between the pressure at the two iterations ($\Delta P = P_{top_{new}} - P_{top}$) was calculated.
28. If the value of "ΔP" does not meet the desired accuracy, steps 25 to 27 were repeated using the new values of pressure "$P_{top_{new}}$" at the top of the segment.
29. The entire procedure was repeated until the calculations reached the top of the drill pipe.

Appendix V

Base Case Hydraulic Model Results

V.1 Vertical Wellbore

Table V-1: Simulation results in a vertical wellbore using base case inputs

Depth	Annulus				Drill Pipe			
	Pressure (MPa)	Quality (Γ)	Density (kg/m^3)	u (m/s)	Pressure (MPa)	Quality (Γ)	Density (kg/m^3)	u (m/s)
0	0.7	0.96	48.44	4	5.9	0.76	285.65	1.74
200	1.85	0.91	121.23	1.59	6.45	0.75	305.48	1.63
400	3	0.86	186.36	1.03	7.04	0.73	325.91	1.53
600	4.16	0.81	244.31	0.79	7.68	0.71	346.71	1.44
800	5.29	0.78	295.58	0.65	8.35	0.7	367.66	1.36
1000	6.42	0.74	341.51	0.56	9.05	0.68	388.66	1.29
1200	7.53	0.71	382.85	0.5	9.8	0.66	409.63	1.23
1400	8.62	0.68	419.7	0.46	10.58	0.64	430.49	1.17
1600	9.71	0.66	453.22	0.42	11.4	0.63	451.19	1.12
1800	10.8	0.63	484.21	0.4	12.26	0.61	471.65	1.07
2000	11.91	0.61	513.19	0.38	13.16	0.59	491.81	1.03
2200	13.05	0.59	539.95	0.36	14.09	0.58	511.62	0.99
2400	14.22	0.57	565.72	0.35	15.07	0.56	531	0.96
2600	15.42	0.55	590.08	0.33	16.08	0.54	549.92	0.93
2800	16.66	0.53	613.1	0.32	17.13	0.53	568.32	0.9
3000	17.93	0.52	634.84	0.31	18.21	0.51	586.16	0.87
3048	18.24	0.51	639.87	0.31	18.48	0.51	590.36	0.87

V.2 Three-Segment Wellbore

Table V-2: Simulation results in a three-segment wellbore using base case inputs

Depth	Annulus				Drill Pipe			
	Pressure (MPa)	Quality (Γ)	Density (kg/m^3)	u (m/s)	Pressure (MPa)	Quality (Γ)	Density (kg/m^3)	u (m/s)
0	0.7	0.96	48.44	4	7.41	0.72	342.68	1.48
200	1.82	0.91	118.35	1.63	7.97	0.7	357.68	1.42
400	2.9	0.87	176.77	1.09	8.55	0.69	372.32	1.36
600	3.94	0.83	226.45	0.85	9.14	0.68	386.53	1.32
800	4.95	0.79	269.48	0.71	9.75	0.67	400.33	1.27
1000	5.87	0.77	304.93	0.63	10.27	0.66	411.52	1.24
1200	6.69	0.75	333.85	0.58	10.67	0.65	419.45	1.22
1400	7.52	0.73	360.97	0.53	11.07	0.64	427.21	1.2
1600	8.33	0.71	385.22	0.5	11.47	0.64	434.8	1.18
1800	9.12	0.69	407.19	0.47	11.89	0.63	442.23	1.16
2000	9.42	0.68	415.46	0.46	11.77	0.63	439.31	1.17
2200	9.62	0.68	420.94	0.46	11.58	0.64	434.64	1.18
2400	9.82	0.68	426.58	0.46	11.38	0.64	429.97	1.19
2600	10.01	0.67	431.87	0.45	11.18	0.65	425.29	1.2
2800	10.19	0.67	436.87	0.45	10.99	0.65	420.61	1.22
3000	10.36	0.66	441.6	0.44	10.8	0.65	415.95	1.23
3048	10.4	0.66	442.69	0.44	10.76	0.66	414.83	1.23